SHORT-DISTANCE MATRIX ELEMENTS FOR D-MESON MIXING FOR 2+1 FLAVOR LATTICE QCD

BY

CHIA CHENG CHANG

DISSERTATION

Submitted in partial fulfillment of the requirements
for the degree of Doctor of Philosophy in Physics
in the Graduate College of the
University of Illinois at Urbana-Champaign, 2015

Urbana, Illinois

Doctoral Committee:

Professor Michael Stone, Chair
Professor Aida X. El-Khadra, Director of Research
Dr. Andreas Kronfeld
Professor Kevin Pitts
Professor Ryu Shinsei

Abstract

We study the short-distance hadronic matrix elements for D-meson mixing with partially quenched $N_f = 2{+}1$ lattice QCD. We use a large set of the MIMD Lattice Computation Collaboration's gauge configurations with a^2 tadpole-improved staggered sea quarks and tadpole-improved Lüscher-Weisz gluons. We use the a^2 tadpole-improved action for valence light quarks and the Sheikoleslami-Wohlert action with the Fermilab interpretation for the valence charm quark. Our calculation covers the complete set of five operators needed to constrain new physics models for D-meson mixing. We match our matrix elements to the $\overline{\text{MS}}$-NDR scheme evaluated at 3GeV. We report values for the Beneke-Buchalla-Greub-Lenz-Nierste choice of evanescent operators and obtain

$$\begin{aligned}
\langle \mathcal{O}_1 \rangle / m_D =& 0.042(4)\text{GeV}^3, \\
\langle \mathcal{O}_2 \rangle / m_D =& -0.078(4)\text{GeV}^3, \\
\langle \mathcal{O}_3 \rangle / m_D =& 0.033(2)\text{GeV}^3, \\
\langle \mathcal{O}_4 \rangle / m_D =& 0.155(10)\text{GeV}^3, \\
\langle \mathcal{O}_5 \rangle / m_D =& 0.058(6)\text{GeV}^3.
\end{aligned}$$

To Xiaoqian, Mom and Dad. Thanks for everything.

Acknowledgments

Thank you Aida and Andreas for mentoring me throughout the years both as a physicist and as a young man finding his way in life. Thank you Chris, Daniel, Daping, Elizabeth, Elvira and Paco for the discussions which helped me understand what I know today and for all the wonderful moments I had during graduate school. Thank you Jim for your support and for the discussion regarding coding and data structure, as well as all the wonderful coffee break stories!

This work was supported in part by the University Research Association Visiting Scholars' program, the Fermilab Fellowship of Theoretical Physics, and the DOE grant under grant number DOE DE-FG02-13ER42001

Computations for this work were carried out with resources provided by the USQCD Collaboration, the Argonne Leadership Computing Facility, the National Energy Research Scientific Computing Center, and the Los Alamos National Laboratory, which are funded by the Office of Science of the United States Department of Energy; and with resources provided by the National Institute for Computational Science, the Pittsburgh Supercomputer Center, the San Diego Supercomputer Center, and the Texas Advanced Computing Center, which are funded through the National Science Foundation's Teragrid/XSEDE Program.

Fermilab is operated by Fermi Research Alliance, LLC, under Contract No. DE- AC02-07CH11359 with the U.S. Department of Energy.

Table of Contents

List of Tables

List of Figures

Chapter 1

The Standard Model

1.1 Symmetries of the Standard Model

The Standard Model of particle physics describes the electroweak and strong forces and their interactions with the matter particles of the universe. The gauge fields are force carriers, and their interaction with matter is described by the theory of Quantum Chromodynamics and Electroweak. Geometrically, gauge fields are introduced as connections which preserve invariance of the Lagrangian under local phase transformations. For the strong interaction, the gauge fields G_μ^a transform under the adjoint representation of $\mathrm{SU}(3)_c$, while in the electroweak theory, the gauge fields W_μ^a and B_μ transform under the adjoint representation of $\mathrm{SU}(2)_L \otimes \mathrm{U}(1)_Y$. The index a runs of over the generators of the Lie algebra, while the index on the groups remind us that the gauge fields are symmetric under change in color, weak-isospin of left-handed matter fields, and hypercharge. The geometric interpretation of gauge fields as connections necessitates that they transform under the adjoint representation. On the other hand, matter fields transform under the fundamental representation as confirmed by the existence of anti-particles transforming under the complex conjugate representation such that the generators $\tau_a \neq -\tau_a^*$. Finally, the Higgs transforms under the fundamental representation of SU(2), which can be verified by the experimental result $m_Z = m_W/\cos\theta_w$. If the Higgs transforms under the adjoint representation, the predicted relationship between the mass of the Z-boson and W-bosons would instead be $m_Z = \sqrt{2} m_W/\cos\theta_w$. Another feature of the Standard Model is that the weak interaction is maximally parity violating, which was first observed in the decays of ^{60}Co, which later led to a Nobel Prize in physics for Lee and Yang. Therefore, right-handed quark fields are decoupled from the weak Lagrangian by demanding that they transform under the trivial representation of SU(2), while still carrying hypercharge. In 2012, direct searches for the Higgs at ATLAS and CMS led to the discovery of a Higgs-like scalar, verifying the existence of the last of the Standard Model particles [1, 25]. The charges of the Standard Model fields are listed in table 1.1 as tabulated in Ref. [57].

The Standard Model Lagrangian is gauge invariant after promoting deriva-

Field	$L = \begin{pmatrix} \nu_L \\ e_L \end{pmatrix}$	e_R	ν_R	$Q = \begin{pmatrix} u_L \\ d_L \end{pmatrix}$	u_R	d_R	H
SU(3)$_c$	0	0	0	□	□	□	0
SU(2)$_L$	□	0	0	□	0	0	□
U(1)$_Y$	$-\frac{1}{2}$	-1	0	$\frac{1}{6}$	$\frac{2}{3}$	$-\frac{1}{3}$	$\frac{1}{2}$

Table 1.1: Standard Model fields and their transformation properties with respect to gauge fields. □ denotes the fundamental representation, 0 denotes the trivial representation, while the explicit hypercharges are given. The generators of trivial representations are 0 satisfying the Lie algebra $[0, 0] = 0$, explicitly decoupling the gauge field from the matter fields. Representations of the hypercharge are elements of real numbers. Conventionally defining the charge of the electron as -1 results in the list of hypercharges listed in the table. L and Q are written explicitly as doublets of SU(2), although the quark fields transform as triplets under SU(3). All leptons and quark fields also come with a suppressed index which labels the three generations of particles. Under Lorentz transformation, left-handed particles transform under the $(\frac{1}{2}, 0)$ and right-handed particles transform under the $(0, \frac{1}{2})$ spinor representation of the Lorentz group. Finally, right-handed neutrinos have not been observed and therefore do not interact with the Standard Model gauge fields but are included for completeness.

tives to covariant derivatives

$$\partial_\mu \to D_\mu = \partial_\mu - igA^a_\mu \tau_a \tag{1.1}$$

where g is the coupling strength, A^a_μ is a gauge field with the group index a and Lorentz index μ while τ_a is the generator of the group in the fundamental representation. It can be shown that under such a substitution, the kinetic term of the Lagrangian is gauge invariant,

$$\mathcal{L}_{\text{kin.}} = \sum_{j=\{1,2,3\}} \sum_{i=\{L,R\}} i\bar{\psi}^j_i (\not{\partial} - ig_s \not{G}^a \Lambda_a - ig \not{W}^a \tau_a - ig' \not{B} Y) \psi^j_r, \tag{1.2}$$

where we sum over j-generations for i-handed states and Λ_a, τ_a, and Y are generators of SU(3), SU(2) and U(1) respectively. To complete the minimal theory, we include the Lagrangian for dynamical gauge bosons,

$$\mathcal{L}_{\text{gauge}} = -\frac{1}{4} G_{\mu\nu} G^{\mu\nu} - \frac{1}{4} W_{\mu\nu} W^{\mu\nu} - \frac{1}{4} B_{\mu\nu} B^{\mu\nu} \tag{1.3}$$

where $W_{\mu\nu}$ and $B_{\mu\nu}$ are the stress-energy tensors. Mass terms for gauge fields of the form $mB_\mu B^\mu$ are prohibited by gauge invariance, therefore gauge fields are massless. While this is observed to be true for the gluons, there is more to this picture in the electroweak sector. Experimentally, the weak gauge fields are measured to have mass of 80 to 91 GeV, which can be understood through the Higgs mechanism.

1.2 The Higgs mechanism

The Higgs mechanism is most easily revealed by studying the abelian Higgs model, which is the linear sigma model gauged with a one-component U(1) field. A review of this model is given in Ref. [57] with the main concepts summarized here. In this toy model, the Lagrangian is

$$\mathcal{L} = -\frac{1}{4}F_{\mu\nu}^2 + |\partial_\mu\phi + ieA_\mu\phi|^2 + m^2\phi^2 - \frac{\lambda}{4}|\phi|^4. \tag{1.4}$$

The Lagrangian is invariant under global U(1) rotations, $F_{\mu\nu}$ is the field strength of the U(1) gauge field and ϕ is a complex scalar fields. The factor of 1/4 is a convention such that the Feynman rule for the $|\phi|^4$ interaction turns out to be $i\lambda$. The minimum of the scalar potential lies at the bottom of the "Mexican hat" potential with radius $\phi_0 = \sqrt{2m^2/\lambda} \equiv v/\sqrt{2}$. Without loss of generality, we choose our vacuum along the positive real axis, which is equivalent to choosing the unitarity gauge, and parametrize fluctuations around the vacuum in the amplitude and phase,

$$\phi(x) = \left(\frac{v + \sigma(x)}{\sqrt{2}}\right) e^{i\frac{\pi(x)}{\sqrt{2}v}}. \tag{1.5}$$

Expanding the abelian Higgs Lagrangian around this minima spontaneously breaks global U(1). In other words, the symmetry of the Lagrangian is not respected by the ground state that is chosen (or any that can be chosen for that matter). We see that the quadratic terms of the gauge field are,

$$\mathcal{L}_{\text{gauge}} = -\frac{1}{4}F_{\mu\nu}^2 + \frac{1}{2}e^2v^2A_\mu^2. \tag{1.6}$$

As a result the gauge field gains a mass term of $m_A = ev$, which arises due to the specific choice of gauge. More generally, the gauge field now has three non-zero polarizations.

The same reasoning is applied to the electroweak sector, where the scalar field now transforms as a doublet under SU(2). Without loss of generality, we can choose the ground state of the Higgs potential $m^2\phi^\dagger\phi - \lambda(\phi^\dagger\phi)^2$ to be at

$$\phi_0 = \frac{1}{\sqrt{2}}\begin{pmatrix} 0 \\ v \end{pmatrix}. \tag{1.7}$$

To determine the masses of the gauge fields, we can simply substitute the ground state without perturbations in to the kinetic term of the scalar field

$$\left|\left(i\partial_\mu - gW_\mu^a\tau_a - \frac{1}{2}ig'B_\mu\right)\phi\right|^2, \tag{1.8}$$

and rotating to the mass basis,

$$Z_\mu \equiv \cos\theta_w W_\mu^3 - \sin\theta_w B_\mu \tag{1.9}$$

$$A_\mu \equiv \sin\theta_w W_\mu^3 + \cos\theta_w B_\mu \tag{1.10}$$

$$W_\mu^\pm = \frac{1}{\sqrt{2}}\left(W_\mu^1 \mp i W_\mu^2\right) \tag{1.11}$$

where $\tan\theta_W = g'/g$, we see that the Lagrangian becomes,

$$\frac{1}{4} g v^2 W_\mu^+ W_\mu^- + \frac{1}{8} v^2 (g^2 + g'^2) Z_\mu Z^\mu + \text{interaction terms.} \tag{1.12}$$

As a result, the weak gauge bosons $W^\pm$ and Z gain mass through the Higgs mechanism, while leaving the photon A_μ massless as protected by $\mathrm{U}(1)_{em}$.

Masses of fermions are introduced into the Standard Model though the Higgs mechanism in the Yukawa sector,

$$\mathcal{L}_{\text{Yukawa}} = -Y_{ij}^d \bar{Q}^i \phi d_R^j - Y_{ij}^u \bar{Q}^i \tilde{\phi} u_R^j + \text{h.c.} \tag{1.13}$$

where the term proportional to Y^d and Y^u gives mass respectively to down-type and up-type quarks. The indices i, j run through the three generation of quarks. The field $\tilde{\phi} \equiv i\sigma_2 \phi^*$ is necessary to generate a $\bar{u}_L u_R$ term after SSB in unitarity gauge, while the transformation using the Pauli matrix σ_2 preserves invariance under SU(2). Substituting the ground states

$$\phi_0 = \frac{1}{\sqrt{2}}\begin{pmatrix} 0 \\ v \end{pmatrix} \qquad\qquad \tilde{\phi}_0 = \frac{1}{\sqrt{2}}\begin{pmatrix} v \\ 0 \end{pmatrix} \tag{1.14}$$

into the Yukawa sector, we get after SSB

$$\mathcal{L}_{\text{Yukawa}} = -\frac{v}{\sqrt{2}} Y_{ij}^d \bar{d}_L^i d_R^j - \frac{v}{\sqrt{2}} Y_{ij}^u \bar{u}_L^i u_R^j + \text{h.c.}. \tag{1.15}$$

This Lagrangian can be rotated from the flavor basis to the mass basis by introducing unitary transformations which diagonalizes the Yukawa couplings, uncovering masses for quarks. We can similarly generate masses for the charged leptons in exactly the same fashion.

As a result of moving to the mass basis, the kinetic terms of the electroweak Lagrangian is also affected and results in mixing between up-type and down-type quarks. For neutral currents, down-type quarks are rotated to the mass basis via a unitary transformation U_d results in the following transformation $Z_\mu \bar{d}_L U_d^\dagger \gamma^\mu U_d d_L \rightarrow Z_\mu \bar{d}_L \gamma^\mu d_L$ where $U_d^\dagger U_d = 1$. The same logic applies to up-type quarks which in general rotates under a different unitary transformation U_u. This is the famous result stating the absence of tree-level flavor-changing-neutral-currents in the Standard Model. For charged currents however, the quark-$W^\pm$ vertex looks like $W_\mu^+ \bar{u}_L^i \gamma^\mu V_{ij} d_L^j$, where $V_{ij} = U_u^\dagger U_d$ is not diagonal if $U_u \neq U_d$. The matrix V is called the Cabbibo-Kobayashi-Maskawa (CKM) matrix which parametrizes mixing between up-type and down-type quarks.

Chapter 2

D-meson Mixing Phenomenology

In nature, the D^0- and $\bar{D}^0$-mesons are observed in their mass eigenstate. Under the weak interaction, mixing has been observed and may be described by an effective Hamiltonian in the time dependent Schrödinger equation

$$i\frac{\partial}{\partial t}\begin{pmatrix} D^0(t) \\ \bar{D}^0(t) \end{pmatrix} = \left(\mathbf{M} - \frac{i}{2}\mathbf{\Gamma}\right)\begin{pmatrix} D^0(t) \\ \bar{D}^0(t) \end{pmatrix}. \tag{2.1}$$

Specifically, the Hamiltonian is not Hermitian due to the dispersive term leaking probability onto on-shell intermediate states. However, $\mathbf{M}$ and $\mathbf{\Gamma}$ individually are Hermitian since in general, the mixing Hamiltonian can be written as

$$H = \frac{1}{2}\left(H + H^\dagger\right) - \frac{i}{2}\left[i\left(H - H^\dagger\right)\right]. \tag{2.2}$$

The diagonal elements of the Hamiltonian are expected to be equal because the mass of the particle is the same as the mass of the anti-particle. The Hamiltonian explicitly may be written as,

$$\mathbf{M} - \frac{i}{2}\mathbf{\Gamma} = \begin{pmatrix} M & M_{12} \\ M_{12}^* & M \end{pmatrix} - \frac{i}{2}\begin{pmatrix} \Gamma & \Gamma_{12} \\ \Gamma_{12}^* & \Gamma \end{pmatrix}. \tag{2.3}$$

It follows that the eigenvalues of the Hamiltonian are,

$$E_{\mathrm{H,L}} = M - \frac{i}{2}\Gamma \pm \frac{q}{p}\left(M_{12} - \frac{i}{2}\Gamma_{12}\right), \tag{2.4}$$

$$\left(\frac{q}{p}\right)^2 = \frac{M_{12}^* - \frac{i}{2}\Gamma_{12}^*}{M_{12} - \frac{i}{2}\Gamma_{12}}. \tag{2.5}$$

The normalization condition also places the condition that

$$|p|^2 + |q|^2 = 1. \tag{2.6}$$

The subscripts H and L suggest a heavier and lighter D-meson state in the mass diagonalized basis. The mass eigenstates $|D_{\mathrm{H,L}}\rangle$ are a superposition of the weak eigenstates:

$$|D_{\mathrm{H,L}}\rangle = p\left|D^0\right\rangle \pm q\left|\bar{D}^0\right\rangle, \tag{2.7}$$

Assuming that CP is a good symmetry, it follows that $p = q$, resulting in the mass eigenstate receiving equal contributions from the weak eigenstates. We may define the CP eigenstates as

$$|D_{\rm H,L}\rangle = |D_\pm\rangle \;\text{ if CP}\,|D_{\rm H,L}\rangle = \pm\,|D_{\rm H,L}\rangle\,. \tag{2.8}$$

Referring to the eigenvalues of Eq. (2.5), we assume no CP-violation and set $E_\pm = E_{\rm H,L}(p/q = 1)$ yielding the time evolution for the CP eigenstates given as

$$|D_\pm(t)\rangle = e^{-iE_\pm t}\,|D_\pm\rangle\,. \tag{2.9}$$

It follows from Eq. (2.7, 2.9) that the time evolution of the weak eigenstates are

$$\left|D^0(t)\right\rangle = \frac{e^{-iE_Ht} + e^{-iE_Lt}}{2}\left|D^0\right\rangle + \frac{q}{p}\frac{e^{-iE_Ht} - e^{-iE_Lt}}{2}\left|\bar{D}^0\right\rangle, \tag{2.10}$$

$$\left|\bar{D}^0(t)\right\rangle = \frac{e^{-iE_Ht} + e^{-iE_Lt}}{2}\left|\bar{D}^0\right\rangle + \frac{p}{q}\frac{e^{-iE_Ht} - e^{-iE_Lt}}{2}\left|D^0\right\rangle. \tag{2.11}$$

The probability of observing a $\left|\bar{D}^0\right\rangle$ at some time t when starting from the $\left|D^0\right\rangle$ state is,

$$\left|\left\langle\bar{D}^0|D^0(t)\right\rangle\right|^2 = \frac{1}{2}e^{-\Gamma t}\left[\cosh(\Gamma_{12}t) - \cos(2M_{12}t)\right]. \tag{2.12}$$

It is common to parametrize the argument of the hyperbolic cosine and cosine as the following,

$$x \equiv \frac{M_{12}}{\Gamma} = \frac{M_+ - M_-}{(\Gamma_+ + \Gamma_-)/2}, \qquad y \equiv \frac{\Gamma_{12}}{2\Gamma} = \frac{\Gamma_+ - \Gamma_-}{\Gamma_+ + \Gamma_-}. \tag{2.13}$$

In fact, experimental results are often reported with respect to x and y.

Theoretically the mixing arises from $|\Delta C = 1|$ and $|\Delta C = 2|$ operators which change the charm number by one and two respectively. Following Ref. [36], the off-diagonal elements of the Hamiltonian may be expressed as,

$$M_{12} = \left\langle\bar{D}^0\left|\mathcal{O}^{\Delta C=2}\right|D^0\right\rangle + P\sum_n \frac{\left\langle\bar{D}^0\left|\mathcal{O}^{\Delta C=1}\right|n\right\rangle\left\langle n\left|\mathcal{O}^{\Delta C=1}\right|D^0\right\rangle}{m_D^2 - E_n^2}, \tag{2.14}$$

$$\Gamma_{12} = \sum_n \rho_n\left\langle\bar{D}^0\left|\mathcal{O}^{\Delta C=1}\right|n\right\rangle\left\langle n\left|\mathcal{O}^{\Delta C=1}\right|D^0\right\rangle. \tag{2.15}$$

The sum is over all intermediate states. For M_{12}, these are off-shell states and correspondingly P denotes the principle value; while for Γ_{12} the intermediate states are on-shell so ρ_n is the density of the state n. The mixing parameters may therefore be expressed in terms of $\left\langle\mathcal{O}^{\Delta C=2}\right\rangle$ short-distance and $\left\langle\mathcal{O}^{\Delta C=1}\right\rangle$ long-distance matrix elements.

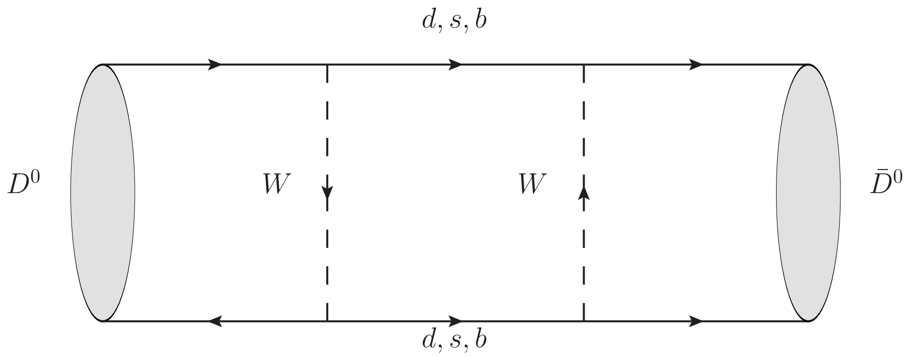

Figure 2.1: D-meson mixing box diagram. The W and intermediate d, s, b quarks are off-shell and have dynamics at the electroweak scale.

2.1 Short-distance contributions

D-meson mixing in the SM occurs initially at one-loop in electroweak theory in the absence of tree-level flavor changing neutral currents. The SM D-meson short-distance diagram shown in Fig. 2.1 is mediated by off-shell quarks and therefore have a typical interaction range of $1/M_W$, where M_W is the weak gauge boson mass. From the figure, we can immediately see that the amplitude is proportional to

$$A \propto \frac{m_i^2 m_j^2}{M_W^4} V_{ic} V_{iu}^* V_{jc} V_{ju}^*, \tag{2.16}$$

where $i, j = \{d, s, b\}$. We can conclude from Eq. (2.16) that the b-quark is $|V_{ub} V_{cb}^*|^2 \sim 0.2^1 0$ suppressed, allowing for D-meson mixing to be described by only two generations of quarks. Using this simplification, the SM short-distance D-meson mixing amplitude is given by [29]

$$\begin{aligned}\left\langle D^0 \left| H_{\mathrm{box}} \right| \bar{D}^0 \right\rangle =& \frac{G_f^2}{8\pi^2} V_{cs}^* V_{us} V_{cd}^* V_{ud} \frac{\left(m_s^2 - m_d^2\right)^2}{m_c^2} \\ & \times \left(\left\langle D^0 \left| \left(\bar{\psi}_u \Gamma \psi_c\right)^2 \right| \bar{D}^0 \right\rangle + 2 \left\langle D^0 \left| \left(\bar{\psi}_u \Gamma' \psi_c\right)^2 \right| \bar{D}^0 \right\rangle \right) \end{aligned} \tag{2.17}$$

where $\Gamma = (1 + \gamma_5)\gamma_\mu$ and $\Gamma' = 1 + \gamma_5$. From Eq. (2.17), GIM suppression can be seen explicitly by the $m_s^2 - m_d^2$ term. Therefore, in the Standard Model, the short-distance contribution to D-meson mixing is highly suppressed; in fact, order of magnitude estimates from quark models [39] suggest that the short-distance contributions to x and y are while experimental measurements find $x = (0.49^{+0.14}_{-0.15})\%$ and $y = (0.62 \pm 0.08)\%$ [3]. Long-distance contributions however, are not suppressed by the GIM mechanism as explained in detail in Section 2.2, and therefore may explain D-meson mixing. However, it is also possible that the short-distance contributions receive enhancement from new physics. Ref [38] provides a review of a subset of possible new physics contributions for D-meson mixing as well as rare D decays where the branching ratios predicted are completely fixed by the D-meson mixing matrix elements. Currently, the D-meson mixing matrix elements are estimated using the modified vacuum saturation approximation yielding order-of-magnitude estimates for various new physics contributions summarized in Table I of Ref. [38]. This dissertation provides the values of the matrix elements from the first principle description of QCD, allowing for well controlled systematics, providing model discrimination for various new physics models.

2.2 Long-distance contributions

While in the Standard Model D-meson mixing is expected to receive contribution mainly from the long-distance diagrams, with current lattice techniques, the long-distance diagrams are not able to be extracted. While significant progress on the long-distance Kaon-mixing diagrams have recently been made [5], D-meson mixing is an even harder problem due to the large mass of the D-meson. Unlike Kaon mixing where the long-distance diagram involves one intermediate pion, the mass of the D-meson results in contributions of two intermediate on-shell states. The D-meson is heavier than Λ_{QCD} and therefore introduces another length scale in the problem. For example, the process $D^0 \to K^+K^- \to \bar{D}^0$, is shown in Fig. 2.2. The interactions with the W-boson is described by perturbative electroweak and can be integrated out, resulting in a 4-point correlation function described by strong dynamics. The 4-point correlation function involved two intermediate states (in this case, $K^{\pm}$), which can be understood using the Lellouch-Lüscher formalism [43], where the finite volume matrix element can be related to the $D^0 \to K^+K^-$ decay amplitude. This study however, requires lattice ensembles that are currently unavailable.

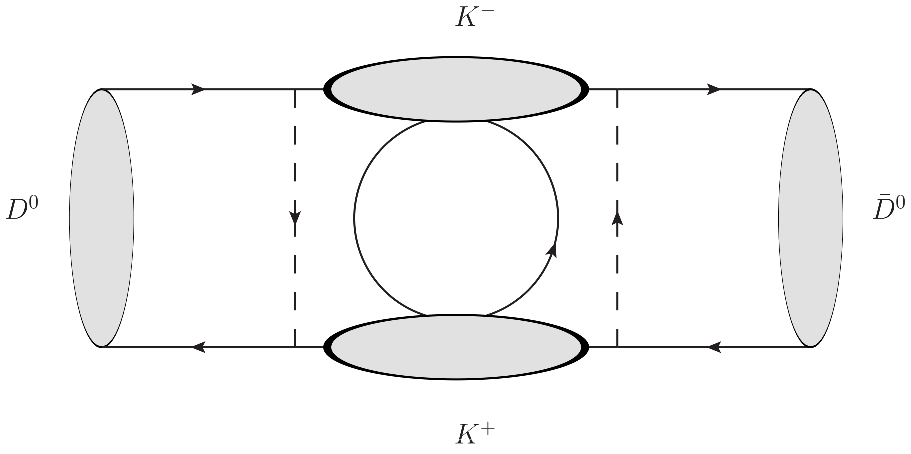

Figure 2.2: D-meson mixing long-distance diagram. The W bosons are off-shell and have dynamics at the electroweak scale while the $K^{\pm}$ are on-shell mesons with dynamics at the strongly-coupled QCD scale.

Currently, the long-distance contributions only have order-of-magnitude estimates. The estimates are provided through either exclusive or inclusive calculations of the long-distance diagrams [36]. The exclusive approach makes the assumption that the long-distance contribution is dominated by a small number of exclusive processes. This approach relies heavily on experimental data of the individual decay processes; due to the lack of precise experimental data, the exclusive approach introduces model dependent assumptions on the amplitudes and strong phase. The inclusive approach provides an estimate of the long-distance contribution via the operator product expansion. If one assumes that $m_c \gg \Lambda_{\text{QCD}}$, then it is ensured that the internal momentum is large and an expansion of short-distance diagrams may be performed to describe the long-distance contribution. In particular, the leading contribution of the long-distance diagram is described by the 4-quark operators of the short-distance diagram in this approach. However, higher-order corrections to the leading contribution involves a large number of diagrams, all involving non-perturbative matrix elements which need to be determined in order to control systematic errors. The charm quark mass of approximately 1GeV is also not significantly larger than Λ_{QCD}. While there is significant interest in understanding the long-distance contributions, this dissertation will focus on extracting the short-distance matrix elements, providing leverage for understanding the upper limits of BSM models.

2.3 The 4-quark operators

The 4-quark operators in Eq. (2.17) with heavy quarks Q and light quarks q form Lorentz invariant color singlets as shown in Eq. (2.18) and (2.19).

$$\bar{Q}_i^{\alpha}\Gamma^{ij}q_{j,\alpha}\bar{Q}_k^{\beta}\Gamma'^{kl}q_{l,\beta} \tag{2.18}$$

$$\bar{Q}_i^{\alpha}\Gamma^{ij}q_j^{\beta}\bar{Q}_{k,\beta}\Gamma'^{kl}q_{l,\alpha} \tag{2.19}$$

Eq. (2.18) indicates that the 4-quark operator induces no color mixing between the mesons while the 4-quark operator in Eq. (2.19) mixes color indices between the incoming and outgoing mesons. The operator Γ and Γ' are gamma matrices, where we define using the chiral basis,

$$\Gamma = \left\{R, L, R\gamma^{\mu}, L\gamma^{\mu}, \frac{1}{2}\sigma^{\mu\nu}\right\}. \tag{2.20}$$

There are 10 combinations where the Lorentz indices of the bilinears contract. Multiplying that by the two ways to contract color indices, results in twenty effective 4-quark operators. However, not all of these operators are linearly independent. To explore the linear dependence in more detail, it is beneficial to first introduce the Takahashi notation [53]. By suppressing the Dirac indices, let Eq. (2.18) and (2.19) be rewritten in the following form.

$$\bar{Q}_i^\alpha \Gamma^{ij} q_{j,\alpha} \bar{Q}_k^\beta \Gamma'^{kl} q_{l,\beta} \to \quad (\Gamma)\,[\Gamma'] \tag{2.21}$$

$$\bar{Q}_i^\alpha \Gamma^{ij} q_j^\beta \bar{Q}_{k,\beta} \Gamma'^{kl} q_{l,\alpha} \to \quad [\Gamma]\,[\Gamma') \tag{2.22}$$

The parenthesis and brackets represent the color index while the Lorentz index is explicitly shown when choosing a particular Γ. Since the 4-quark operator is a produce of Dirac bilinears, the 20 operators may be related by performing a chiral Fierz transformation.[1] The chiral Fierz identities are

$$(\Gamma^A)[\Gamma^B] = \frac{1}{4}\mathrm{Tr}[\Gamma^A \Gamma_C \Gamma^B \Gamma_D](\Gamma^D][\Gamma^C) \tag{2.23}$$

where Γ^A is given by Eq. 2.20 and $\{\Gamma_A\} = \left\{R, L, L\gamma_\mu, R\gamma_\mu, \frac{1}{2}\sigma_{\mu\nu}\right\}$ is the dual basis. The Fierz transformation maps ten operators from one set of color contractions to the remaining ten, resulting in ten independent operators.

The remaining ten operators may be reduced to eight by commuting the bilinears. In particular $(L)[R] \to (R)[L]$ and $(\gamma_\mu L)[\gamma^\mu R] \to (\gamma_\mu R)[\gamma^\mu L]$ are the two cases for this rearrangement symmetry.

The remaining eight operators may be reduced to five by noting that QCD has parity invariance. Under parity the anti-symmetric tensor operator vanishes while the left projection operator transforms into the right projection operator [21].

As a result, the D-meson mixing matrix elements are completely defined by a basis of five operators. For this work, the operators are chosen to be the following:

$$\mathcal{O}_1 = \bar{Q}_i^\alpha R_{ij} \gamma^\mu_{jk} q_k^\alpha \bar{Q}_l^\beta R_{lm} \gamma^\mu_{mn} q_n^\beta \tag{2.24}$$

$$\mathcal{O}_2 = \bar{Q}_i^\alpha L_{ij} q_j^\alpha \bar{Q}_k^\beta L_{kl} q_l^\beta \tag{2.25}$$

$$\mathcal{O}_3 = \bar{Q}_i^\alpha L_{ij} q_j^\beta \bar{Q}_k^\beta L_{kl} q_l^\alpha \tag{2.26}$$

$$\mathcal{O}_4 = \bar{Q}_i^\alpha L_{ij} q_j^\alpha \bar{Q}_k^\beta R_{kl} q_l^\beta \tag{2.27}$$

$$\mathcal{O}_5 = \bar{Q}_i^\alpha L_{ij} q_j^\beta \bar{Q}_k^\beta R_{kl} q_l^\alpha \tag{2.28}$$

In particular, we can recognize $\mathcal{O}_1$ as having two copies of the SM V-A weak current structure. Some early papers have called this the "SUSY basis", even though the choice has little to do with supersymmetry. In fact, these five operators are sufficient for all new physics models.

---

[1] For this particular project, the Dirac matrices are given in the DeGrand-Rossi basis. As a consequence, when explicitly calculating the Fierz transformations $\mathrm{Tr}\left\{R\sigma_{\mu\nu}\sigma_{\rho\tau}\right\} = 2\left(\eta_{\mu\rho}\eta_{\nu\tau} - \eta_{\mu\tau}\eta_{\nu\rho} \pm \epsilon_{\mu\nu\rho\tau}\right)$ and $\mathrm{Tr}\gamma^\mu\gamma^\nu\gamma^\rho\gamma^\tau\gamma^5 = -4\epsilon^{\mu\nu\rho\tau}$. The Dirac matrix also has the special property of being Hermitian in all four components.

Chapter 3

Numerical simulation

3.1 Building QCD on the lattice

Lattice QCD is currently the only non-perturbative approach for calculations in the strong-coupling regime. Lattice QCD naturally introduces a ultraviolet and infrared cutoff defined by the lattice spacing a and box size L respectively. On the lattice, matrix elements are calculated using the Euclidean path integral formulation. For a composite operator $\hat{\mathcal{O}}$, the vacuum expectation value of operator $\hat{\mathcal{O}}$ is given by the following integral,

$$\left\langle \Omega \middle| \hat{\mathcal{O}} \middle| \Omega \right\rangle = \frac{\int [d\psi][d\bar{\psi}][dA_\mu]\hat{\mathcal{O}}(\psi,\bar{\psi},A_\mu)e^{-S_{\mathrm{QCD}}(\psi,\bar{\psi},A_\mu)}}{\int [d\psi][d\bar{\psi}][dA_\mu]e^{-S_{\mathrm{QCD}}(\psi,\bar{\psi},A_\mu)}}. \tag{3.1}$$

Upon placing Eq. (3.1) on the lattice, the integral becomes approximately a $N_{\mathrm{color}} \times N_{\mathrm{spin}} \times N_x^3 \times N_t$ dimension integration problem. Therefore, currently the only feasible numerical technique that solves this problem is the Monte Carlo algorithm. The current project uses the RHMC algorithm, which is a Monte Carlo algorithm with variable step-size aiding faster convergence. Details of the RHMC algorithm are explained in Ref. [10].

The lattice calculations approximate the weighted average (integral) shown in Eq. (3.1) as a simple average over a Boltzmann distributed set of configurations as the following,

$$\frac{1}{Z}\int \hat{\mathcal{O}}e^{-S_{\mathrm{QCD}}} \to \frac{1}{N}\sum_{n=1}^{N}\hat{\mathcal{O}}(A_n) \tag{3.2}$$

where the gauge fields A_n are distributed as

$$A_n \sim e^{-S_{\mathrm{QCD}}}. \tag{3.3}$$

In the infinite data limit of $N \to \infty$, the sum becomes an integral while in practice, the finite number of sample introduces statistical errors to the analysis.

The Fermion action is first integrated out algebraically to avoid having to

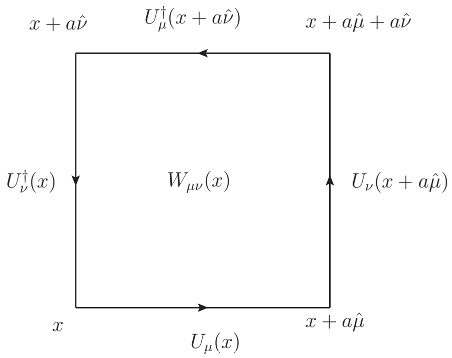

Figure 3.1: The plaquette is a 1 × 1 Wilson loop. To relate the plaquette to $F^2_{\mu\nu}$, the index x runs over all lattice sites, while μ and ν point in orthogonal directions in 4-dimensional Euclidean spacetime.

numerically integrate Grassman numbers,

$$\int [d\psi][d\bar{\psi}][dU]e^{-S_{\text{QCD}}} = \int [d\psi][d\bar{\psi}][dU]e^{-S_U - S_{\text{F}}} \tag{3.4}$$

$$= \int [d\psi][d\bar{\psi}][dU]e^{-S_U - \int d^4x\bar{\psi}(\not{D}+m)\psi} \tag{3.5}$$

$$= \det(\not{D} + m) \int [dU]e^{-S_U} \tag{3.6}$$

where $\not{D} + m$ is the Dirac operator and S_U is the SU(3) gauge action. The simplest gauge action S_U is the sum over all plaquettes on the lattice,

$$S_U = \frac{2}{g^2} \sum \text{ReTr}(1 - W_{\mu\nu}(x)) \tag{3.7}$$

where the plaquette $W_{\mu\nu}$ is

$$W_{\mu\nu} = U_\mu(x)U_\nu(x + a\hat{\mu})U^\dagger_\mu(x + a\hat{\nu})U^\dagger_\nu(x) \tag{3.8}$$

as shown in Fig. 3.1, and $U_\mu(x) = \exp(iaA_\mu(x))$ are the link fields. Taylor expanding $A_\nu(x + a\hat{\nu}) \simeq A_\nu(x) + a\partial_\mu A_\nu$, and then expanding around small values of a yields,

$$S_U = \frac{a^4}{g^2} \sum F^2_{\mu\nu}(x) \tag{3.9}$$

$$\lim_{a\to 0} S_U = \frac{1}{g^2} \int d^4x F^2_{\mu\nu}(x), \tag{3.10}$$

which up to leading order is the kinetic term of the gauge fields in the continuum limit. The action used for this project is improved up to O(a^2) and therefore includes terms beyond just the plaquette.

A more detailed discussion on the gauge and fermion lattice actions are given in Appendix A and B respectively. It is important to note that the determinant of the Dirac operator is a function of the gauge links, therefore the Monte Carlo update is required to evaluate the determinant at every step in the trajectory. While many optimizations and simplifications have been made to make this calculation feasible, this remains the most computational expensive aspect of this project.

3.2 Gauge configurations

This project uses the MILC collaboration's $N_f = 2 + 1$ asqtad ensembles with Lüscher-Weisz gluons, both of which are $O(a^2)$ improved actions [10]. The asqtad action is also tadpole improved which renormalizes the gauge couplings and greatly improves the rate of convergence during Monte Carlo runs [46]. A more in-depth discussion on the actions is given in Appendix A and B.2. In particular, since the asqtad action is not doubler-free, MILC takes the 4th-root of the fermion determinant such that it is weighted properly to reflect a theory with one taste. This procedure leads to violations of unitarity and locality and therefore has made people worry [27][26][28]. However, the asqtad action still has a properly defined chiral symmetry with massless Goldstone bosons as discussed in detail in Appendix B.2. On the other hand, the chiral-extrapolation of the matrix elements is never taken to the $m_q \to 0$ limit, and instead is only taken to $m_q = m_u$, the physical up-quark mass. Therefore the issue at $m_q = 0$ is circumvented.

The full dataset is shown in FIG. 3.2(left) with details tabulated in Tab. F.1. We use ensembles where pions in the pion cloud have masses ranging from 176 MeV to 557 MeV across four lattice spacings. The light quarks use the same lattice action as the sea quarks, however for each sea quark ensemble, partially-quenched data sets are generated at seven to eight different valence quark masses. Referring to Fig. 3.2(right), dots of the same color and shade are valence quark propagators with different masses evaluated on the same gauge ensembles. Table F.2 tabulates the list of valence light quark masses analyzed in this project. The black line running diagonally in Fig. 3.2 intersects with datasets where the sea and valence light quarks have the same mass. All other datasets are partially quenched. The advantage of generating partially quenched datasets are because the implementation is numerically straightforward and computationally cheap, yielding more statistics for very little work. Table F.1 also show that most ensembles have volumes $\gtrsim 4 m_\pi L$ to minimize finite volume effects [32]. The valence quark masses are listed in Table F.2.

For the valence heavy-quark propagators, we use the Sheikoleslami-Wohlert action with the Fermilab interpretation [35]. We fix the mass of the heavy charm quark to the physical value of the spin-averaged D_s mass as discussed in [17]. The tadpole-improved bare charm quark masses chosen during the time of simulation are tabulated in Table F.13, parametrized by the hopping parameter κ_c.

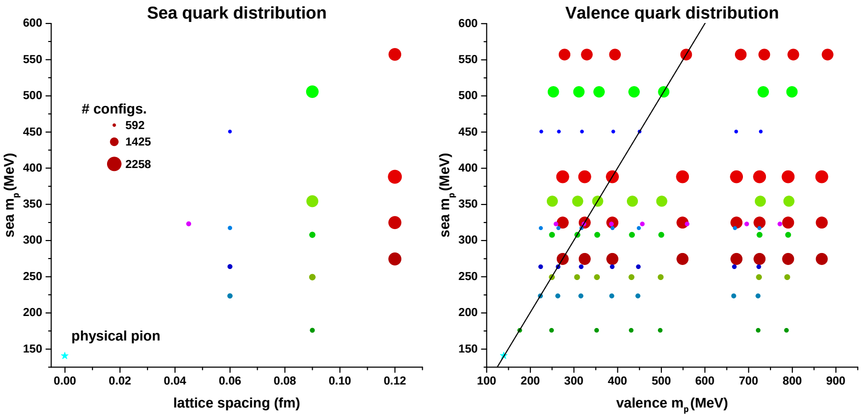

Figure 3.2: Left: MILC asqtad ensembles used for the analysis. The colors label (red) 12 fm, (green) 0.09 fm, (blue) 0.06 fm, (purple) 0.045 fm, with darker hues corresponding to lighter pion masses. The physical pion resides at the cyan star. The size of the circle are proportional to the number of configurations, ranging from 592 to 2258. Right: Valence light-quark propagators used for the analysis expressed in pion mass. Datasets with the same sea masses are generated on the same MILC ensembles. The diagonal line passes through $m_{\text{sea}} = m_{\text{valence}}$ with multiple partially-quenched points on either side.

3.3 From gauge ensembles to quark propagators

With the gauge configurations available, we may generate quark propagators by building the Dirac operator from the gauge links $U_{x,\mu}$. This is because, on the lattice, derivatives become covariant difference operators defined by the connection $U_{x,\mu}$. Therefore the corresponding Dirac operator for any lattice action is a function of the gauge links. For this project, the light quarks are described by the asqtad action and the heavy quark is described by the improved Wilson action. Both actions are discussed in detail in Appendix B.2 and B.1.

Propagators are generated on the lattice by numerically inverting the lattice Dirac operator. We use one-to-all propagators, where instead of inverting the entire Dirac matrix: we only invert one row, describing propagators with their sources at the origin, propagating to all other points on the lattice. This is required because while the matrix is sparse, inverting one that is so large is computationally unfeasible. While the problem of generating propagators is a very interesting and rich research topic, the propagators for this project are already available and therefore I will not go into more detail on the algorithms used for matrix inversions.

3.4 Matrix elements on the lattice

On the lattice, mesons are created and annihilated via the interpolating operators,

$$D = \bar{q}^{\alpha}\gamma_5 Q^{\alpha}(x), \tag{3.11}$$

$$\bar{D} = \bar{Q}^{\alpha}\gamma_5 q^{\alpha}(x). \tag{3.12}$$

The interpolation operators generate mesons with the correct valence quark masses and pseudoscalar spin structure. There is no restriction on the radial quantum number however, therefore the creation operator generates an infinite tower of excited states when acting on the vacuum state,

$$D\left|\Omega\right\rangle = \sum_n e^{-E_n t}\left|n\right\rangle. \tag{3.13}$$

Excited state contributions are removed through the fit procedure that is addressed in detail in Chapter 4. The meson two-point correlators are constructed from the interpolating operators, and provide important data for resolving the coefficients of the correlator fits, as well as additional information on the meson masses detailed in Appendix D. From the 4-quark operators Eqs. (2.24–2.28) and the interpolation operators Eqs. (3.11) (3.12), the two- and three-point correlators are time-ordered vacuum expectation values,

$$C^{\text{2pt}}(x,0) = \left\langle T\left\{\bar{D}(x)D(0)\right\}\right\rangle, \tag{3.14}$$

$$\langle\mathcal{O}_i\rangle \equiv C_i^{\text{3pt}}(x_1,x_2,0) = \left\langle T\left\{D(x_2)\mathcal{O}_i(0)D(x_1)\right\}\right\rangle, \tag{3.15}$$

where $i = 1,2,3,4,5$ correspond to the set of 4-quark operators.

The meson correlators are generated by Wick contracting the quark fields, and forming quark propagators. For example, for the two-point function,

$$C^{\text{2pt}}(x) = \langle D(x)|D(0)\rangle \tag{3.16}$$

$$= \left\langle T\{\bar{q}_i^{\alpha}(x)\gamma_5^{ij}Q_j^{\alpha}(x)\bar{Q}_k^{\beta}(0)\gamma_5^{kl}q_l^{\beta}(0)\right\rangle \tag{3.17}$$

$$= -\left\langle q_l^{\beta}(0)\bar{q}_i^{\alpha}(x)\right\rangle\gamma_5^{ij}\left\langle Q_j^{\alpha}(x)\bar{Q}_k^{\beta}(0)\right\rangle\gamma_5^{kl} \tag{3.18}$$

$$= -L_{li;0x}^{\beta\alpha}\gamma_5^{ij}H_{jk;x0}^{\alpha\beta}\gamma_5^{kl} \tag{3.19}$$

$$= -\operatorname{Tr}_{\text{color,spin}}\left\{L_{0x}H_{0x}^{\dagger}\right\} \tag{3.20}$$

where for the last line, we invoke γ_5-Hermiticity so that the source for both the light and heavy quark propagator is at the origin. We Fourier transform the correlators to zero momentum to get,

$$C^{\text{2pt}}(t) = -\sum_{\vec{x}}\operatorname{Tr}_{\text{color,spin}}\left\{L_{0x}H_{0x}^{\dagger}\right\} \tag{3.21}$$

Similarly, the three-point correlator may be derived in the same way. Defining the "open meson propagator",

$$E_{il}^{\alpha\gamma}(x_1,x_2) \equiv H_{ij}^{\alpha\beta}(x_1,x_2) L_{jk}^{\dagger\beta\gamma}(x_1,x_2)\gamma_5^{kl}, \tag{3.22}$$

the Wick contractions is conveniently categorized for operators $\{1,2,4\}$ and $\{3,5\}$ by their separate color structure. Again, we Fourier transform the correlators to zero momentum yielding,

$$\begin{aligned}
C_i^{3pt}(t_1,t_2) &= \sum_{\vec{x}_1,\vec{x}_2} \langle D(x_2)\left|\mathcal{O}_{1,2,4}(0)\right| D(x_1)\rangle \\
&= \sum_{\vec{x}_1,\vec{x}_2} \Big[\mathrm{Tr}_{\text{color,spin}}\left\{E(0;x_1)\Gamma_i^{(1)}\right\} \times \mathrm{Tr}_{\text{color,spin}}\left\{E(0;x_2)\Gamma_i^{(2)}\right\} \\
&+ \mathrm{Tr}_{\text{color,spin}}\left\{E(0;x_1)\Gamma_i^{(2)}\right\} \times \mathrm{Tr}_{\text{color,spin}}\left\{E(0;x_2)\Gamma_i^{(1)}\right\} \\
&- \mathrm{Tr}_{\text{color,spin}}\left\{E(0;x_1)\Gamma_i^{(1)}E(0;x_2)\Gamma_i^{(2)}\right\} \\
&-\mathrm{Tr}_{\text{color,spin}}\left\{E(0;x_1)\Gamma_i^{(2)}E(0;x_2)\Gamma_i^{(1)}\right\}\Big],
\end{aligned} \tag{3.23}$$

$$\begin{aligned}
C_i^{3pt}(t_2,t_1) &= \sum_{\vec{x}_1,\vec{x}_2} \langle D(x_2)\left|\mathcal{O}_{3,5}(0)\right| D(x_1)\rangle \\
&= \sum_{\vec{x}_1,\vec{x}_2} \Big[\mathrm{Tr}_{\text{color}}\left\{\mathrm{Tr}_{\text{spin}}\left[E(0;x_1)\Gamma_i^{(1)}\right] \times \mathrm{Tr}_{\text{spin}}\left[E(0;x_2)\Gamma_i^{(2)}\right]\right\} \\
&+ \mathrm{Tr}_{\text{color}}\left\{\mathrm{Tr}_{\text{spin}}\left[E(0;x_1)\Gamma_i^{(2)}\right] \times \mathrm{Tr}_{\text{spin}}\left[E(0;x_2)\Gamma_i^{(1)}\right]\right\} \\
&- \mathrm{Tr}_{\text{spin}}\left\{\mathrm{Tr}_{\text{color}}\left[E(0;x_1)\Gamma_i^{(1)}\right] \times \mathrm{Tr}_{\text{color}}\left[E(0;x_2)\Gamma_i^{(2)}\right]\right\} \\
&-\mathrm{Tr}_{\text{spin}}\left\{\mathrm{Tr}_{\text{color}}\left[E(0;x_1)\Gamma_i^{(2)}\right] \times \mathrm{Tr}_{\text{color}}\left[E(0;x_2)\Gamma_i^{(1)}\right]\right\}\Big].
\end{aligned} \tag{3.24}$$

3.4.1 Heavy quark smearing

For the D-meson interpolating operator, the heavy quark can be smeared in order to have more overlap with the ground state at the expense of weaker excited state signals. Since we are only interested in extracting the ground state matrix element, this is beneficial. Eq. (3.25) demonstrates how smearing is implemented,

$$\bar{D}^{\text{smear}}(t,\mathbf{x}) = \sum_{\mathbf{x}'} \bar{Q}(t,\mathbf{x}')S(\mathbf{x},\mathbf{x}')\gamma_5 q(t,\mathbf{x}) \tag{3.25}$$

where $S(\mathbf{x},\mathbf{x}')$ is the smearing function, where setting $S(\mathbf{x},\mathbf{x}') = \delta^{(3)}(\mathbf{x}-\mathbf{x}')$ results in the previously discussed unsmeared correlators. For larger overlaps with the ground state, $S(\mathbf{x},\mathbf{x}')$ is set to the 1S wavefunction of the Richardson potential [54]. The Richardson potential is a phenomenological heavy quark potential that combines asymptotic freedom with linear quark confinement. Its ground-state wavefunction has been shown to give greater overlap with the ground state of the charm when compared to a local operator [52]. We revalidate this finding in Section 4.

3.4.2 Tree-level heavy-quark improvement

The heavy quark spinors on the lattice have discretization errors starting at O(a) which enter into the operators. Following Ref. [35], the continuum 4-quark operator is reconstructed as a sum of infinite lattice operators,

$$\mathcal{O}^{\text{cont.}} = Z_{\mathcal{O}}(\{m_0 a\}, g_0^2)\left[\mathcal{O}_0^{\text{lat.}} + \sum_n C_n(\{m_0 a\}, g_0^2)\mathcal{O}_n^{\text{lat.}}\right], \tag{3.26}$$

where the coefficients $Z_{\mathcal{O}}$ and C_n can be expanded around the gauge coupling g_0^2,

$$Z_{\mathcal{O}}(\{m_0 a\}, g_0^2) = \sum_{l=0}^{\infty} g_0^{2l} Z_{\mathcal{O}}^{[l]}(\{m_0 a\}), \tag{3.27}$$

$$C_n(\{m_0 a\}, g_0^2) = \sum_{l=0}^{\infty} g_0^{2l} C_n^{[l]}(\{m_0 a\}). \tag{3.28}$$

Therefore, at tree-level where $l = 0$ and leading-order where $n = 0$, the lattice operator and continuum operator differ only by a normalization factor $Z_{\mathcal{O}}^{[0]}$. On the other hand, the continuum spinor is relativistically normalized as $u_{\text{rel}}(\xi, \mathbf{p})\sqrt{m_q/E}$ where the normalization $\sqrt{m_q/E} = 1$ for $\mathbf{p} = 0$. On the lattice, the spinor is normalized as $u_{\text{lat}}(\xi, \mathbf{p})\mathcal{N}(\mathbf{p})$. The variable ξ labels the four solutions to the lattice Dirac equation, while the normalization $\mathcal{N}(\mathbf{p})$ is fixed by working out the anti-commutation relation of the lattice fermion fields. By inserting the mode expansion for the fields, using the anti-commutation relations for the creation and annihilation operators, and finally Fourier transforming to momentum space, $\mathcal{N}(0) = e^{-M_1 a/2}$ where M_1 is the rest mass of the heavy-quark as defined in Appendix B.1.2. Therefore, choosing $Z_{\mathcal{O}}^{[0]} = 1$, which fixes a preferred normalization convention, the lattice matrix element is the same as the continuum matrix element for small values of $\mathbf{p}$ if we multiply $e^{M_1 a/2}$ for each instance of a Fermilab-type Wilson spinor.

For tree-level improvement of light-quarks which we define here as $m_q a \ll 1$, the normalization factor is all that is required. However, for heavy-quarks where $m_a q \gg 1$, more care is needed. Expanding around small momentum, the heavy quark spinor on the lattice is,

$$u_{\text{lat}}(\xi, \boldsymbol{p}) = e^{-M_1 a/2}\left[1 - \frac{i\zeta\boldsymbol{\gamma}\cdot\boldsymbol{p}a}{2\sinh M_1 a} - \mathcal{O}(\boldsymbol{p}^2)\right] u(\xi, \boldsymbol{0}). \tag{3.29}$$

In the continuum, the heavy quark spinor expanded around small momentum is,

$$u_{\text{rel.}}(\xi, \boldsymbol{p}) = \left[1 - \frac{i\boldsymbol{\gamma}\cdot\boldsymbol{p}}{2m_q} - \mathcal{O}(\boldsymbol{p}^2)\right] u(\xi, \boldsymbol{0}). \tag{3.30}$$

The heavy quark spinor on the lattice is matched to the continuum spinor by matching Eq. (3.29) with Eq. (3.30). By absorbing the normalization factor in Eq. (3.29) into the wavefunction renormalization, the heavy quark fields ψ are tree-level improved by rotating the fields,

$$\Psi = [1 + ad_1\boldsymbol{\gamma}\cdot\boldsymbol{D}]\,\psi. \tag{3.31}$$

The factor

$$d_1 = \frac{1}{2 + m_0 a} - \frac{1}{2(1 + m_0 a)}, \tag{3.32}$$

and is derived by setting the quark mass m_q to the kinetic mass M_2, imposing axis-interchange symmetry and substituting Eq. (B.17, B.18) for M_1 and M_2 respectively. We can see immediately that for $m_0 a \ll 1$, $d_1 \simeq 0$, therefore only the normalization $\mathcal{N}(0)$ and the rotation defined in Eq. 3.31 are needed to tree-level improve the heavy-quarks without additional operators. The two- and three-point composite operators are tree-level improved by substituting the heavy quark field ψ by the rotated field Ψ. This step was performed during the data generation process.

3.5 Folding

Due to the periodic boundary conditions in time, there are backwards propagating waves in the correlators. Using combined parity-inversion and time-reversal invariance, the backward propagating signal may be included in order to gain approximately a factor of two in statistics. We will refer to this as “folding”.

On a lattice with time dimension of length T, we have lattice sites at $t = \{0, ..., T-1\}$. The signal is sourced at $t = 0$ while at $\mathcal{O}(T)$, the source is at $t = T$. Under this definition, the two-point correlators are folded by taking

$$C^{\text{2pt}}_{\text{folded}}(t) = \frac{C^{\text{2pt}}(t) + C^{\text{2pt}}(T-t)}{2}. \tag{3.33}$$

We focus on the subset of the two-point data where $0 \leq t \leq T/2$ to damp the backward propagating signal by $\exp(-[T-t])$ as shown in Appendix D.

For the three-point correlator, the 4-quark operator is placed at $t = 0$, with the D- and $\bar{D}$-meson placed at $t = t_1 < 0$ and $t = t_2 > 0$ respectively on each sides. For a lattice of time length T, where $t_1 = \{-T, ..., -1\}$ and $t_2 = \{0, ..., T-1\}$, the correlator is folded by taking

$$C^{\text{3pt}}_{\text{folded}}(-|t_1|, t_2) = \frac{C^{\text{3pt}}(-|t_1|, t_2) + C^{\text{3pt}}(-[T-|t_1|], T-t_2)}{2}. \tag{3.34}$$

For the analysis, the quadrant of the t_1–t_2 plane is focused on where $|t_1| < T/2$

and $t_2 < T/2$ in order to avoid both backward propagating and tetraquark-like signals, and is discussed in detail in Appendix D.

3.6 Parity equivalent operators

We increase statistics by combining parity equivalent operators together into a larger data set since they are statistically distinguishable. The following three-point correlators and their parity equivalent partners are show in Eq. (3.35).

$$\begin{aligned}\langle \mathcal{O}_1 \rangle &\overset{p}{=} \langle \mathcal{O}_{10} \rangle \,, \\ \langle \mathcal{O}_2 \rangle &\overset{p}{=} \langle \mathcal{O}_8 \rangle \,, \\ \langle \mathcal{O}_3 \rangle &\overset{p}{=} \langle \mathcal{O}_9 \rangle \,, \end{aligned} \tag{3.35}$$

where the parity-equivalent operators correspond to taking $L \leftrightarrow R$,

$$\mathcal{O}_{10} = \bar{Q}_i^\alpha L_{ij} \gamma^\mu_{jk} q_k^\alpha \bar{Q}_l^\beta L_{lm} \gamma^\mu_{mn} q_n^\beta, \tag{3.36}$$

$$\mathcal{O}_8 = \bar{Q}_i^\alpha R_{ij} q_j^\alpha \bar{Q}_k^\beta R_{kl} q_l^\beta, \tag{3.37}$$

$$\mathcal{O}_9 = \bar{Q}_i^\alpha R_{ij} q_j^\beta \bar{Q}_k^\beta R_{kl} q_l^\alpha. \tag{3.38}$$

The SM operators are combined with their parity partners, effectively doubling the amount of data. Fig. 3.3 compares the relative error of the coarse 0.2ms ensemble for $\mathcal{O}_1$ versus $(\mathcal{O}_1 + \mathcal{O}_{10})/2$. The relative error on the parity combined dataset is smaller by a factor of ~ 1.33. This is slightly lower than $\sqrt{2}$, which is the amount the error would have decreased if the data was uncorrelated. Therefore, it is advantageous to exploit this symmetry to gain more statistics.

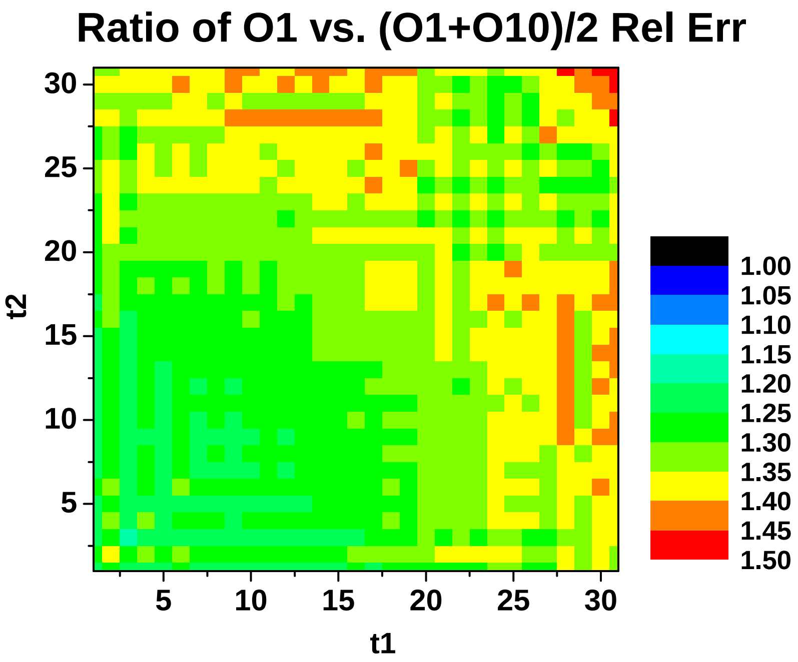

Figure 3.3: Ratio of relative errors between $\mathcal{O}_1$ and $(\mathcal{O}_1 + \mathcal{O}_{10})/2$. The axis labels t_1 the source of the D-meson, t_2 the sink of the $\bar{D}$-meson, with the 4-quark operator at $t = 0$. The colors represent the ratio of the relative errors between the $\mathcal{O}_1$ correlator versus the parity-average correlator $(\mathcal{O}_1 + \mathcal{O}_{10})/2$. Most of the region is green, indicating at the parity-averaged correlators have errors that are smaller by approximately a factor of $1/\sqrt{2}$, suggesting that the sample size has doubled.

Chapter 4

Correlator Fits

4.1 Correlator fit requirements

Two- and three-point data analysis extracts the hadronic matrix element by applying the methods of Bayesian constraint curve fitting as described in Appendix E. In order for the fit parameters to guide the χ^2 minimization without introducing systematic errors, a consistent method is used to determined all fit parameters involved in the analysis. An exhaustive list of the fit parameters that need to be assigned and the target characteristics for each category are listed in Table 4.1. The following sections will outline the techniques and process that are used to determine all the fit parameters listed above.

Priors	A set of priors (central value and width) for every parameter (E's, Z's, and matrix element O's) in the fit function that is valid for every ensembles within one lattice spacing is needed. Using the same set of priors for each lattice spacing avoids systematic errors resulting from over-fitting the data.
Fit Ranges	One set of t_{min} and t_{max}, indicating a subset of both the two and three point correlator data needs to be determined. The physical length of t_{min} and t_{max} is fixed or smoothly varying across all ensembles to avoid introducing systematic errors.
Number of States	A common N_s large enough to describe the radially excited states is needed for both the two and three point fit function.
Smearing	The type(s) of source and sink smearing performed on the two- and three-point data needs to be consistent across all ensembles.

Table 4.1: Exhaustive List of Fit Parameters

4.2 Correlator fit functions

The two- and three-point correlator data are fitted with the fit functions outlined in Appendix D,

$$\begin{aligned} C^{2\text{pt}}(t) &= \sum_{n=0}^{N_s} (-1)^{n(t+1)} \frac{\left|Z_n\right|^2}{2E_n} \left(e^{-E_n t} + e^{-E_n(T-t)}\right), \quad (4.1) \\ C_i^{3\text{pt}}(t_1, t_2) &= \sum_{m,n=0}^{N_s} (-1)^{n(t_2+1)} (-1)^{m(|t_1|+1)} \frac{\langle n\left|\mathcal{O}_i\right| m\rangle Z_n^\dagger Z_m}{4E_n E_m} e^{-E_n t_2} e^{-E_m|t_1|}. \quad (4.2) \end{aligned}$$

The even and odd states describe the interaction of the $J^P = 0^-$ and $J^P = 0^+$ D-mesons respectively. The fit functions used in the analysis reparameterizes Eq. (4.1, 4.2) to avoid ill-defined parameter combinations. Setting $\tilde{Z}_n^2 \equiv Z_n/\sqrt{2E_n}$, $\tilde{O}_{00} \equiv \frac{\langle 0|\mathcal{O}_i|0\rangle}{2E_0}$, and $\tilde{O}_{nm} = \frac{\langle n|\mathcal{O}_i|m\rangle Z_n^\dagger Z_m}{4E_n E_m}$ for $n, m \neq 0$, the fit functions become,

$$\begin{aligned} C^{2\text{pt}}(t) &= \sum_{n=0}^{N_s} (-1)^{n(t+1)} \left|\tilde{Z}_n^2\right|^2 \left(e^{-E_n t} + e^{-E_n(T-t)}\right), \quad (4.3) \\ C_i^{3\text{pt}}(t_1, t_2) &= \left|\tilde{Z}_0^2\right|^2 \tilde{O}_{i;00} e^{-E_0 t_2} e^{-E_0|t_1|} \\ &\quad + \sum_{m,n\neq 0}^{N_s} (-1)^{n(t_2+1)} (-1)^{m(|t_1|+1)} \tilde{Z}_n^2 \tilde{Z}_m^2 \tilde{O}_{i;nm} e^{-E_n t_2} e^{-E_m|t_1|}. \quad (4.4) \end{aligned}$$

I define the ground state as having the energy E_0, while the first excited state corresponds to the ground state scalar state, and is parametrized as a splitting from the ground state $E_1 \equiv E_0 + \ln(\Delta E_{1,0})$ where $\Delta E_{i,j} \equiv \exp(E_i - E_j)$. The exponential ensures that the splitting is positive, enforcing a strict hierarchy of states. I next construct two towers of excited states based on the pseudoscalar ground state E_0 and the scalar ground state E_1 where $E_n \equiv E_{0(1)} + \sum_{i=2(3)}^{n} \ln\left(\Delta E_{i,i-2}\right)$ where the sum is over even (odd) states respectively for E_0 and E_1. Fig. 4.1 schematically shows how the priors are organized as two towers of excited states.

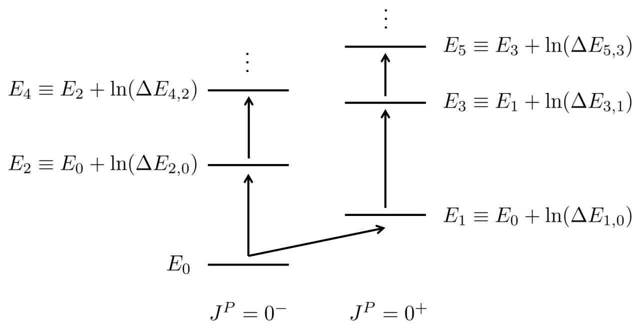

Figure 4.1: Correlators are fit to two independent towers of excited states.

Note that Eq. (4.3, 4.4) share every parameter with the exception of the hadronic matrix element $\tilde{O}_{i;nm}$. Simultaneous fits to the two datasets therefore yields more stringent determinations for E_i, and also is required for the fitter to factorize $\tilde{O}_{i;00}$ from $\left|\tilde{Z}_0{}^2\right|^2 \tilde{O}_{i;00}$. However, analysis starting with exclusively the two-point data will provide valuable insight into the final correlator fits.

4.3 Two-point correlator fits

The two-point correlator data describes a D-meson being created at $t = 0$, and being annihilated at different points in time $t = \{0, 1, 2....T\}$. Referring back to Eq. (4.1), the two-point fit function is an infinite sum of radially excited states. In practice, the series may be truncated for large values of t since the exponentials are damped by the excited state masses. To gain an initial understanding of the data set, it is informative to study exclusively the ground state of the fit function. Due to the simplicity of the fit function after the truncation, it is possible to generate what are called the effective mass and scaled correlator plots.

4.3.1 Effective mass

Before fits are performed, effective mass plots are generated to estimate the ground state energy of an ensemble by taking ratios of the data. Truncating the fit function to the ground state and dropping terms of order $\mathcal{O}(\exp[-E_n T])$, Eq. (4.3) yields,

$$C^{2pt}(t) \approx \tilde{Z}_0^4 e^{-E_0 t}. \tag{4.5}$$

Taking ratios of the two-point correlator, the effective mass converges to the ground state energy at large t.

$$M_{\text{eff}} = \ln \frac{C^{2pt}(t+1)}{C^{2pt}(t)} \tag{4.6}$$

An example of an effective mass plot is shown in Fig. 4.2. For small values of t, there is an oscillating exponential decreasing trend; this signal stems from the radially excited state information contained in the two-point data. However, for $t \geq 15$ the effective mass plot converges to a stable value of approximately $M_{\text{eff}} \approx 1.03$. This motivates the selection of the ground state energy prior for this particular ensemble. Repeating the same logic, the ground state energy for every ensemble is deduced by the effective mass plots.

A table for all the effective mass values are given in Appendix F.

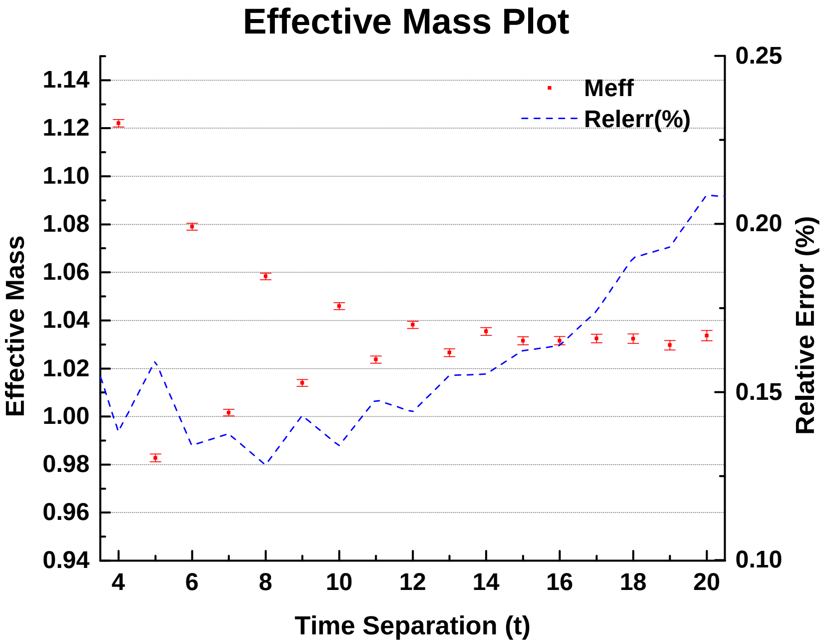

Figure 4.2: Effective mass for smeared source to smeared sink coarse 0.2ms ensemble and $\mathrm{m_{val}}$ of 0.0500.

4.3.2 Scaled correlator

The scaled correlator plots are generated to estimate the ground state prior for $\tilde{Z}_0$. Given an effective mass, M_{eff}, the scaled correlator is,

$$Z_{eff} \equiv \tilde{Z}_0^4 = C^{2pt}(t)e^{M_{eff}t}. \tag{4.7}$$

From Eq. (4.7), the central value for $\tilde{Z}_0$ is the fourth root of the scaled correlator. An example of the scaled correlator is shown in Fig. 4.3. Similar to the effective mass plot, for $t \leq 14$, the plot exhibits oscillating exponential behavior suggestion excited state contamination. For $t > 14$ the scaled correlator plateaus to a value of ≈ 1.477, motivating the selection of $\tilde{Z}_0$.

A table for all the scaled correlator values are given in Appendix F.

4.3.3 Prior selection

While the effective mass and scaled correlator plots motivate the selection of ground state $\tilde{E}$ and $\tilde{Z}$ prior central values, however the ground state prior widths and excited state parameters need to be determined as well. For setting the ground state priors, the mean and standard deviation of the effective masses and scaled correlators are calculated for each valence mass at each lattice spacing. Fig. 4.4 is an example of a summary of the effective masses pertaining to the coarse ensemble. While there are variances in the effective mass across

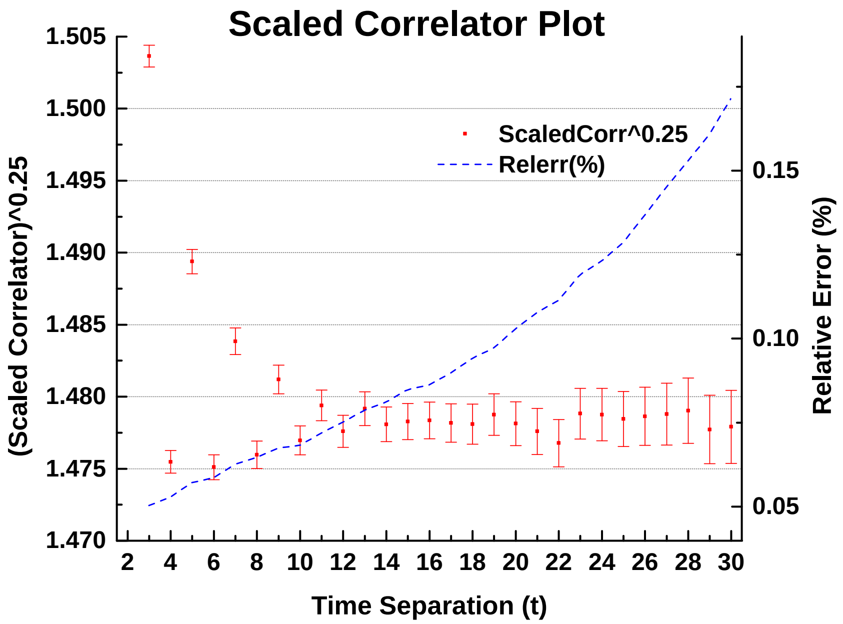

Figure 4.3: Scaled Correlator for smeared source to smeared sink coarse 0.2ms ensemble and $\mathrm{m_{val}}$ of 0.0500.

different light sea quark masses as suggested by the black error bars, there is a more prominent trend resulting from varying the light valence quark masses. Referring back to section 4, only one prior should be used in each lattice spacing to constrain all $\tilde{E}_0$'s and $\tilde{Z}_0$'s in order to avoid over-fitting the data. Therefore, the red data point in Fig. 4.4 suggests a prior wide enough to encompass all reasonable values of $\tilde{E}_0$ appearing in the coarse ensemble, while narrow enough to prevent the minimizer from wandering off into unphysical regions of parameter space. A similar plot as Fig. 4.4 is generated to determine the ground state $\tilde{Z}_0$ prior for each lattice spacing.

Excited state prior selections are motivated from experimental and theoretical predictions. The $D^0 - D^{0*}$ splitting is obtained from the Particle Data Group [14] while the radial excitations are estimated from quark models [34]. Table F.4 provides the values of the energy splittings.

As discussed in table 4.1, the goal of the priors is to guide the fitter without over-fitting the data. The finalized priors listed in Table F.5 show that priors are only varied across lattice spacing and are not tweaked from ensemble to ensemble. When employing Bayesian inference, parameters are promoted to distributions, therefore I am careful to not have over-constraining priors that introduce systematic errors.

While the initial set of priors are determined by looking at the effective mass, scaled correlator as well as input from experimental data and theoretical esti-

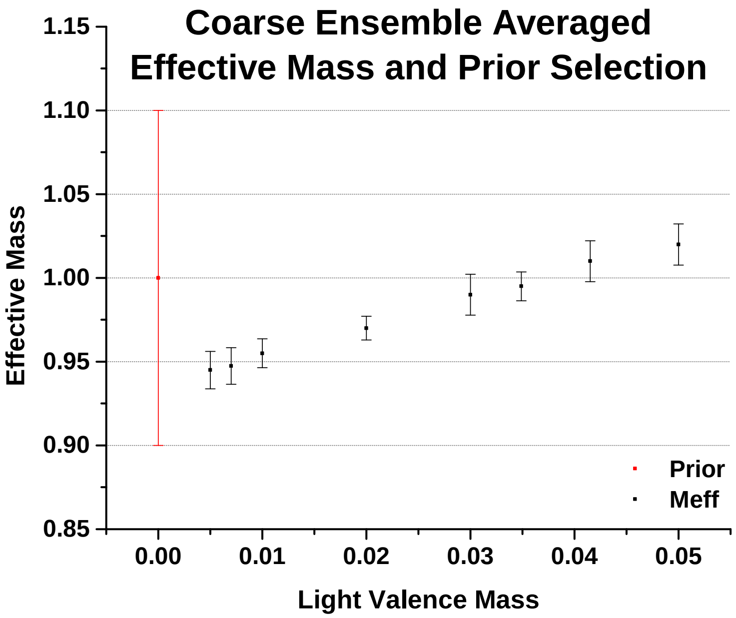

Figure 4.4: Plot for setting the ground state energy priors for the coarse ensemble with smeared source and sink.

mates. The finalized priors listed in Table F.5 have also been tested for stability under variation of fit range, number of states, and smearing. A complete list of priors used for this project are tabulated in Table F.5.

4.3.4 Fit range and number of states

The effective mass plot shown in Fig. 4.2 indicates that excited state contributions are important for data close to the source at $t = 0$. Keeping more terms better describes the excited states, but also complicates the fit and introduces possible local minima; the issues may be alleviated by introducing tighter priors but an analysis on the fit range versus the number of terms kept from Eq. (4.1) is necessary.

The fit range of the two-point correlators is illustrated by Fig. 4.5 where t_{min} and t_{max} define the 1-dimensional region where the fit is performed on.

Fig. 4.6 is a t_{min} stability plot where fits over different values of t_{min} are evaluated, and exemplifies fits to the same data set over varying number of states. For the fits involving 1+1 states (a ground state plus the opposite parity ground state fit shown in red), a systematic trend is prevalent at $t_{\mathrm{min}} < 10$ indicating that the fit function does not adequately capture excited state signals. The addition of the first excited state in the 2+2 state fit alleviates the systematic trend from excited states and stability under varying t_{min} is demonstrated. The 3+3 state fit confirms the stability seen in the 2+2 state fits, and in particular,

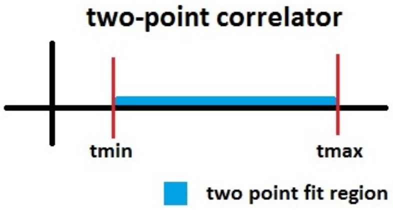

Figure 4.5: Definitions of $t_{\min}$ and $t_{\max}$ for the two-point correlator fits.

for fits at $t \geq 5$, the error bars on the 2+2 states saturate to the 3+3 state fits, indicating that the priors are not synthetically reducing the errors are they appear to be for $t \leq 4$. For the final correlator fits, 2+2 state fits are used with $t_{\min}$ chosen such that the errors have saturated.

Fig. 4.7 is the equivalent $t_{\max}$ stability plot for a representative two-point correlator fit. In general, the correlator fits are less sensitive to $t_{\max}$ because only the ground state signal remains detectable at large time slices. The errors on E_0 decrease as more data is added motivating the choice of a larger $t_{\max}$. Across all three fits, the errors have all saturated moving from 1+1 to 3+3 state fits given that an appropriate $t_{\min}$ is chosen for the 1+1 state fit. Table F.8 lists the fit ranges used for the finalized two- and three-point correlator fits.

4.3.5 Operator smearing

Operator smearing of the source and sink provides stronger overlap with the ground state at the expense of more noisy excited state signals as discussed in Section 3.4.1. Fig. 4.8 shows that the smeared operators allow for smaller $t_{\min}$ selections compared to the point source operators. Fitting towards smaller values of $t_{\min}$ yields more precise fits on the ground state parameters. Since the objective for this project is to extract the ground state D-meson mixing matrix element, enhancement of the ground state signal at the expensive of the excited state signal is desirable. The final two- and three-point correlator fits use smeared operators.

4.4 Three-point simultaneous fit

The two- and three-point fit functions share the common parameters $\tilde{Z}_n^2$ and $\tilde{E}_n$ as described by Eq. (4.3,4.4), motivating the effort for fitting both sets of data simultaneously. In particular, two-point information is necessary to resolve the $\tilde{Z}_n^2$s. While various combinations of excited states and operator smearing were explored for the three-point correlator fits as well, choices consistent with the two-point fits were made. Having the same number of excited states and smearing resulted in the overlap of the most number of parameters, which is primarily the reason for simultaneous fits.

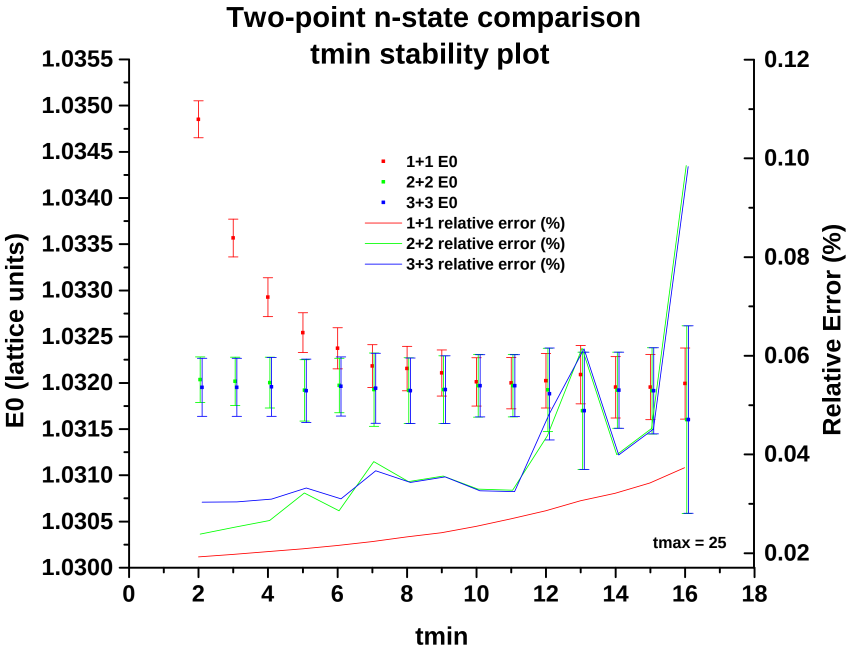

Figure 4.6: Two-point fit under varying number of excited states. Fits performed on coarse 0.2ms ensemble with m_{val}=0.0500 on smeared source/sink operators.

4.4.1 Scaled three-point and prior motivation

Before any fits are attempted, the three-point correlator may first be understood by looking at the first term in Eq. (4.4). Possessing knowledge of the shared parameters gained from the two-point fits, the leading exponential and factors of $\tilde{Z}^2$ may be factored out yielding the expression of the scaled correlator given by Eq. (4.8).

$$\mathcal{O}_{\text{eff}} = \frac{C_i^{3\text{pt}}(t_1, t_2)}{e^{-\tilde{E}_0 t_1} e^{-\tilde{E}_0 t_2} \left|\tilde{Z}_0^2\right|^2} \tag{4.8}$$

where $i = \{1, 2, 3, 4, 5\}$ denotes one of five 4-quark operators.

An example of the scaled three-point is given by Fig. 4.9. The data has periodic boundary conditions at $t = 64$, therefore what is shown is the quadrant of data closes to the $t = 0$ source. The left plot shows the central value of the scaled three point in the full $t_1 - t_2$ plane. The checkered behavior comes from the oscillating opposite parity states. The right figure plots the $|t_1| = t_2$ diagonal slice in detail with error bars as well as the magnitude of the relative errors. The excited state contributions may be seen on early time slices up to $t \sim 7$ and plateaus to the ground state value of approximately 0.115 for this ensemble. An extensive list of the ground state matrix element prior derived from the scaled three-point plots are tabulated in Appendix F.4.

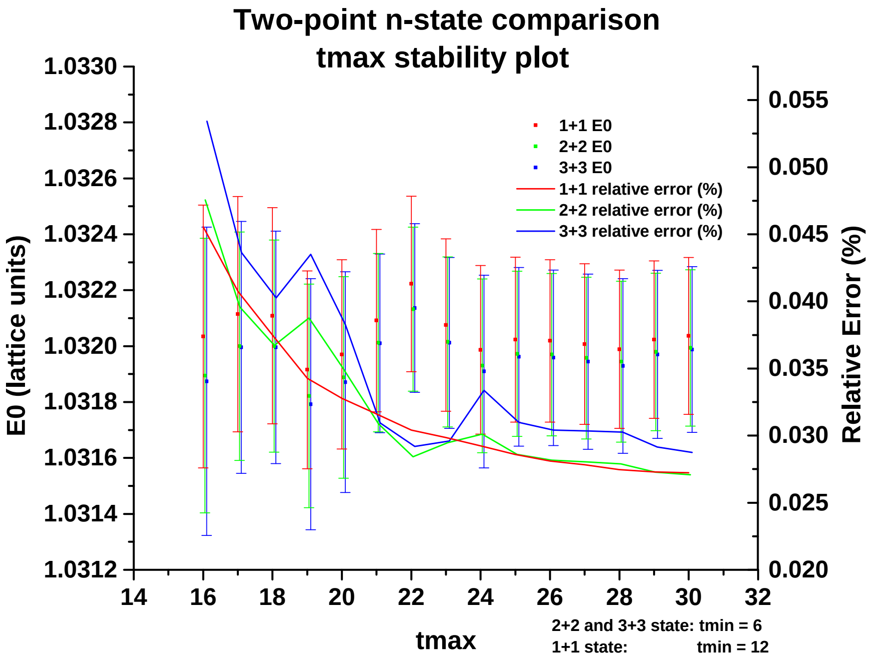

Figure 4.7: $t_{\max}$ stability plot for varying number of excited states. Fits performed on coarse 0.2ms ensemble with $\mathrm{m_{val}}$=0.0500 on smeared source/sink operators.

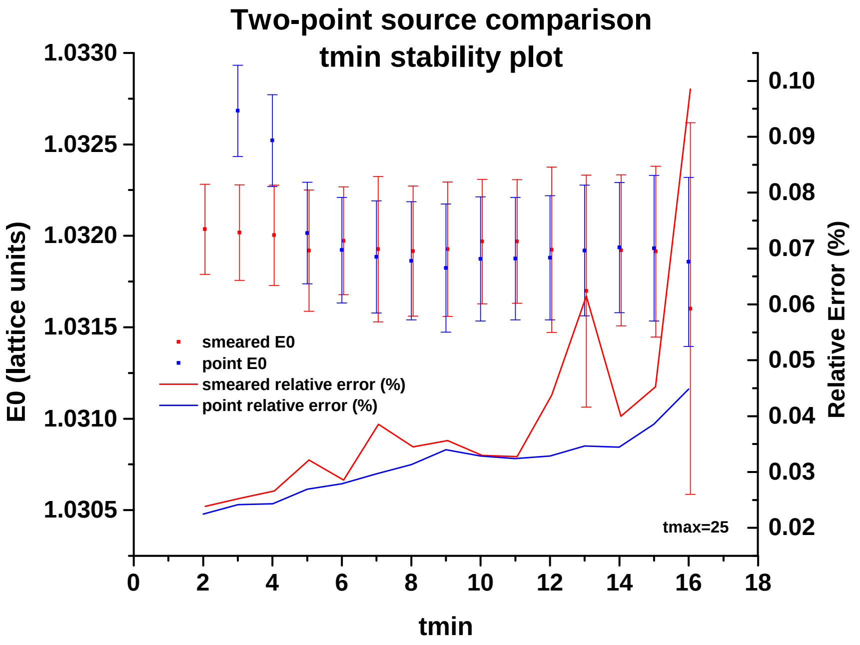

Figure 4.8: $t_{\min}$ stability plot for point and smeared source/sink two-point correlation fits. Fits performed on coarse 0.2ms ensemble with $\mathrm{m_{val}}$=0.0500.

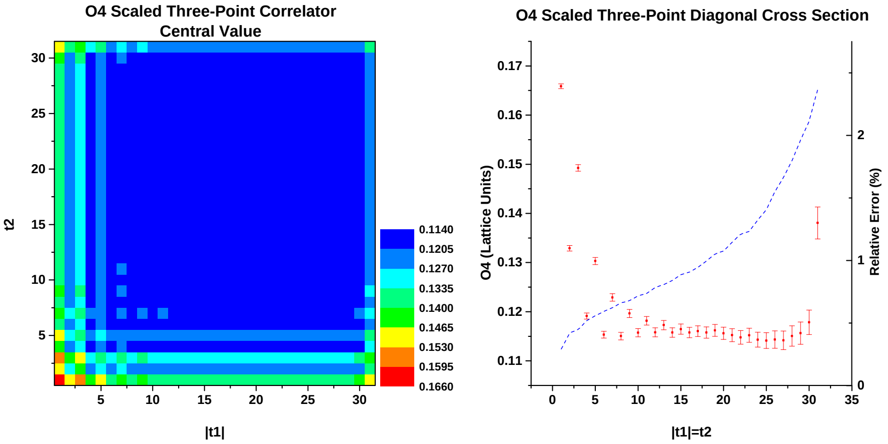

Figure 4.9: Scaled three-point for coarse 0.2ms ensemble with m_{val}=0.0500 with smeared source/sink and point source 4-quark operator.

4.4.2 Three-point fit region

In the spirit of not over-fitting the data, the fit ranges across the two- and three-point correlators are kept the same. However, since the three-point correlator is fit across a two dimensional plane unlike the two-points, there is some freedom in defining the three-point fit region while still being consistent. Fig. 4.10 show the relationship between the two correlator fits, as well as sensible definitions of t_{min} and t_{max} for the three-point correlation function.

Triangle fits

In an attempt to best resolve the matrix element, fits over the most amount of data was initially attempted. Due to folding, the upper and lower triangular region are completely correlated, therefore, the maximum dataset is sketched by the triangular region shown in Fig. 4.10. Fig. 4.11 shows a simultaneous two- and three-point correlator t_{min} stability plot on the $\mathcal{O}_4$ matrix element. Similar to the two-point, fits closer to the origin exhibit excited state contamination, while fits further from the origin yield growing errors as shown by the relative error line.

The t_{max} stability plot is shown in Fig. 4.12. The fits are expected to be insensitive to the choice of t_{max} as discussed in section 4.3.4 when analyzing the two-point correlation function. It is a surprise therefore, that a systematic trend is seen in the t_{max} stability plot. Aside from coding errors (which have been extensively checked and cross-checked), the contribution to this trend may come from either, unaccounted corrections to the three-point correlation function (physics problem), or fitting procedure (statistical problem).

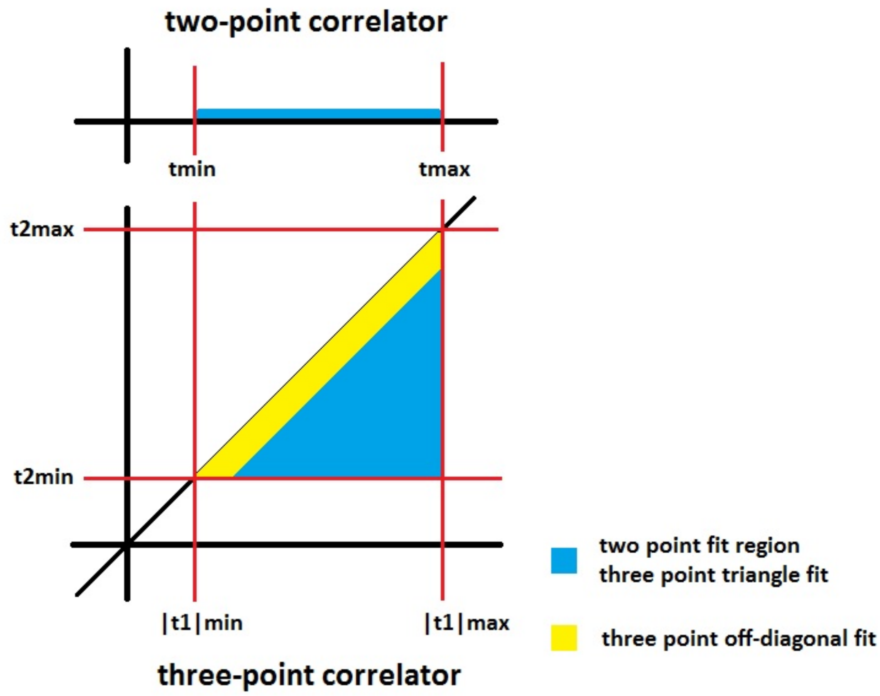

Figure 4.10: Two-point and three-point fit regions. The t_{min} and t_{max} of both fits are consistent, however because the three-point varies both the source and sink freely, there is more than one sensible fit region.

Three-point corrections

The systematic trend shown in Fig. 4.12 suggests that one possibility might be contamination from the backward propagating signal. In theory, this is suppressed by order e^{-ET} as derived in Appendix D, Eq. (D.20,D.21). The systematic trend however, warrants closer investigation of this effect. Fig. 4.13 compares the fit shown in Fig. 4.11 against a fit which includes the ground state periodic boundary condition terms and little difference is seen. In fact, adding the periodic boundary terms introduces less stability to the fits as seen by fits at $t_{\text{max}} = 19$ and 28 suggesting that the data has minimal information on the behavior of the new terms. Specifically, the coefficients of the periodic boundary terms fit towards values on the order of $1E-15$, while the $\tilde{Z}_n$s are of order one, suggesting that they are subdominant as expected.

Uncorrelated fits

Another possibility for the cause of the systematic effect seen in Fig. 4.11 is from statistical effects. The first indications of systematic statistical effects was observed while performing uncorrelated fits. Fig. 4.14 compares the uncorrelated

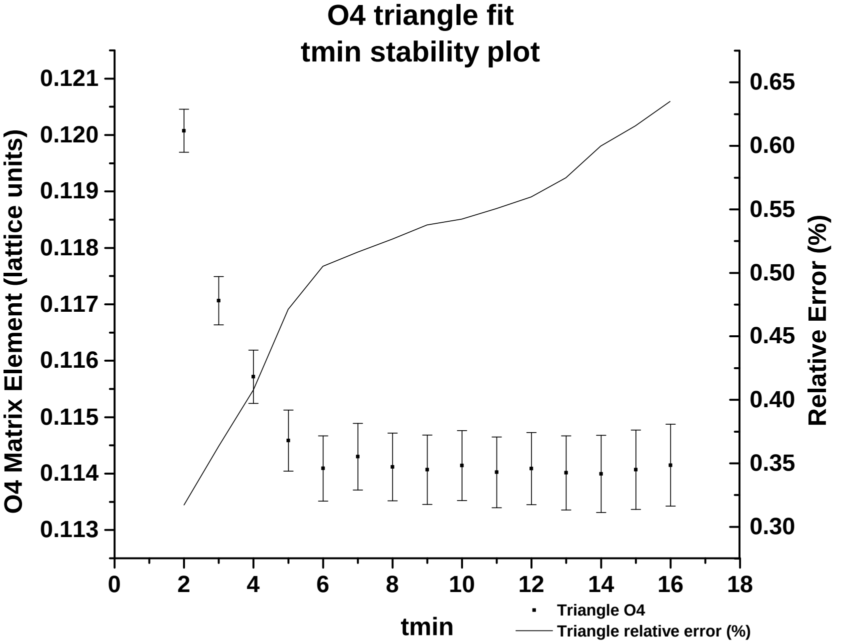

Figure 4.11: $\mathcal{O}_4$ triangle fit tmin stability plot with $t_{\max} = 25$. Two- and three-point simultaneous fits on the coarse 0.2ms ensemble with m_{val}=0.0500 with smeared source/sink and point source 4-quark operator. The two-point time range is fixed at [6,25].

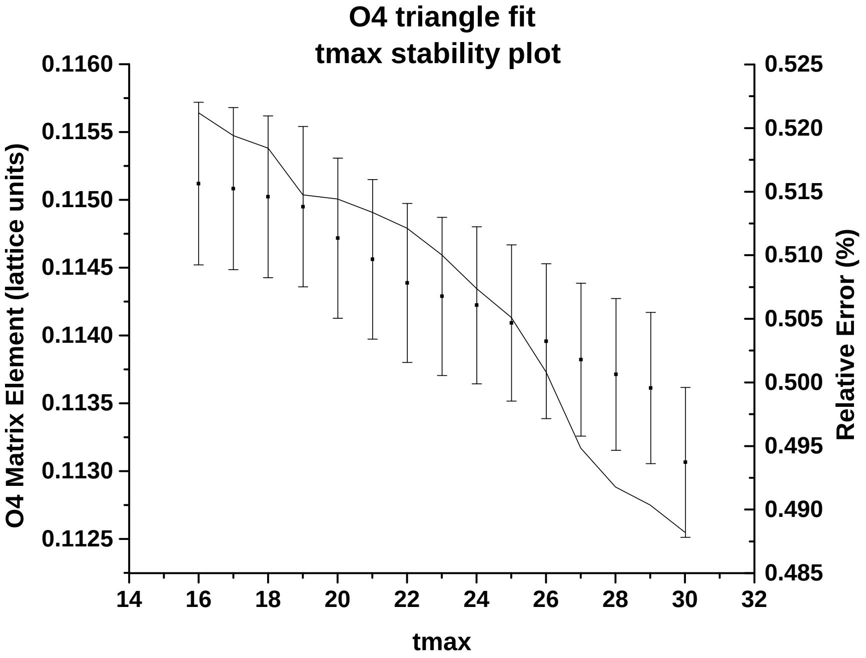

Figure 4.12: Study of the $t_{\max}$ stability plot for the coarse 0.2ms m0.0500 ensemble with $t_{\min} = 6$.

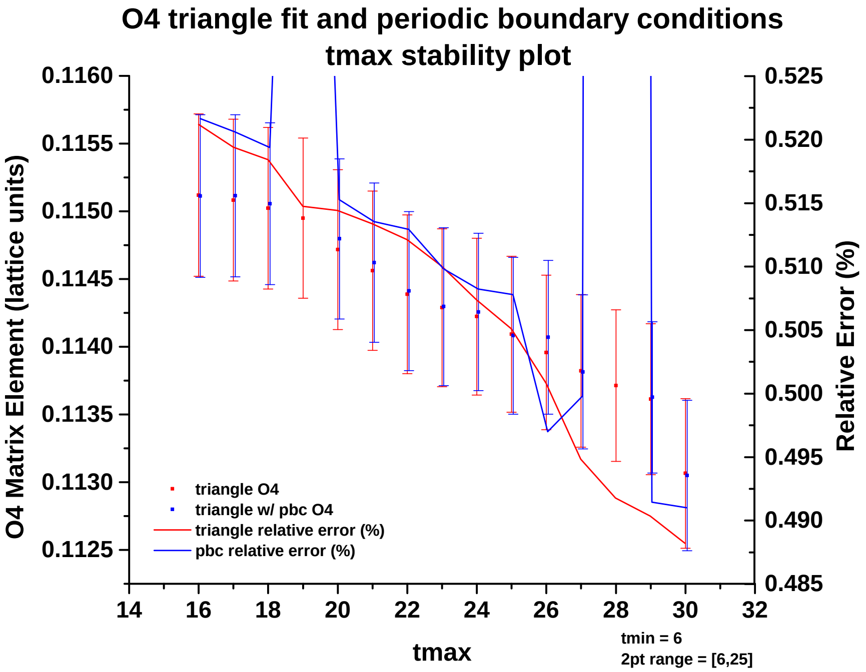

Figure 4.13: Comparison of three point fits with and without periodic boundary condition terms with a triangle fit region. Simultaneous fits with the two-point correlator on the coarse 0.2ms ensemble with $\mathrm{m_{val}}$=0.0500.

fit with the same correlated fit shown in Fig. 4.12. While there are strong correlations within an ensemble, and therefore uncorrelated fits are not suitable for the final analysis, Fig. 4.14 suggests that the systematic effects disappear through controlling the size of the covariance matrix.

Singular value decomposition

To further pursuit the idea of controlling the covariance matrix, fits were performed a triangular fit region with increasingly aggressive singular value decomposition (svd) cuts. In the application of least square fitting, the inverse of the covariance matrix is needed when minimizing the χ^2 statistic. Due to the finite accuracy available for numerical calculations, if the the eigenvalues of the covariance matrix span over many orders of magnitude, the matrix inversion becomes ill-conditioned and may lead to unexpected systematic effects. A traditional way to circumvent this issue is to impose a svdcut which sets a lower bound on the range of eigenvalues. The svdcut preserves the most important correlations in the data while approximating the original data using fewer dimensions leading to better controlled matrix inversions. Fig. 4.15 suggests that the systematic trend seen in Fig. 4.12 is slowly alleviated as stronger svdcuts are imposed. In particular, as we go from the black to the red and to the green points, allowing the eigenvalues of the covariance matrix to only span across four orders of

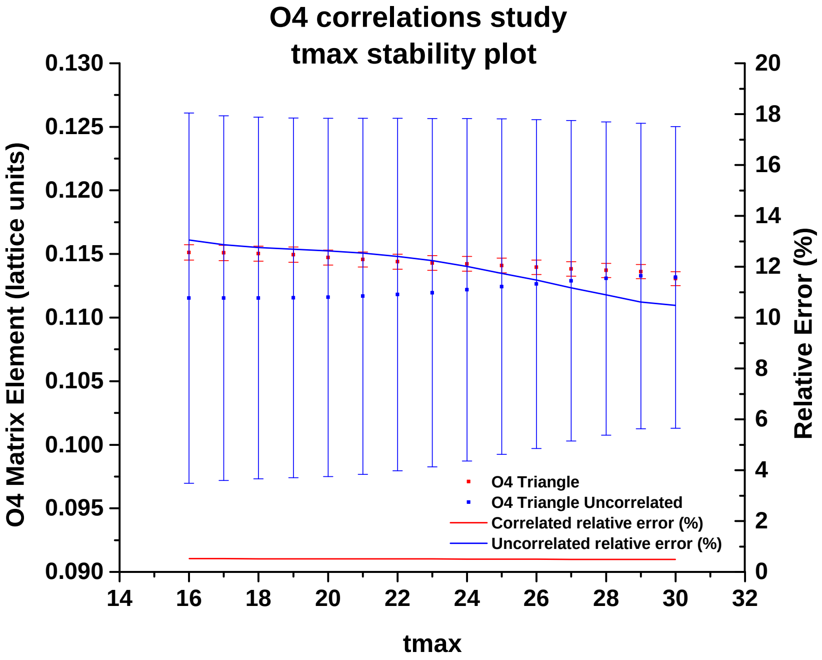

Figure 4.14: Comparison of three-point fits with and without correlations in the covariance matrix. Simultaneous fits with the two-point correlator on coarse 0.2ms ensembles with $\mathrm{m}_{\mathrm{val}} = 0.0500$.

magnitude significantly dampens the systematic trend. While well motivated from the point of view of computer algorithms and statistics, there is no physics reason to impose the svdcut at any particular value. Therefore while this study suggests that the systematic trends are a result of insufficient resolution in the data, the final analysis does not have any svdcuts, instead another method had to be implemented.

Random sampling

To further understand the t_{max} stability plots, a method is devised to understand the dependence of the matrix element as a function of the number of data points while being independent of the fit region. Varying the number of data points will test for stability under changes in the dimension of the covariance matrix, while keeping the fit region unchanged will fix the contribution (if there is any contribution) of signal from the boundary conditions. The fit region is fixed to the triangular fit region shown in Fig. 4.16. Within the triangle, $2 \leq m \leq N-2$ number of random data points are drawn G times where N is the total number of data points in the triangle. The results from the G number of subsamples drawn are averaged in the end to represent a typical m-data fit.

The study is performed on the coarse 0.2ms ensemble with $\mathrm{m}_{\mathrm{val}}$=0.0500 on operator $\mathcal{O}_4$. With the fit region indicated in Fig. 4.16, there are a total of

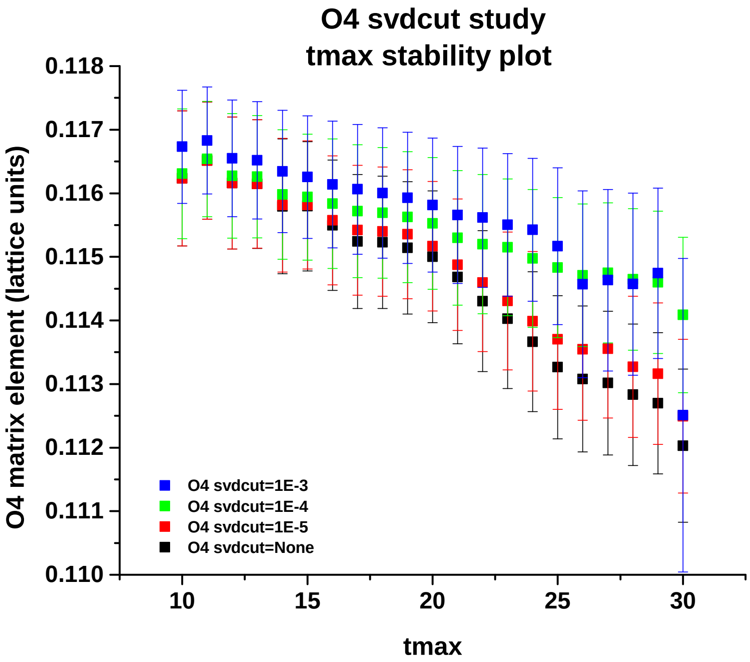

Figure 4.15: Svdcut study for $\mathcal{O}_4$ coarse 0.2ms ensemble with $\mathrm{m_{val}}$=0.0500.

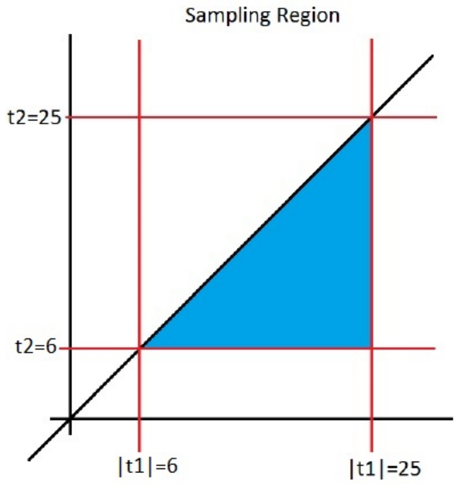

Figure 4.16: Fit region for random sampling on a coarse ensemble. The data is symmetric across $|t_1| = t_2$ and therefore only the triangular region is sampled.

$N = 210$ data points. Applying the constraint that $2 \leq m \leq N-2$, there are at least $\binom{N}{2} > 10^4$ unique sample sets. In the following analysis with $G = 200 \ll \binom{N}{m}$, the dataset may be safely sampled without duplication. The results of random sampling are shown in Fig. 4.17. For $m < 60$ Fig. 4.17 shows that the fits that are stable, but with relatively larger errors due to fitting through a sparse number of points. In the middle, there is a region between $60 < m < 100$ where the fits are stable both in the central value and error. The intermediate region seen here is a lucky balance between fitting over too little data leading to larger error and fitting over too much data, leading to ill-conditioned covariance matrix inversions. The systematic effects of ill-conditioned inversions are seen for $m > 100$ where a downward trend similar to Fig. 4.12 is seen. Overlaid on top of Fig. 4.16 are three more conventional fit strategies over the same time range $t_{\text{min}} = 6$ and $t_{\text{max}} = 25$. The red point corresponds to the triangle fit and is the limiting case of a $m = N$ random fit. In order to avoid the region of large systematic uncertainty, two other fit shapes were considered; the blue corresponds to a fit along the $|t_1| = t_2$ diagonal slice, while the bidiagonal fit in green indicates a fit to the diagonal plus one off-diagonal entry of data. The two diagonal type fits statistically agree with the random fit results. The bidiagonal fits return significantly better error bars as well due to the fact that the off-diagonal data elements include information on the $J^P = 0^+$ state information, which for the lattice data, is the first state with larger energy than the ground state. Therefore, the bidiagonal fits both thin down the number of data points, which improves the stability of the matrix inversion, as well as preserves the most important correlations in the data.

Bidiagonal fits

The bidiagonal fits possess the attribute keeping the most important correlations in the dataset from a physics standpoint by including information on the $J^P = 0^+$ state, as well as minimizes the range in eigenvalues of the covariance matrix. The bidiagonal fit shape is used in the final analysis; representative stability plots of these fits are supplied in this section. Fig. 4.18 is the t_{min} stability plot; a region of stability with relatively small errors is observed across time regions $[3, 6]$. Data towards earlier time slices have better signal to noise ratio and therefore yields smaller errors in the fits. Fits towards larger time slices are statistically stable and consistent; however statistical noise undermines the precision of the results. Fig. 4.19 shows the t_{max} stability plot; the bidiagonal fits show a wide region of stability as expected since at high time slices, the ground state signal is dominant, therefore fits are expected to be insensitive to changes in t_{max}. The priors and time ranges of the bidiagonal fits are listed in Appendix F.5.

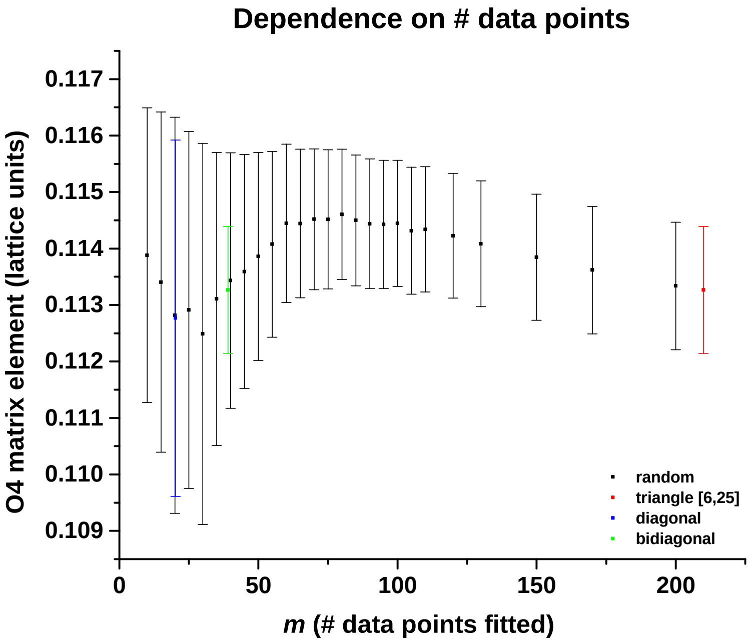

Figure 4.17: Random sampling on O4 coarse 0.2ms ensemble with m_{val}=0.0500. Overlayed are the diagonal, bidiagonal and triangle fits plotted against the corresponding number of data points each fit shape has.

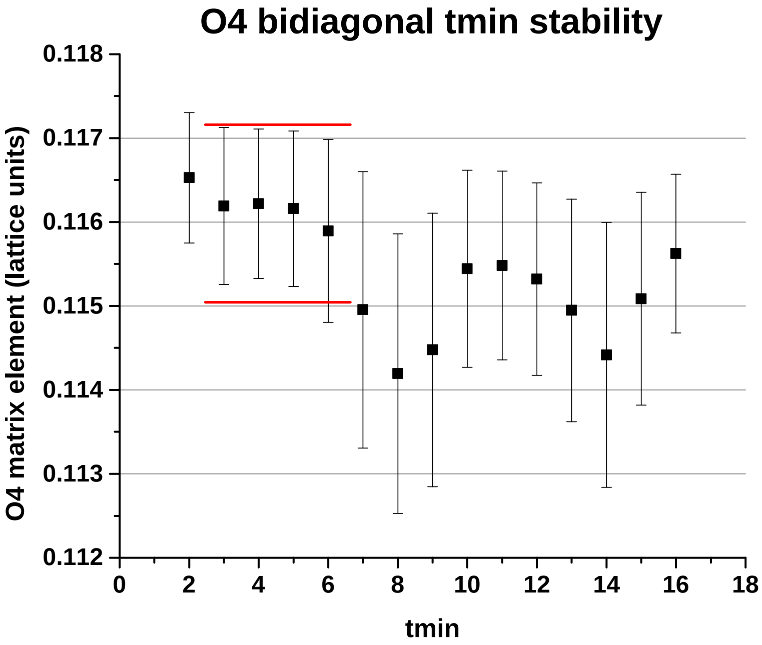

Figure 4.18: Bidiagonal fit on $\mathcal{O}_4$ coarse 0.2ms m0.0500 ensemble with $t_{\max} = 25$. The red lines suggest a region of stability.

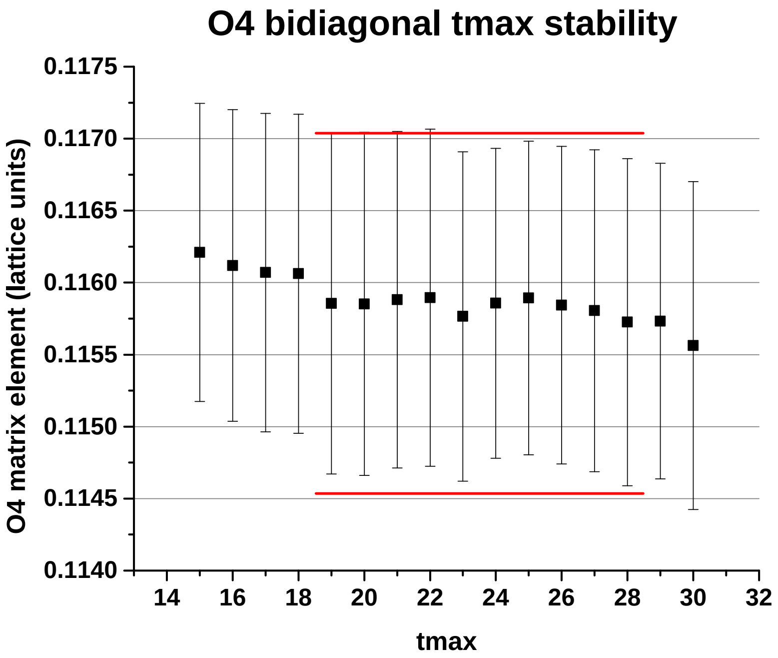

Figure 4.19: Bidiagonal fit on $\mathcal{O}_4$ coarse 0.2ms m0.0500 ensemble with $t_{\min} = 6$. The red lines suggest a region of stability.

Chapter 5

Renormalization and Matching

Calculations performed on the lattice are automatically UV regulated by the finite lattice spacing. The matrix elements evaluated at different lattice spacing are therefore regulated at different scales. The combination of the Wilson coefficients and matrix elements however, are independent of scheme and scale. In order to combine the results of the matrix elements with the Wilson coefficients, matrix elements at different lattice spacing need to be evaluated at the same scale and matched to the same continuum scheme. For this project, we match lattice regularization to dimensional regularization with the $\overline{\mathrm{MS}}$-scheme at the charm quark scale. To one-loop in perturbation theory, the matrix elements $\{\langle\mathcal{O}_1\rangle, \langle\mathcal{O}_2\rangle, \langle\mathcal{O}_3\rangle\}$ and $\{\langle\mathcal{O}_4\rangle, \langle\mathcal{O}_5\rangle\}$ mix within the separate subsets. Explicitly, the one-loop renormalized matrix elements are given as,

$$\left\langle D\left|\mathcal{O}_1\right|\bar{D}\right\rangle_{\text{renorm}} = [1+\alpha_V\zeta_{11}]\left\langle D\left|\mathcal{O}_1\right|\bar{D}\right\rangle_{\text{lat}} + \alpha_V\zeta_{12}\left\langle D\left|\mathcal{O}_2\right|\bar{D}\right\rangle_{\text{lat}}, \tag{5.1}$$

$$\left\langle D\left|\mathcal{O}_2\right|\bar{D}\right\rangle_{\text{renorm}} = [1+\alpha_V\zeta_{22}]\left\langle D\left|\mathcal{O}_2\right|\bar{D}\right\rangle_{\text{lat}} + \alpha_V\zeta_{21}\left\langle D\left|\mathcal{O}_1\right|\bar{D}\right\rangle_{\text{lat}}, \tag{5.2}$$

$$\left\langle D\left|\mathcal{O}_3\right|\bar{D}\right\rangle_{\text{renorm}} = [1+\alpha_V\zeta_{33}]\left\langle D\left|\mathcal{O}_3\right|\bar{D}\right\rangle_{\text{lat}} + \alpha_V\zeta_{31}\left\langle D\left|\mathcal{O}_1\right|\bar{D}\right\rangle_{\text{lat}}, \tag{5.3}$$

$$\left\langle D\left|\mathcal{O}_4\right|\bar{D}\right\rangle_{\text{renorm}} = [1+\alpha_V\zeta_{44}]\left\langle D\left|\mathcal{O}_4\right|\bar{D}\right\rangle_{\text{lat}} + \alpha_V\zeta_{45}\left\langle D\left|\mathcal{O}_5\right|\bar{D}\right\rangle_{\text{lat}}, \tag{5.4}$$

$$\left\langle D\left|\mathcal{O}_5\right|\bar{D}\right\rangle_{\text{renorm}} = [1+\alpha_V\zeta_{55}]\left\langle D\left|\mathcal{O}_5\right|\bar{D}\right\rangle_{\text{lat}} + \alpha_V\zeta_{54}\left\langle D\left|\mathcal{O}_4\right|\bar{D}\right\rangle_{\text{lat}}. \tag{5.5}$$

The expansion is performed around the renormalized coupling α_V instead of the bare coupling $\alpha_s \equiv g_{\text{lat}}^2/4\pi$. This is motivated by the fact that the lattice bare coupling is a poor expansion parameter due to large renormalizations stemming from tadpole contributions [46]. In order to remove the bulk of these contributions, we we use the "V-scheme" for defining α_V, which is determined by the static quark potential

$$V(q) = \frac{4}{3}\frac{4\pi\alpha_V(q)}{q^2}. \tag{5.6}$$

The static quark potential is simulated on the lattice in order to extract $\alpha_V(q)$. The running of α_V is given by Ref. [50]

$$q^2\frac{d\alpha_V(q)}{dq^2} = -\beta_0\alpha_V^2(\mu) - \beta_1\alpha_V^3(\mu) - \beta_2\alpha_V^4(\mu) - \beta_3\alpha_V^5(\mu) + \mathcal{O}\left(\alpha_V^6(\mu)\right) \tag{5.7}$$

where the constants β_i are given by Ref. [62]. The scale μ is fixed to the typical scale of the loop momenta $2/a$ where a is the lattice spacing. Eq. (5.7) is then numerically integrated in order to obtain α_V evaluated at 3 GeV.

The one-loop renormalization coefficients ζ are evaluated using dimensional regularization in the $\overline{\text{MS}}$ scheme. In non-integer dimensions, the Dirac algebra is infinite dimensional and requires in an infinite set of evanescent operators in addition to the familiar 4-dimensional basis of operators in order to define the algebra. The choice of evanescent operators are not unique, and for this project we follow the BBGLN [12] definition. The renormalization coefficients for all five operators are listed in Appendix F.6.

Chapter 6

Kappa tuning corrections

The heavy-quark mass is an input parameter κ to the simulation and is chosen to be close to the physical value. However, the physical value of the charm quark is verified by evaluating the chiral-continuum extrapolated D_s mass. Therefore, in the initial phase of data generation, it is impossible to choose the value of κ which yields exactly the correct D_s mass. We correct the mistunings in the heavy quark mass and match the lattice dispersion relation to the continuum up to order $\mathbf{p}^2$. The dispersion relation is described in [35] as

$$E^2(\mathbf{p}) = M_1^2 + \frac{M_1}{M_2}\mathbf{p}^2 + \mathcal{O}(\mathbf{p}^4) \tag{6.1}$$

where the rest mass

$$M_1 = E(\mathbf{0}), \tag{6.2}$$

and the kinetic mass

$$M_2^{-1} = (\partial^2 E/\partial p_i^2)_{\mathbf{p}=\mathbf{0}} \tag{6.3}$$

of the heavy quark. Weak matrix elements are unaffected by the rest mass M_1. As long as M_1 is large, corrections to heavy quark systematic errors expand around the heavy-quark limit, which is sensitive to the kinetic mass M_2. Therefore it is important to tune the kinetic mass to the physical D-meson mass. For this project, another set of correlation functions at a different κ value is generated in order to extrapolate the matrix elements to the correct heavy quark mass. Our method of tuning the κ value for the charm quark closely follows the prescription outlined in Refs. [8, 17].

The kappa tuning shifts are implemented by linearly extrapolating the matrix elements using the following formula,

$$\langle \mathcal{O}_i \rangle_{\text{tune}} = \langle \mathcal{O}_i \rangle_{\text{sim.}} + \sigma_i \times \Delta M_2 \tag{6.4}$$

where

$$\sigma_i = \frac{d\left\langle r_1^3 \mathcal{O}_i \right\rangle_{\text{sim.}}}{d\left(\frac{1}{r_1 M_2}\right)} \tag{6.5}$$

and

$$\Delta M_2 = \left(\frac{1}{r_1 M_2}\right)_{\text{tune}} - \left(\frac{1}{r_1 M_2}\right)_{\text{sim.}}. \tag{6.6}$$

The kinetic mass is related to the κ values as outlined in [17]

$$\frac{1}{aM_2} = \frac{2}{am_0(2+am_0)} + \frac{1}{1+am_0} \tag{6.7}$$

where am_0 is the tadpole-improved bare quark mass given by

$$am_0 = \frac{1}{2u_0}\left(\frac{1}{\kappa} - \frac{1}{\kappa_{\text{crit}}}\right) \tag{6.8}$$

where a is the lattice spacing, u_0 is the tadpole-improvement factor [46], and κ_{crit} corresponds to the value of κ in which the mass of the pseudoscalar meson vanishes. The values of the critical, tuned and simulated κ values, u_0 and r_1/a are given in section F.7. Using Eq. (6.6), the corresponding values for ΔM_2 are given in Table F.14.

The slope described by Eq. (6.5) is extracted with a correlated unconstrained linear fit on the renormalized 0.12fm, $m_l/m_s = 0.2$ ensemble at valence masses of $am_q = 0.0100$ and 0.349, at κ values of 0.1254 and 0.1280. The one-loop renormalization coefficients used for the kappa tuning points are given in Appendix F.6. The prescription for the three-point fits follow closely with what is described in section 4, with the exception of the widening the prior on $E_0 = 1.0(1) \to 1.0(2)$ in order to account for the difference in the ground state energy due to varying κ. To extract the slope for each valence mass,

$$\left\{\langle\mathcal{O}_i\rangle^{\text{boot0}}_{\kappa=0.1254}, \langle\mathcal{O}_i\rangle^{\text{boot0}}_{\kappa=0.1280}\right\}_{am_q} \to \left\{0, \langle\mathcal{O}_i\rangle^{\text{boot0}}_{\kappa=0.1280} - \langle\mathcal{O}_i\rangle^{\text{boot0}}_{\kappa=0.1254}\right\}_{am_q}, \tag{6.9}$$

$$\left\{\frac{1}{aM_2}_{\kappa=0.1254}, \frac{1}{aM_2}_{\kappa=0.1280}\right\}_{am_q} \to \left\{0, \frac{1}{aM_2}_{\kappa=0.1280} - \frac{1}{aM_2}_{\kappa=0.1254}\right\}_{am_q}, \tag{6.10}$$

shifting the matrix elements such that the y-intercept is at zero by construction. With this formulation, a two-parameter fit defined as

$$\sigma_i \times 1/r_1M_2 + \text{intercept} \tag{6.11}$$

is implemented in order to extract the slope across two valence masses. The intercept, while possessing a central value of zero, is introduced as a fit parameter in order to avoid over-constraining the fit. Neglecting to include the intercept is equivalent to setting a prior of zero width. Figure 6.1 shows the result of the two-parameter linear fit on all five matrix elements. Table F.15 includes the list of slopes.

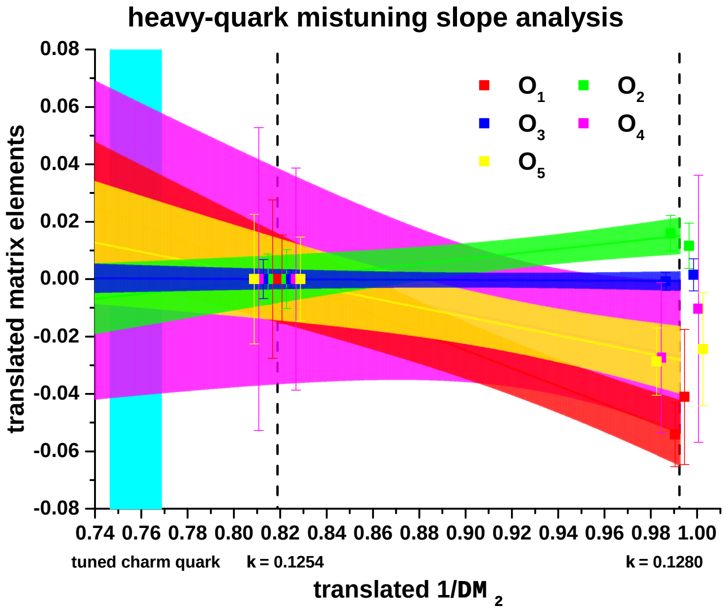

Figure 6.1: Linear fit to all five matrix elements. The slope is extracted from a correlated, unconstrained fit.

Chapter 7

Extrapolation to the physical point

7.1 One-loop corrections to D-meson mixing

The extrapolation to the physical pion mass and continuum limit is guided by NLO SU(3) heavy-meson partially-quenched rooted-staggered chiral perturbation theory. The effective theory treats pions as the fundamental degrees of freedom, and in SU(3), this includes the kaons. Heavy meson chiral perturbation theory allows for the inclusion of heavy quarks through the language of heavy quark effective theory (HQET). Since the light quarks are described by staggered quarks with the fourth-root trick applied to the fermionic determinant, the chiral perturbation theory takes into account the interactions of pions with different taste structures. A more in-depth overview of the details of the effective theory is given in the appendix.

From the chiral effective theory, the Feynman rules are derived, and the scattering matrix in terms of pion degrees of freedom for neutral-meson mixing is worked out [15]. To one-loop in chiral perturbation theory, the matrix elements receives corrections from the wavefunction renormalization $\mathcal{W}$, tadpole $\mathcal{T}$, and sunset $\mathcal{Q}$ terms shown in Fig. 7.1. Due to the fact that the valence quarks are naive quarks, which are constructed from the staggered quarks via the similarity transformation. There are also wrong-spin, taste-mixing terms which enter the tadpole and sunset diagrams parametrized by $\tilde{\mathcal{T}}$ and $\tilde{\mathcal{Q}}$ respectively. The matrix element described by up to one-loop in chiral perturbation theory where

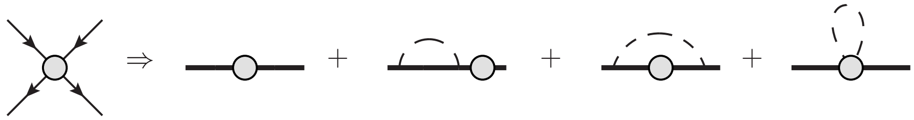

Figure 7.1: The matrix element expanded to one-loop in chiral perturbation theory. The thick solid lines represent the D^0 meson while the dashed lines represent the pion. At one-loop, the diagrams are respectively the wavefunction renormalization, the sunset and the tadpole contribution. On the left-hand side of the equation we have a description with quark degrees of freedom, and on the right hand-side we have a description in meson degrees of freedom.

I schematically illustrate as,

$$\left\langle \bar{D}^0 \left| \mathcal{O}_i \right| D^0 \right\rangle = \beta_i \left(1 + \mathcal{W} + \mathcal{T}^{(i)} + \tilde{\mathcal{T}}^{(i)} + \text{analytic terms} \right) \tag{7.1}$$

$$+ \beta_i' \left(\mathcal{Q}^{(i)} + \tilde{\mathcal{Q}}^{(i)} \right), \tag{7.2}$$

for $i = \{1,2,3,4,5\}$ where $\beta_1' = \beta_1$. The βs are the leading order LECs and is the parameter of interest that is extrapolated to the physical point, therefore loose priors are used in order to prevent over-constraining the parameter. The exact forms of the one-loop contributions are derived in Ref. [15] and are reproduced below.

The wavefunction renormalization is given to be,

$$\begin{aligned}\mathcal{W} = & \frac{i g^2_{D^* D\pi}}{f_\pi^2} \left\{ \frac{1}{16} \sum_{\mathcal{S},\rho} N_\rho \mathcal{H}^{\Delta^* + \delta_{\mathcal{S}x}}_{x\mathcal{S},\rho} + \frac{1}{3} \left[R^{[2,2]}_{X_I}(\{M^{(2)}_{X_I}\};\{B_{0I}\}) \frac{\partial \mathcal{H}^{\Delta^*}_{X,I}}{\partial m^2_{X_I}} \right. \right. \\ & - \sum_{j \in \{M_I^{(2)}\}} D^{[2,2]}_{j;X_I}(\{M^{(2)}_{X_I}\};\{B_{0I}\}) \mathcal{H}^{\Delta^*}_{j,I} \Bigg] + a^2 \delta_V' \left[R^{[3,2]}_{X_V}(\{M^{(3)}_{X_V}\};\{B_{0V}\}) \frac{\partial \mathcal{H}^{\Delta^*}_{X,V}}{\partial m^2_{X_V}} \right. \\ & \left. \left. - \sum_{j \in \{M_V^{(3)}\}} D^{[3,2]}_{j,X_V}(\{M^{(3)}_{X_V}\};\{B_{0V}\}) \mathcal{H}^{\Delta^*}_{j,V} \right] + (V \to A) \right\}. \end{aligned} \tag{7.3}$$

The constant f_π is free parameter of the chiral effective theory, and is a parameter that needs to be set in order for the effective theory to gain predictive power. Therefore the experimental result of $f_\pi = 130\text{MeV} \pm 0.20\text{MeV}$ [55] is introduced as a prior to set the central value and encapsulate the experimental uncertainty into the analysis.

In the infinite-mass limit of the heavy quark, the D and D^* forms a doublet due to heavy-quark spin symmetry and couples with strength $g_{D^* D\pi}$ to the pion. The $g_{D^* D\pi}$ has been studied extensively for two dynamical light sea quarks in [11] yielding $g_{D^* D\pi} = 0.53(3)(3)$ and 2+1 dynamical sea quarks in [23] yielding 0.55(6). We take the conservative value of $g_{D^* D\pi} = 0.53 \pm 0.08$ for this coupling.

The sum runs over ρ taste representations (P,A,T,V,I) with degeneracies $\mathcal{N}_\rho \in \{1,4,6,4,1\}$ and sea quarks $\mathcal{S} \in \{u,d,s\}$. The taste contributions form degeneracies as a result of SO(4) taste symmetry being protected at $\mathcal{O}(a^2)$ in the chiral Lagrangian and is discussed in detail in Appendix C.2.2. $\mathcal{H}$ refers to the chiral logarithm involving a heavy quark inside the loop. Referring to the wavefunction renormalization contribution in Fig. 7.1, $\mathcal{H}^{\Delta^* + \delta_{\mathcal{S},x}}_{x\mathcal{S},\rho}$ describes a loop integral involving a pion (dashed line) constructed by a $\mathcal{S}$ sea quark and x valence quark over all taste representations $\mathcal{N}_\rho$ and a D^* meson (bold solid line inside the loop) involving $\mathcal{S}$ in its light quark component.

Corrections to the breaking of heavy-quark spin symmetry is parametrized by the hyperfine splitting $\Delta^* = M_{D^*} - M_D \approx 142.1 \pm 2.6\text{MeV}$ consistent with ref. [8] and is set by the experimental measurements for the splitting. Flavor SU(3) symmetry breaking is parametrized by the splitting

$$\delta_{\mathcal{S}x} \equiv M_{D_{\mathcal{S}}} - M_{D_x} = 2\lambda_1 B_0(m_{\mathcal{S}} - m_x) = \lambda_1(M_{\eta_s}^2 - M_{\pi^0}^2) \tag{7.4}$$

where we used the result $M_\pi^2 = 2B_0 m_l$ to relate the quark mass to the meson mass as derived in Eq. (C.38), where m_l is the degenerate up/down sea quark mass. From Eq. 7.4 we see that $\lambda_1 = M_{D_s} - M_{D_x}/M_{\eta_s}^2 - M_{\pi^0}^2$ parametrizes the ratio of the flavor splitting of the heavy-light and light-light mesons and serves as an expansion parameter. The pion and D-meson masses are determined by experimental measurements [13] while the η_s is a theoretical $\bar{s}s$ bound state with mass determined by ref [30]. Combining the results, we set $\lambda_1 = 0.219 \pm 0.003\text{GeV}^{-1}$. While the flavor splitting is formally of higher order in perturbation theory since these are corrections on top of the one-loop order, numerically λ_1 is large and therefore is added into the description.

The remaining chiral logarithms in Eq. (7.3) involve loop integrals $\mathcal{H}$ scaled by factors of the residue R and D. These terms come from geometrically summing up the one particle irreducible diagrams involving taste changing loops inside the propagator, analogous to the vacuum polarization correction to the photon propagator. The single and double poles arise a result of the sum over the geometric series and respectively yield residues R and D. The residue is a function of the chiral condensate $q\bar{q}$ yielding the set of meson states π^0, η, η'. For the scalar taste states I, the U(1) axial anomaly takes the η' mass to infinity and decouples the meson from the theory. However the vector and axial-vector tastes of the η' do not decouple. In fact, the coupling to the η' is given by the hairpin strength δ'_ρ [15] where

$$\delta'_\rho = \begin{cases} a^2\delta'_V & \rho = V \text{ (taste vector)} \\ a^2\delta'_A & \rho = A \text{ (taste axial-vector)} \\ 4m_0^2/3 & \rho = I \text{ (taste singlet)} \\ 0 & \rho = T, P \text{ (taste tensor and pseudoscalar)} \end{cases} . \tag{7.5}$$

The coefficient m_0 is a free parameter of the chiral Lagrangian related to the anomaly term and the limit $m_0 \to \infty$ is taken to recover physical meson states. While the tensor and pseudoscalar tastes do not interact at this order, the vector and axial-vector tastes enter in at order $a^2\delta'_V$ and $a^2\delta'_A$. Therefore, the loop-integrals for the singlet taste state only depend on

$$M_X^{(2)} \equiv \{m_\eta, m_X\} \tag{7.6}$$

while the vector and axial-vector tastes depend on also the η' and form the set of masses

$$M_X^{(3)} \equiv \{m_\eta, m_{\eta'}, m_X\} \tag{7.7}$$

where m_X is the mass of the light-light meson with $x\bar{x}$ quark content. Here again the x denotes a valence quark.

Within the loop integrals, a UV cutoff is introduced, and sets the scale for the chiral effective theory. The chiral scale Λ_χ defines the cutoff of the effective theory and is fixed as a constant so all couplings are evaluated at the same energy scale. It is customary to assert that chiral perturbation theory is valid up to the ρ-meson mass, where the rho-meson is the next lightest meson in the spectrum after accounting for the eight Goldstone bosons (pions, kaons and eta) of the chiral effective theory. Therefore $\Lambda_\chi = 775$MeV is fixed as a constant. Given a reasonable choice of the chiral scale, what is important is that the chiral scale is to the same value across all analysis such that all the couplings are evaluated at the same scale.

The following is the expression for the sunset contribution given in ref. [15] in Fig. 7.1 corresponding to the third term in the diagrammatic expansion.

$$\begin{aligned}\mathcal{Q}^{(i)} =& \frac{-ig^2_{D^*D\pi}}{f^2_\pi}\Bigg\{\frac{1}{16}\sum_\rho N_\rho \mathcal{H}^{\Delta^*}_{X,\rho} + \frac{1}{3}\Bigg[R^{[2,2]}_{X_I}(\{M^{(2)}_{X_I};\{B_{0I}\})\,\frac{\partial \mathcal{H}^{\Delta^*}_{X,I}}{\partial m^2_{X_R}} \\ &- \sum_{j\in\{M^{(2)}_I\}} D^{[2,2]}_{j,X_I}(\{M^{(2)}_{X_I}\};\{B_{0I}\})\mathcal{H}^{\Delta^*}_{j,I}\Bigg]\Bigg\}. \end{aligned} \tag{7.8}$$

The tadpole corrections described by the last term in fig. 7.1 is also worked in in ref. [15] and is reproduced below. For the $\mathcal{O}_N$ for $N \in \{1,2,3\}$ and $N \in \{4,5\}$, the tadpole contributions are respectively

$$\begin{aligned}\mathcal{T}^{(1,2,3)} =& \frac{-i}{f^2_\pi}\Bigg\{\frac{1}{16}\sum_{\mathcal{S},\rho} N_\rho \mathcal{I}_{x\mathcal{S},\rho} + \frac{1}{16}\sum_\rho N_\rho \mathcal{I}_{X,\rho} + \frac{2}{3}\Bigg[R^{[2,2]}_{X_I}(\{M^{(2)}_{X_I}\};\{B_{0I}\})\,\frac{\partial \mathcal{I}_{X,I}}{\partial m^2_{X_I}} \\ &- \sum_{j\in\{M^{(2)}_I\}} D^{[2,2]}_{j,X_I}(\{M^{(2)}_{X_I}\};\{B_{0I}\})\mathcal{I}_{j,I}\Bigg] + a^2\delta'_V\Bigg[R^{[3,2]}_{X_V}(\{M^{(3)}_{X_V}\};\{B_{0V}\})\,\frac{\partial \mathcal{I}_{X,V}}{\partial m^2_{X_V}} \\ &- \sum_{j\in\{M^{(2)}_V\}} D^{[3,2]}_{j,X_V}(\{M^{(3)}_{X_V}\};\{B_{0V}\})\mathcal{I}_{j,V}\Bigg] + (V\to A)\Bigg\}, \end{aligned} \tag{7.9}$$

$$\begin{aligned}\mathcal{T}^{(4,5)} =& \frac{-i}{f^2_\pi}\Bigg\{\frac{1}{16}\sum_{\mathcal{S},\rho} N_\rho \mathcal{I}_{x\mathcal{S},\rho} - \frac{1}{16}\sum_\rho N_\rho \mathcal{I}_{X,\rho} + a^2\delta'_V\Bigg[R^{[3,2]}_{X_V}(\{M^{(3)}_{X_V}\};\{B_{0V}\})\,\frac{\partial \mathcal{I}_{X,V}}{\partial m^2_{X_V}} \\ &- \sum_{j\in\{M^{(2)}_V\}} D^{[3,2]}_{j,X_V}(\{M^{(3)}_{X_V}\};\{B_{0V}\})\mathcal{I}_{j,V}\Bigg] + (V\to A)\Bigg\}. \end{aligned} \tag{7.10}$$

The loop integrals in the tadpole diagrams involve only a light-light meson unlike the wavefunction and sunset contributions, therefore the chiral logarithms are parametrized by $\mathcal{I}$ denoting loops with only light-light mesons involved.

We define the chiral fit function involving the leading order β_i and NLO chiral logs as

$$F_i^{\text{logs.}} = \beta_i \left(1 + \mathcal{W} + \mathcal{T}^{(i)} + \tilde{\mathcal{T}}^{(i)}\right) + \beta_i' \left(\mathcal{Q}^{(i)} + \tilde{\mathcal{Q}}^{(i)}\right) \tag{7.11}$$

where $\beta_1 = \beta_1'$.

Next-to-leading order analytic terms are added to the chiral fit function in order to capture 1) explicit chiral symmetry breaking from the QCD Lagrangian of order m_q and 2) light-quark discretization errors stemming from the asqtad action of order $\alpha_s^2 a^2$. It is also possible to include a generic order $\alpha_s a^2$ analytic term to capture one-loop corrections, however we observe stability in our fits even while omitting this term. The analytic terms are expressed in dimensionless parameters [8] x_q, x_l, and x_h corresponding to the light-valence, light-sea and strange-sea quark masses $m_{q,l,h}$ respectively. The order $\alpha_s^2 a^2$ term is parametrized by the average taste-splitting $a^2\bar{\Delta}$. We know that the average taste splitting must be proportional to $\alpha_s^2 a^2$ because the asqtad action, which has discretization errors starting at that order which correspond to SO(4) taste breaking effects characterized by the average taste splitting. The dimensionless parameters are explicitly,

$$\begin{aligned} x_{q,l,h} \equiv& \frac{(r_1 B_0)(r_1/a)(2am_{q,l,h})}{8\pi^2 f_\pi^2 r_1^2}, && (7.12)\\ x_{\bar{\Delta}} \equiv& \frac{r_1^2 a^2 \bar{\Delta}}{8\pi^2 f_\pi^2 r_a^2}, && (7.13)\\ \text{where } \bar{\Delta} =& \frac{1}{16}(\Delta_P + 4\Delta_A + 6\Delta_T + 4\Delta_V + \Delta_I). && (7.14)\end{aligned}$$

As simulation parameters, the xs are conveniently defined in r_1 units as explained in Appendix F.1. In terms of these parameters, the NLO analytic terms used in this analysis are,

$$F_i^{\text{NLO}} = c_{0,i}x_q + c_{1,i}(2x_l + x_h) + c_{2,i}x_{\bar{\Delta}}\ . \tag{7.15}$$

The NNLO analytic terms are introduced to saturate the errors arising from the NNLO chiral logarithms and analytic contributions, playing a similar role as higher energy terms are for correlator fits. The NNLO analytic terms are the set of quadratic mass and taste splitting contributions,

$$\begin{aligned} F_i^{\text{NNLO}} =& d_{0,i}x_q x_{\bar{\Delta}} + d_{1,i}(2x_l + x_h)x_{\bar{\Delta}} + d_{2,i}(2x_l + x_h)x_q \\ &+ d_{3,i}x_q^2 + d_{4,i}(2x_l + x_h)^2 + d_{5,i}x_{\bar{\Delta}}^2 + d_{6,i}(2x_l^2 + x_h^2). \qquad (7.16)\end{aligned}$$

The LECs in the NLO analytic terms are discernible by data and are therefore loosely constrained by prior of 0 ± 10 given that we expect these LECs to be of $\mathcal{O}(1)$. The NNLO analytic LECs are constrained to 0 ± 1 to account for our expectation of the size of the coefficients while using natural chipt units. We can extend this to include NNNLO analytic terms as an option to check for error saturation.

$$\begin{aligned}F_i^{\mathrm{NNNLO}} =& e_{0,i}x_q^2 x_{\bar{\Delta}} + e_{1,i}x_q(2x_l + x_h)x_{\bar{\Delta}} + e_{2,i}x_q x_{\bar{\Delta}}^2 \\ & + e_{6,i}(2x_l + x_h)^2 x_{\bar{\Delta}} + e_{7,i}(2x_l + x_h)x_{\bar{\Delta}}^2 + e_{10,i}x_{\bar{\Delta}}^3 + e_{11,i}(2x_l^2 + x_h^2)x_{\bar{\Delta}} \\ & + e_{3,i}x_q^2(2x_l + x_h) + e_{4,i}x_q^3 + e_{5,i}x_q(2x_l + x_h)^2 + e_{13,i}x_q(2x_l^2 + x_h^2) \\ & + e_{8,i}(2x_l^3 + x_h^3) + e_{9,i}(2x_l + x_h)(2x_l^2 + x_h^2) + e_{12,i}(2x_l^3 + x_h^3),\end{aligned} \tag{7.17}$$

where the coefficients $e_{j,i}$ are constrained to the natural order of 0 ± 1.

Finally, we reserve the option to include generic $\alpha_s a^2$ discretization errors through the term

$$F_i^{\alpha_s a^2} = g_{0,i}\alpha_s \left(\frac{a}{r_1}\right)^2, \tag{7.18}$$

where the coefficient $g_{0,i}$ is given a prior of 0 ± 1.

7.1.1 Wrong-spin taste mixing contributions

In the formulation of the staggered action as described in Appendix B.2, the naive quark field may be expressed as four copies of the staggered field

$$q(x) = \Omega_x \chi(x)_A. \tag{7.19}$$

The four copies of the staggered field are invariant under SU(4) transformations and form a copy symmetry that is exact on the lattice. This may be seen by following the derivation of the staggered action and noting that the Kawamoto-Smit transformation exactly spin diagonalizes the Dirac action. The interpolating field for a Wilson heavy and staggered light meson is described in Appendix D.3,

$$\chi^0(x) = \bar{\psi}_H(x)\gamma_5 q(x). \tag{7.20}$$

At this point in the analysis, the temporally oscillating states have been removed by the correlator fit procedure, therefore we can proceed to understand the chiral fit function without considering these states. However, while the heavy quark fields are defined smoothly under transitions around neighboring lattice sites, the light quark fields, due to the staggering are defined only smoothly over the doubled lattice. Therefore, this motivates defining a light quark field which is averaged over the spatial hypercube and is commonly called the spin-taste basis of the staggered fields,

$$q_{\mathrm{avg.}}^{\alpha a}(t, y) = \frac{1}{8}\sum_{\eta} \Omega^{\alpha a}(\eta)\chi(t, 2y + \eta), \tag{7.21}$$

where a and α denote the spin and taste index respectively. It follows that the four quark operator written in the spin-taste basis is given as

$$\mathcal{O}_i(x) = \frac{1}{8}\sum_{\eta} \bar{\psi}_H(t,2y+\eta)\Gamma_i q_{\text{avg.}}(t,2y+\eta)\bar{\psi}_H(t,2y+\eta)\Gamma_i' q_{\text{avg.}}(t,2y+\eta). \quad (7.22)$$

The two fermion bilinear may be separately summed using the following identities

$$\frac{1}{256}\sum_{K} \text{Tr}(\Omega(\eta)K\Omega^\dagger(\eta)K)\text{Tr}(\Omega(\eta')K\Omega^\dagger(\eta')K) = \delta_{\eta,\eta'} \quad (7.23)$$

$$\frac{1}{4}\text{Tr}(\Omega(\eta)K\Omega^\dagger(\eta)K)\Omega(\eta) = K\Omega(\eta)K \quad (7.24)$$

where $K \in \{\gamma_5, i\gamma_\mu\gamma_5, \sigma_{\mu\nu}(\mu < \nu), \gamma_\mu, \mathbb{1}\}$. As a result, the 4-quark operator becomes

$$\mathcal{O}_i = \frac{1}{4}\sum_{K}(\bar{\psi}_H\Gamma_i K q^{cA}_{\text{avg.}}\bar{\psi}_H\Gamma_i' K q^{dB})K_{cA}K_{dB} \quad (7.25)$$

where c, d are the taste indices and A, B are the copy indices. From this equation, we may see that for $K \neq \mathbb{1}$, the spin structure of the 4-quark operator changes from $\Gamma_i \otimes \Gamma_i'$, yielding the SUSY basis, to $\Gamma_i K \otimes \Gamma_i' K$ resulting in wrong-spin contributions. The different tastes also mixing through the contribution from the summation of the taste indices c, d. There is however no copy mixing since on the lattice, copy symmetry is an exact symmetry. Therefore, terms arising from $K \neq \mathbb{1}$ are called wrong-spin taste-mixing contributions.

The wrong-spin taste-mixing terms enter in the sunset and tadpole contributions explicitly represented in Ref [15] are schematically reproduced as,

$$\tilde{\mathcal{Q}}^{(i)} = \frac{ig^2_{D^*D\pi}}{f_\pi^2}\left\{F(\mathcal{H}) + C_Q^{(i)}(\beta,\beta')F(\mathcal{H}, \partial\mathcal{H}/\partial m^2, R, D)\right\}, \quad (7.26)$$

$$\tilde{\mathcal{T}}^{(i)} = \frac{i}{f_\pi^2}\left\{F(\mathcal{I}) + C_T^{(i)}(\beta,\beta')F(\mathcal{I}, \partial\mathcal{I}/\partial m^2, R, D)\right\}, \quad (7.27)$$

where F is a complicated function of the chiral logarithms and residues. However, aside from the terms already encountered in the correct-spin terms, the wrong-spin terms introduce mixing amongst the leading order LEC's β at NLO. Explicitly,

$$C_Q^{(i)} = \left\{\frac{2(\beta_2' + \beta_3')}{\beta_1}, \frac{\beta_3'}{4\beta_2'}, \frac{\beta_2' + \beta_1}{4\beta_3'}, \frac{\beta_5'}{4\beta_4'}, \frac{\beta_4'}{4\beta_5'}\right\}, \quad (7.28)$$

$$C_T^{(i)} = \left\{\frac{2(\beta_2 + \beta_3)}{\beta_1}, \frac{\beta_3}{4\beta_2}, \frac{\beta_2 + \beta_1}{4\beta_3}, \frac{\beta_5}{4\beta_4}, \frac{\beta_4}{4\beta_5}\right\}. \quad (7.29)$$

The mixing between the LO LEC's originate from the fact that in Eq. (7.25), the 4-quark operator was worked out in the spin-taste basis. The matrix elements however, are expressed in the SUSY basis. The spin-taste basis are related to linear combinations of the operators in the SUSY basis and therefore leads to mixing of the LO LECs. In particular, the Standard Model operators $\{\mathcal{O}_1, \mathcal{O}_2, \mathcal{O}_3\}$ and the BSM operators $\{\mathcal{O}_4, \mathcal{O}_5\}$ separately mix as two subgroups. This fact motivates the reason for performing simultaneous chiral fits on the two subgroups, and is the preferred technique used in the following analysis.

7.2 Fitting for systematic errors

7.2.1 Heavy-quark discretization errors

Using the description of Bayesian inference, we account for systematic errors in parallel with the chiral-continuum extrapolation. We include the $\mathcal{O}(\alpha_s a, a^2)$ heavy quark discretization arising from the Lagrangian and operator as an additive correction to the extrapolation. We fold in the error by estimating the error contributions arising from perturbative matching between continuum QCD and lattice QCD through HQET,

$$\mathcal{L}_{\text{QCD}} \doteq \mathcal{L}_{\text{HQET}} = C_j^{\text{cont}}(m_c) \langle \mathcal{O}_j \rangle \,, \tag{7.30}$$

$$\mathcal{L}_{\text{lat}} \doteq \mathcal{L}_{\text{HQET}(m_0 a)} = C_j^{\text{lat}}(m_c, m_0 a) \langle \mathcal{O}_j \rangle \,, \tag{7.31}$$

$$\therefore \text{error}_j = \left| \left[C_j^{\text{lat}}(m_c, m_0 a) - C_j^{\text{cont}}(m_c) \right] \langle \mathcal{O}_j \rangle \right| . \tag{7.32}$$

The $\mathcal{O}(a\alpha_s, a^2)$ errors are included in to the chiral-continuum fit as,

$$F_i^{\text{HQ. error}}(a) = \beta_i (a\Lambda_{\text{HQET}}) z_{B7} f_{B7}(m_0 a) \tag{7.33}$$

$$F_i^{\text{HQ. error}}(a^2) = \beta_i (a\Lambda_{\text{HQET}})^2 \left[z_E f_E(m_0 a) + z_X f_X(m_0 a) + z_Y f_Y(m_0 a) \right] \tag{7.34}$$

$$F_i^{\text{HQ. error}}(a^3) = \beta_i (a\Lambda_{\text{HQET}})^3 z_2 f_2(m_0 a) \tag{7.35}$$

$$F_i^{\text{HQ. error}} \equiv F_i^{\text{HQ. error}}(a) + F_i^{\text{HQ. error}}(a^2). \tag{7.36}$$

The mismatch functions f are discussed in detail in Ref. [8] while the zs are coefficients that are introduced as priors into the fit. The zs are set to $0 \pm \delta$ where δ is determined by power counting and are all under $\mathcal{O}(10)$ and tabulated in Appendix F.

7.2.2 Heavy-quark mistuning corrections

The method of correcting for the heavy quark mistuning are discussed in Section 6. Reproducing Eq. (6.4),

$$\langle \mathcal{O}_i \rangle_{\text{tune}} = \langle \mathcal{O}_i \rangle_{\text{sim.}} + \sigma_i \times \Delta M_2 \tag{7.37}$$

suggests to perform the chiral-continuum extrapolation on the tuned matrix elements. We may however, account for the systematic uncertainty of the shift

$\sigma_i \times \Delta M_2$ by subtracting this effect during the chiral-continuum fit. As a result, the slope and ΔM_2 parameters are described by a distribution introduced by their corresponding priors, and the associated errors are propagated through the analysis. We include these shifts into the chiral fit function,

$$F_i^{\kappa\text{-tune}} = \sigma_i \Delta M_2 \tag{7.38}$$

7.2.3 Renormalization error estimation

In section 5, I discussed how to implement the O(α_s) renormalization corrections. As a result, the renormalization error start at O $\left(\alpha_s^2, \alpha_s \frac{\Lambda_{\text{QCD}}}{m_c}\right)$. Referring back to Eq (5.1) through (5.5), we can write the one-loop renormalization correction as

$$\left\langle D \left| \mathcal{O}_i \right| \bar{D} \right\rangle^R = C_{norm} \left[(1 + \alpha_s \zeta_{ii}) \left\langle D \left| \mathcal{O}_i \right| \bar{D} \right\rangle + \alpha_s \zeta_{ij} \left\langle D \left| \mathcal{O}_j \right| \bar{D} \right\rangle \right], \tag{7.39}$$

where $\mathcal{O}_j$ is the operator which $\mathcal{O}_i$ mixes with under renormalization. For errors that scale as $\alpha_s \frac{\Lambda_{\text{QCD}}}{m_c}$, Eq. (7.33) provides the correct dependence to encapsulate this effect. Since the fitter is not able to differentiate between the $\alpha_s \frac{\Lambda_{\text{QCD}}}{m_c}$ dependence from heavy-quark discretization and renormalization, it is unnecessary to introduce a new $\alpha_s \frac{\Lambda_{\text{QCD}}}{m_c}$ term to capture the renormalization error.

However, for the α_s^2 error, one way to understand this effect is to modify the chiral fit function by estimating these higher order contributions,

$$\begin{aligned} \left\langle D \left| \mathcal{O}_i \right| \bar{D} \right\rangle^R =& C_{norm} \Big[(1 + \alpha_s \zeta_{ii} + \alpha_s^2 \zeta_{ii}^{(3)} + ...) \left\langle D \left| \mathcal{O}_i \right| \bar{D} \right\rangle \\ & + (\alpha_s \zeta_{ij} + \alpha_s \zeta_{ij}^{(3)} + ...) \left\langle D \left| \mathcal{O}_j \right| \bar{D} \right\rangle \Big]. \end{aligned} \tag{7.40}$$

To systematically include this error, I move the α_s^m corrections up to $m = 3$ into the chiral-continuum fit as the following terms,

$$F_i^{\xi_{ii}} = C_{\text{norm}} \alpha_s^2 \xi_{ii} \left\langle \mathcal{O}_i \right\rangle^{\text{lat.}}, \tag{7.41}$$

$$F_i^{\xi_{ij}} = C_{\text{norm}} \alpha_s^2 \xi_{ij} \left\langle \mathcal{O}_j \right\rangle^{\text{lat.}}, \tag{7.42}$$

$$F_i^{\xi_{ii}^{(3)}} = C_{\text{norm}} \alpha_s^3 \xi_{ii}^{(3)} \left\langle \mathcal{O}_i \right\rangle^{\text{lat.}}, \tag{7.43}$$

$$F_i^{\xi_{ij}^{(3)}} = C_{\text{norm}} \alpha_s^3 \xi_{ij}^{(3)} \left\langle \mathcal{O}_j \right\rangle^{\text{lat.}}. \tag{7.44}$$

where the coefficients $\xi = 0 \pm 1$ are introduced as a prior. I define

$$F_i^{\text{renorm}} = F_i^{\xi_{ii}} + F_i^{\xi_{ij}}. \tag{7.45}$$

7.3 Preferred chiral-continuum extrapolation

The preferred fit uses the following fit function

$$F_i^{\text{pref.}} = F_i^{\text{logs}} + F_i^{\text{NLO}} + F_i^{\text{NNLO}} + F_i^{\text{HQ. error}} - F_i^{\kappa\text{-tune}} - F_i^{\text{renorm}}. \tag{7.46}$$

The term $F_i^{\text{logs}} + F_i^{\text{NLO}} + F_i^{\text{NNLO}}$ includes systematic errors from light-quark discretization, gluon discretization, omitting NNLO chiral logarithms, and includes the largest NLO contribution from heavy-meson χPT. The heavy-quark action is tree-level improved, therefore term $F_i^{\text{HQ. error}}$ accounts for systematic errors starting at $\alpha_s a$ and a^2. The term $-F_i^{\kappa\text{-tune}}$ corrects for heavy-quark mistuning and propagates systematic errors from σ_i and κ_{tune}. The shift is applied to the fit function instead of the data, and therefore comes with a negative sign. Finally, the α_s^2 renormalization errors are included by the inclusion of $-F_i^{\text{renorm}}$ where the minus sign reminds us that the correction is performed in the fit function instead of on the data. Systematics that still need to be determined after the chiral-continuum extrapolation include finite volume effects and uncertainty in r_1 when the matrix elements are converted to units of GeV^3. Since the wrong-spin taste-mixing terms mix β_i within the sets $\{\mathcal{O}_1, \mathcal{O}_2, \mathcal{O}_3\}$ and $\{\mathcal{O}_4, \mathcal{O}_5\}$, I simultaneously fit the two sets of operators. The chiral-continuum extrapolation using the preferred fit function and priors listed in Table F.16 are presented in Figure 7.2.

In Figure 7.2, the cyan band is the chiral fit extrapolated to the continuum limit with physical sea quark masses. We can conclude that across all operators and all ensembles, there is slight curvature towards very small valence masses. The source of curvature come from the chiral logarithms. Chiral logarithms are in general functions of the residue times the loop integral,

$$\text{for } \mathrm{m}_{\text{val.}} > \mathrm{m}_{\text{sea}} \begin{cases} R\frac{\partial\mathcal{H}}{\partial m_X^2} \propto & m_X^2 \ln\left(\frac{m_X^2}{\Lambda_\chi^2}\right) \\ D\mathcal{H} \propto & m_X^2 \ln\left(\frac{m_X^2}{\Lambda_\chi^2}\right) \end{cases}, \tag{7.47}$$

$$\text{for } \mathrm{m}_{\text{val.}} < \mathrm{m}_{\text{sea}} \begin{cases} R\frac{\partial\mathcal{H}}{\partial m_X^2} \propto & m_X^2 \ln\left(\frac{m_X^2}{\Lambda_\chi^2}\right) \\ D\mathcal{H} \propto & \ln\left(\frac{m_X^2}{\Lambda_\chi^2}\right) \end{cases}. \tag{7.48}$$

The meson masses M_X constructed from valence quarks range from $M_X \ll \Lambda_\chi$ to $M_X \sim \chi$ and in particular, in the limit of $M_X \to 0$, $R\frac{\partial\mathcal{H}}{\partial m_X^2}$ converges to zero while $D\mathcal{H}$ diverges as a logarithm. During the chiral extrapolation, the sea quark masses are set to the physical values, and therefore is in the region of $\mathrm{m}_{\text{val}} > \mathrm{m}_{\text{sea}}$. However, by extrapolating beyond the physical point as shown in Figure 7.3, the physical point is shown to live far away from the log divergence. The expected log divergence is manifest and well separated from the physical valence quark mass.

Figure 7.2 also suggests that the preferred fit agrees with the simulation data, as shown by the different color lines. For extrapolation lines at non-zero lattice spacing and unphysical sea quark masses, only the central values are shown. Deviations from data for example, in the $\mathcal{O}_1$, $a = 0.045$fm fit are still within one standard deviation. The fits are also highly correlated among different valence masses and operators, therefore, it is not surprising for a fit of a particular ensemble to be affected non-trivially through correlations.

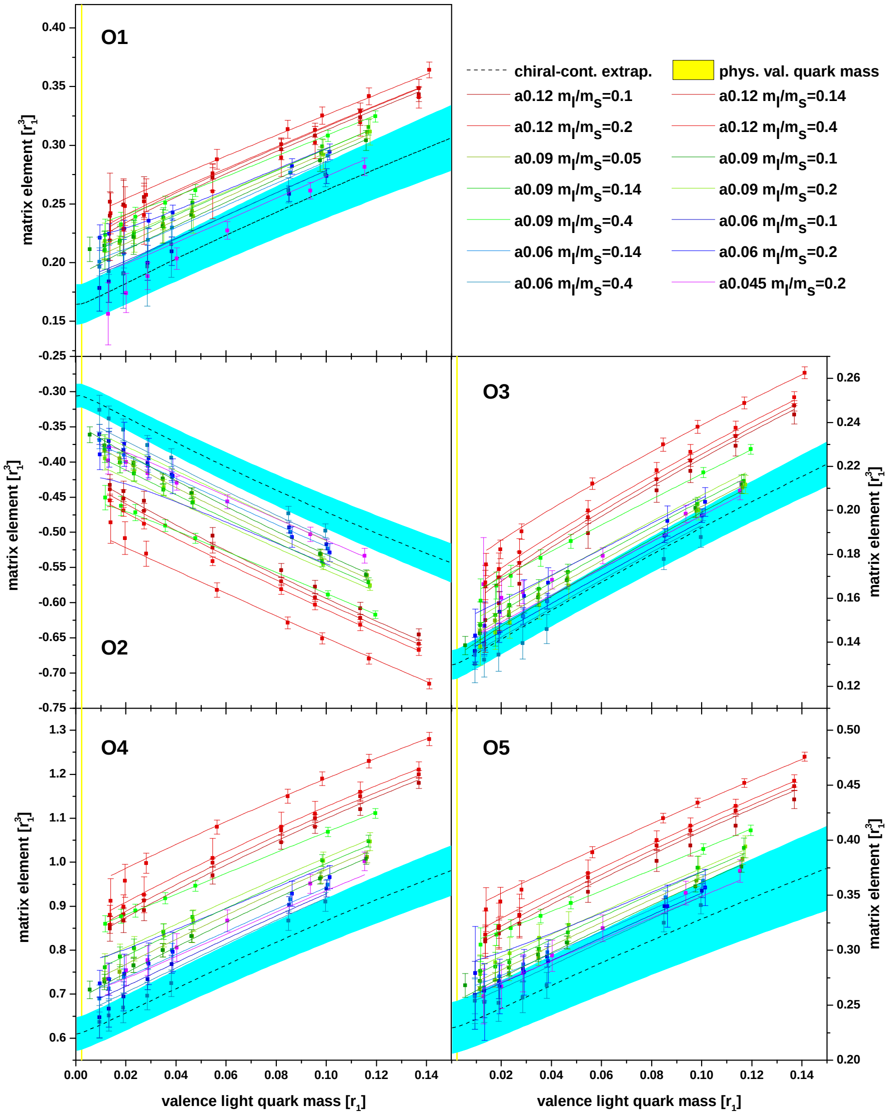

Figure 7.2: Preferred fit for matrix elements of all five 4-quark operators. The black-dotted line with cyan band is the chiral-continuum extrapolation. Colored lines show central values of extrapolations of the valence quark mass at non-zero lattice spacing and unphysical sea quark masses.

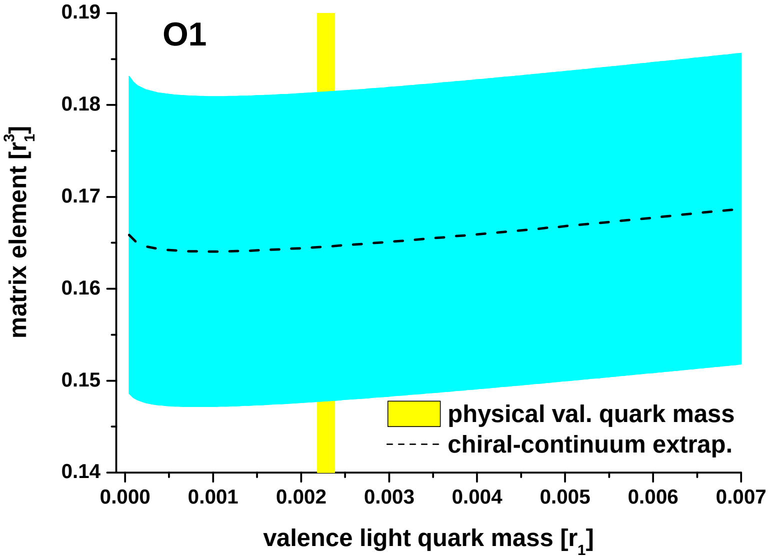

Figure 7.3: Chiral-continuum extrapolation for operator $\mathcal{O}_1$ extrapolated to extremely small pion masses. The log divergence expected in the limit where the valence quark mass goes to zero and is observed far away from the physical pion mass indicated by the yellow band.

Chapter 8

Systematic error analysis

8.1 NLO Chiral logarithms

Errors from $F_i^{\text{logs.}}$ come predominantly from the uncertainty in determining the $\beta_i^{(\prime)}$s, as well as from parametric uncertainty of $g_{D^*D\pi}$. Using a Bayesian fit procedure, these parameters are introduced as priors and the errors associated to these parameters are propagated through the fit function. Since these parameters are promoted to priors, they are part of the data covariance matrix; therefore the partial variance with respect to the $\beta_i^{(\prime)}$s and $g_{D^*D\pi}$, along with sub-dominant contributions from uncertainty in $f_\pi, \Delta^*, \lambda_1, \delta'_V$, and δ'_A is studied to understand the error contribution of the chiral logarithms. Table 8.1 shows the error contribution from the NLO chiral logarithms.

	$\mathcal{O}_1$	$\mathcal{O}_2$	$\mathcal{O}_3$	$\mathcal{O}_4$	$\mathcal{O}_5$
χ-log error	2.8%	1.4%	1.2%	1.1%	2.6%

Table 8.1: Error contributions from chiral logarithms.

8.2 Truncation errors

Truncation errors of the light-quark action and gluon action along with the truncation of χPT at NLO is studied by varying the number of analytic terms as discussed in section 7.1. Starting with the preferred fit, I fit for the following variations,

$$F_i^{\text{NLO}} = F_i^{\text{pref.}} - F^{\text{NNLO}}, \tag{8.1}$$

$$F_i^{\text{NNLO}} = F_i^{\text{pref.}}, \tag{8.2}$$

$$F_i^{\text{gen. NNLO}} = F_i^{\text{pref.}} + F^{\alpha_s a^2}, \tag{8.3}$$

$$F_i^{\text{NNNLO}} = F_i^{\text{pref.}} + F^{\text{NNNLO}}, \tag{8.4}$$

which adds increasingly more analytic terms. Figure 8.1 shows the effect of adding in analytic terms to the fit. We can see that the fits stabilize and errors saturate by adding the NNLO analytic terms. The addition of generic $\alpha_s a^2$ results in almost no change across all five matrix elements. Adding in the full set of NNNLO terms more than doubles the number of analytic terms, yet leads to very stable results of the central value suggesting that systematic truncation errors have been fully accounted. The errors going from NNLO to NNNLO are also less pronounced compared to going from NLO to NNLO suggesting that the errors have saturated. Truncation errors are determined by the partial variance of the coefficients of the analytic terms; Table 8.2 shows their error contribution.

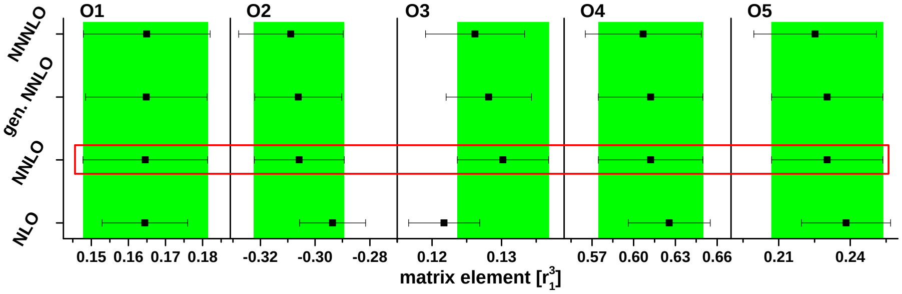

Figure 8.1: Study of truncation errors for all five matrix elements. The preferred fit is boxed in red. The green bands extend the error bar of the preferred fit for comparison with other fits.

	$\mathcal{O}_1$	$\mathcal{O}_2$	$\mathcal{O}_3$	$\mathcal{O}_4$	$\mathcal{O}_5$
truncation errors	3.0%	1.8%	1.7%	1.9%	4.2%

Table 8.2: Error contributions from chiral logarithms.

8.3 Heavy-quark spin and SU(3) flavor symmetry

The pion decay constant f_π provided as an input parameter as a result of using χPT. However, since I am using SU(3) χPT to do the extrapolation, there is freedom to also choose the kaon decay constant f_K. The uncertainty involved in choosing which LEC to use is studied by performing fits with $f_K = 156 \pm 0.2$MeV.

The hyperfine splitting Δ^* and flavor splitting $\delta_{Sx} \propto \lambda_1$ are included in the preferred fit since they are numerically the largest NLO contributions arising from HMχPT. The choice of working strictly in LO of HMχPT is studied by setting Δ^* and λ_1 to zero.

Figure 8.2 show results of fits under the changes described above. All fits vary well within one standard deviation as expected and therefore confirm the expectation that the chiral fits are insensitive to such variations. The shifts in central values of the matrix elements from f_π to f_K is not a higher order correction are not included in the error budget. The changes due to adding the largest NLO HMχPT correction may be included as a systematic error for the

LO HMχPT fit, but in the preferred fit, I choose to include these terms, and therefore the error is included in the error contribution of the chiral logarithms listed in Table 8.1.

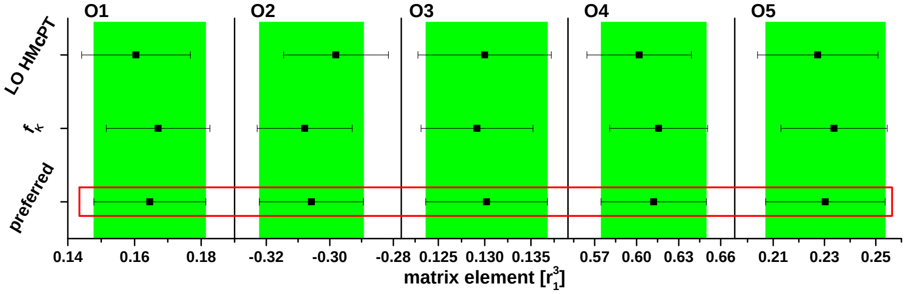

Figure 8.2: Stability under changes from f_π to f_K and truncations in HMχPT for all five matrix elements. The preferred fit is boxed in red. The green bands extend the error bar of the preferred fit for comparison with other fits.

8.4 Heavy-quark discretization errors

I study the heavy quark errors by adding increasingly more terms to the chiral fit function. For the preferred fit, the $\mathrm{O}(\alpha_s a, a^2)$ terms are used. Saturation of the error is seen through fitting the following variations,

$$F_i^{\text{no HQ}} = F_i^{\text{pref.}} - F_i^{\text{HQ. error}}(a) - F_i^{\text{HQ. error}}(a^2), \tag{8.5}$$

$$F_i^{\alpha_s a \text{ HQ}} = F_i^{\text{pref.}} - F_i^{\text{HQ. error}}(a^2), \tag{8.6}$$

$$F_i^{a^2 \text{ HQ}} = F_i^{\text{pref.}}, \tag{8.7}$$

$$F_i^{a^3 \text{ HQ}} = F_i^{\text{pref.}} + F_i^{\text{HQ. error}}(a^3). \tag{8.8}$$

Figure 8.3 shows how the values of the extrapolated matrix elements changes under the above variations. Across all five matrix elements, adding at least one heavy-quark discretization error term saturates the error bars with central values that are stable. For operators $\mathcal{O}_2$ and $\mathcal{O}_3$, the $F_i^{a^3 \text{ HQ}}$ fits is still stable when compared to the changes from $F_i^{\text{no HQ}}$ to $F_i^{\alpha_s a \text{ HQ}}$. The preferred fit is chosen to be the $F_i^{a^2 \text{ HQ}}$ fit since it contains all terms up to the same order, since numerically $\alpha_s \sim a$.

Comparing the error between the $F_i^{\text{no HQ}}$ and $F_i^{\text{pref.}}$ fit, the error contribution from heavy-quark discretization is derived by subtracting the errors in quadrature. Across the five matrix elements, the heavy-quark discretization errors account for approximately 0.6% to 1.6% of the error. From the partial variance of the coefficients in $F_i^{a^2 \text{ HQ}}$, the error contributions is listed in Table 8.3. The values listed in Table 8.3 match the errors derived from comparing $F_i^{\text{no HQ}}$ to $F_i^{\text{pref.}}$. Slight differences occur because while terms in $F_i^{a^2 \text{ HQ}}$ are functions of the heavy-quark mass, and F_i^{analytic} are functions of the light-

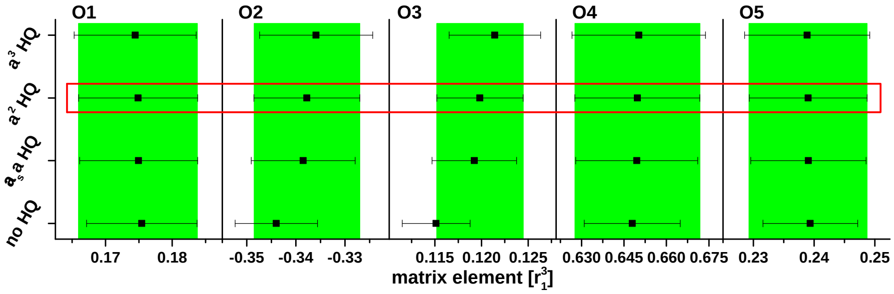

Figure 8.3: Heavy quark discretization error study for all five matrix elements. The preferred fit is boxed in red. The green bands extend the error bar of the preferred fit for comparison with other fits.

quark masses, both terms are also polynomials as a function of lattice spacing a. Therefore, errors from the analytic terms are slightly absorbed by $F_i^{a^2\ \mathrm{HQ}}$.

	$\mathcal{O}_1$	$\mathcal{O}_2$	$\mathcal{O}_3$	$\mathcal{O}_4$	$\mathcal{O}_5$
Heavy-quark errors	1.1%	1.2%	1.1%	1.4%	1.0%

Table 8.3: Heavy-quark discretization errors.

Alternatively, the heavy-quark errors can be estimated through power counting. Using Eq. (7.36), and plugging in values for $\Lambda_{\mathrm{HQET}} = 500\mathrm{MeV}$, and the coefficients $z_E = 2\sqrt{2}, z_{B7} = 3, z_X = 2\sqrt{2}, z_Y = 2$ as motivated by power counting, the heavy quark errors can be conservatively estimated to be approximately 3.5%. This estimate however, assume that all matching calculations enter in with the same sign and therefore serves as an upper bound to this estimate. I will choose to account for heavy-quark errors as estimated from the fitter.

8.5 Validity of χPT

Chiral perturbation theory is the low energy effective theory of QCD, describing a theory of mesons lighter than the chiral scale λ_χ. The theory has eight Goldstone bosons which correspond to the pions, kaons and eta. Therefore the scale is commonly set to the rho meson mass at 775 MeV. Some of the heaviest valence quark masses in the dataset however, go up to approximately 860MeV. To check that the heavy valence mass points do not introduce systematic errors, fits with meson masses up to only 560MeV are studied. Similarly, fits where the largest lattice spacing data at $a = 0.12$fm are dropped to determine the stability of the continuum extrapolation.

Figure 8.4 shows that while fitting exclusively with pions lighter than 560MeV, the central values of the fits shifts are within one standard deviation of the preferred fit. On the other hand the errors bars are smaller by up to 7% with the

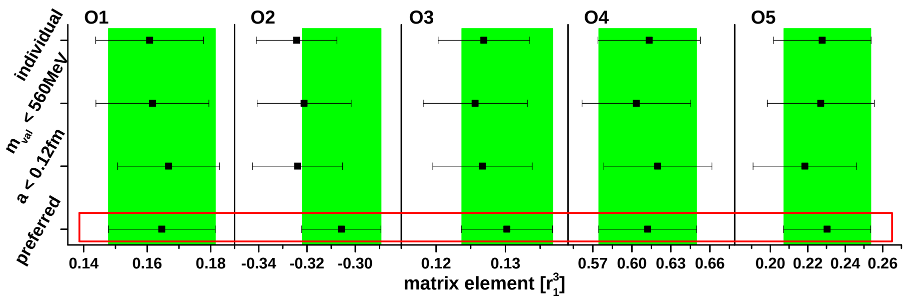

Figure 8.4: Stability of fits across less correlated, more chiral, and more continuum like data. The preferred fit is boxed in red. The green bands extend the error bar of the preferred fit for comparison with other fits.

inclusion of more data. Therefore, the preferred fits use all the available data.

Removing the 0.12fm data results in shifts in central values of 6.0% for $\mathcal{O}_2$ down to 1.3% for $\mathcal{O}_4$ with a corresponding error increase of up to 6% for all operators except for $\mathcal{O}_1$. The shift in central value and the corresponding increase in error suggests that the two fits are statistically consistent. The differences are mainly attributed to cutting away approximately one-third of the data. Therefore for the preferred fit, ensembles up to 0.12fm lattice spacing is used.

The wrong-spin taste-mixing contributions mix leading-order LECs. Datasets for individual operators only contain information on the leading-order LECs at NLO as shown by Eq. (7.29), therefore motivating fits across the SM and BSM sets of operators. Figure 8.4 shows that performing individual fits may introduce some systematic uncertainty as shown in shifts in central values for $\mathcal{O}_2$ and $\mathcal{O}_3$. Therefore, for the preferred fit, simultaneous fits over the SM and BSM sets of operators are performed.

8.6 Renormalization error

The α_s^2 renormalization error arise from truncating the renormalization calculation at one-loop. One way to estimate this error is to calculate the value of α_s^2 at the finest lattice spacings. This assumes that the coefficients are of O(1). Under this assumption, the renormalization errors are approximately 6.5% for all operators.

Another way to estimate the renormalization error is to modify the fit function with increasing number of corrections to the renormalization and observe error saturation similar to the study of truncation errors. The following fits are studied,

$$F_i^{\alpha_s} = F_i^{\text{pref.}} - (-1)F_i^{\xi_{ii}} - (-1)F_i^{\xi_{ij}}, \tag{8.9}$$

$$F_i^{\alpha_s^2 \text{ diag.}} = F_i^{\text{perf.}} - (-1)F_i^{\xi_{ij}}, \tag{8.10}$$

$$F_i^{\alpha_s^2 \text{ comp.}} = F_i^{\text{pref.}}, \tag{8.11}$$

$$F_i^{\alpha_s^3 \text{ diag.}} = F_i^{\text{pref.}} + (-1)F_i^{\xi_{ii}^{(3)}}, \tag{8.12}$$

$$F_i^{\alpha_s^3 \text{ comp.}} = F_i^{\text{pref.}} + (-1)F_i^{\xi_{ii}^{(3)}} + (-1)F_i^{\xi_{ij}^{(3)}}. \tag{8.13}$$

Figure 8.5 shows that the chiral fits stabilize and error bars saturate for all operators when adding in a complete set of α_s^2 terms. Comparing the error bars between the one-loop renormalized fit $F_i^{\alpha_s \text{ renorm}}$ and the preferred fit $F_i^{\alpha_s^2 \text{ complete}}$, the renormalization error varies from as small as 3.3% for operator $\mathcal{O}_5$ and as large as 9.2% for operator $\mathcal{O}_2$. These errors reflect what is expected from power counting with O(1) coefficients. The error contributions from the partial variance listed in Table 8.5 range from 2.4% to 6.1% and are all smaller, but consistent with the 6.5% expectation from power counting. In this method data is used to constrain the renormalization errors, resulting in a more robust estimate. When comparing the statistical error between $F_i^{\alpha_s \text{ renorm.}}$ and $F_i^{\alpha_s^2 \text{ complete}}$, the $F_i^{\alpha_s^2 \text{ complete}}$ fits universally have larger statistical errors. This is consistent with the operators receiving the smallest and largest renormalization error derived from subtracting total error bars in quadrature. The errors from the partial variance however, suggest that improving statistical errors may lead to not only an improvement in statistical resolution, but also improved renormalization errors since the two are strongly correlated.

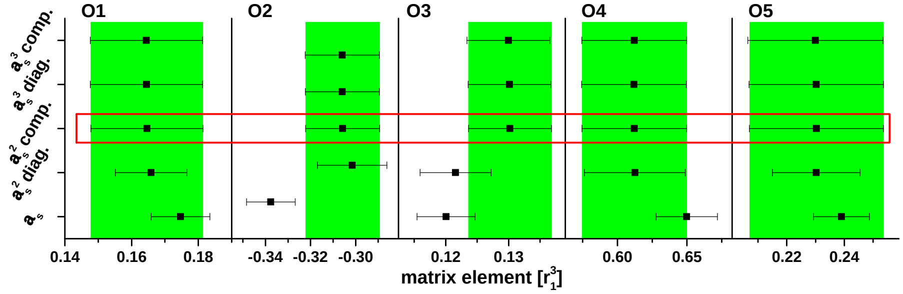

Figure 8.5: Study of renormalization error. The preferred fit is boxed in red. The green bands extend the error bar of the preferred fit for comparison with other fits.

	$\mathcal{O}_1$	$\mathcal{O}_2$	$\mathcal{O}_3$	$\mathcal{O}_4$	$\mathcal{O}_5$
Renormalization errors	6.1%	2.9%	2.4%	4.0%	5.3%

Table 8.4: Percent increase in error bar and change in central value. Values are calculated by comparing the error bars in quadrature.

In addition to α_s^2 renormalization errors, there are $\alpha_s \Lambda_{\mathrm{QCD}}/m_c$ renormalization errors that are numerically of the same order. Discussed in Section 7.2.3, there errors scale in the same manner as the term in the heavy-quark discretization errors with coefficient z_{B7}. From power-counting estimates of the contribution to the mismatch function f_{B7}, the prior for $z_{B7} = 0 \pm 3$. In Figure 8.6, I double the prior width to $z_{B7} = 0 \pm 6$ and stability is observed indicating that $\mathrm{O}(\alpha_s \Lambda_{\mathrm{QCD}}/m_c)$ renormalization errors are properly accounted for.

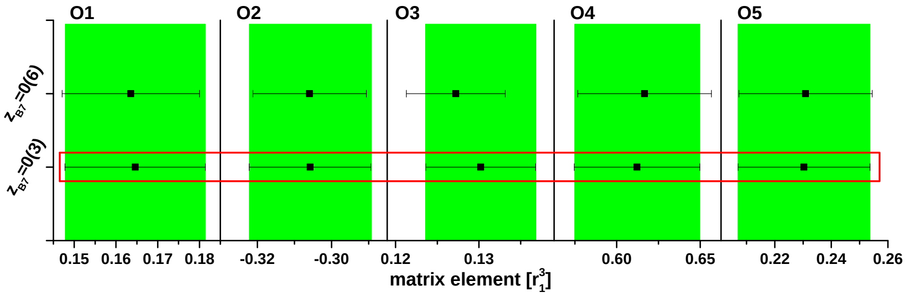

Figure 8.6: Study of $\alpha_s \Lambda_{\mathrm{QCD}}/m_c$ renormalization error. The preferred fit is boxed in red. The green bands extend the error bar of the preferred fit for comparison with other fits.

8.7 Finite volume effects

Finite volume effects are expected to be very small since most ensembles have box sizes of $m_\pi L \gtrsim 4$. Previous studies from Ref. [8] for the D-meson decay constant analysis concluded that finite volume effects are $< 1\%$, and is the number that I am quoting.

8.8 Heavy-quark tuning and light-quark masses

Uncertainty of determining the mass of the physical charm quark is captured by $F_i^{\kappa\text{-tune}}$. The partial errors are propagated through the chiral fit function and tabulated in Table 8.5.

The uncertainty of the physical up quark mass is an input error when extrapolating to the physical quark mass. Standard error propagation is used to account for this error. The value of the physical up quark mass m_u is given in Table VIII of Ref. [7]. There is approximately a 3.5% error on the determination of the physical up quark mass. The error is propagated through the chiral fit function and tabulated in Table 8.5.

	$\mathcal{O}_1$	$\mathcal{O}_2$	$\mathcal{O}_3$	$\mathcal{O}_4$	$\mathcal{O}_5$
Heavy-quark mistuning	2.5%	0.3%	0.4%	0.2%	1.2%
Phys. light-quark uncertainty	0.4%	0.4%	0.4%	0.6%	0.2%

Table 8.5: Partial errors from heavy-quark mistuning and physical light-quark mass uncertainties.

8.9 Final error budget

In this section I provide the combined statistical and systematic error budget as well as a breakdown of errors. Statistical errors normally are determined by the fitter. Since I am using Bayesian constraints, in this analysis, the covariance matrix now include not only the data covariance, but also the posteriors of the priors. Therefore, the statistical error is the partial error related to the data. The complete error budget is provided in Table 8.6.

	$\mathcal{O}_1$	$\mathcal{O}_2$	$\mathcal{O}_3$	$\mathcal{O}_4$	$\mathcal{O}_5$
Statistical	6.3%	3.5%	3.5%	3.8%	6.8%
Total χ-cont. err.	3.9%	2.1%	1.9%	2.2%	5.0%
Heavy-quark disc.	1.1%	1.2%	1.1%	1.4%	1.0%
Renormalization	6.1%	2.9%	2.4%	4.0%	5.3%
HQ mistuning	2.5%	0.3%	0.4%	0.2%	1.2%
LQ mass uncert.	0.4%	0.4%	0.4%	0.6%	0.2%
Finite volume			<1%		
Total error	10.0%	5.1%	4.8%	6.1%	10.1%

Table 8.6: Complete error break down for all five operators.

Chapter 9

Results and outlook

Here I report the results of the non-relativistically normalized D-meson mixing matrix elements with a 2+1 dynamical fermion sea, evaluated at 3GeV $\overline{\text{MS}}$-NDR scheme with BBGLN choice of evanescence operators in units of GeV^3.

	$\mathcal{O}_1$	$\mathcal{O}_2$	$\mathcal{O}_3$	$\mathcal{O}_4$	$\mathcal{O}_5$
$\left\langle D \left\vert \mathcal{O}_i \right\vert \bar{D} \right\rangle / m_D$ [GeV^3]	0.042(4)	-0.078(4)	0.033(2)	0.155(10)	0.058(6)

Table 9.1: D-meson mixing matrix elements for all five operators.

It is customary to parametrize the matrix elements in terms of bag parameters,

$$\langle D \left\vert \mathcal{O}_i \right\vert D \rangle = \mathcal{C}_i m_D^2 f_D^2 B_D^{(i)} \tag{9.1}$$

with coefficients $C_i = \left\{ \frac{2}{3}, -\frac{5}{12}, \frac{1}{12}, \frac{1}{2}, \frac{1}{6} \right\}$. m_D is the D-meson mass, f_D is the D-meson decay constant, and $B_D^{(i)}$ is the bag parameter for operator $\mathcal{O}_i$. When the bag parameter B_D is set to 1., this choice is called the vacuum saturation approximation. This project allows us to rigorously calculate the bag parameters using QCD and avoid this approximation. To extract the bag parameters however, decay constants are needed. The Fermilab Lattice collaboration currently is working on extracting the D-meson decay constants from the same MILC asqtad ensembles. With the completion of that project, we will be able to report bag parameters for D-mixing.

Recently, the European Twisted Mass (ETM) collaboration has published a paper on the D-meson mixing matrix elements as well, using $N_f = 2$ twisted mass fermions [24]. This is a completely independent calculation using Wilson type fermions for both the sea and valence quarks. Figure 9.1 compares $\langle \mathcal{O}_1 \rangle$, the Standard Model V-A current operator, from this work with published results from the ETM collaboration. They pleasantly agree.

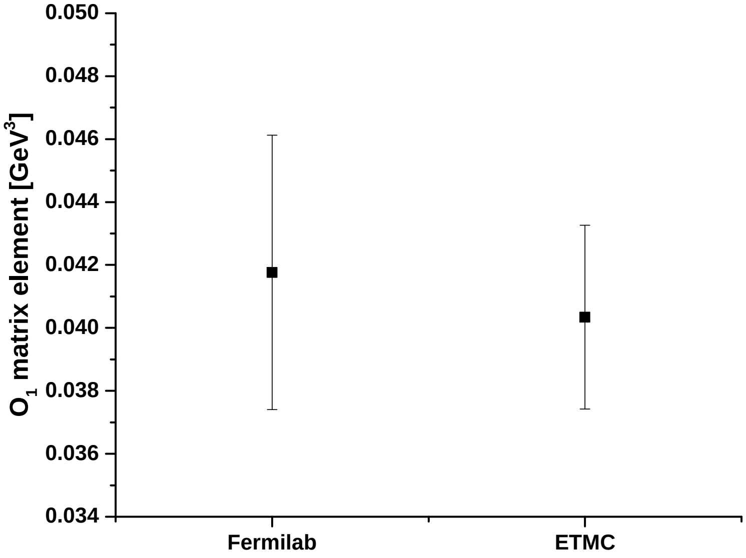

Figure 9.1: Comparison of the $\mathcal{O}_1$ matrix element with an independent calculation from ETMC.

Appendix A

Gauge Field Action

In the continuum, the gauge fields in QCD are described by the gluon fields $A_\mu(x)$. On the lattice however, the gauge fields are described by link operators $U_\mu(x)$. The gauge links can be viewed as parallel transports which tie one lattice site to another. Explicitly, the gauge links are

$$U_\mu(x) = P \exp\left[ig \int_x^{x+a\hat{\mu}} dy_\nu A_\nu(y)\right] \tag{A.1}$$

where P is the path ordered operator. The reason why it is beneficial to use the link operator instead of the more familiar field operator A_μ is because the trace of a Wilson loop constructed by link fields is gauge invariant at finite lattice spacing. It is then possible to construct a gauge invariant analogue to continuum QCD with the link operators. The reason why gauge invariance is such an attractive feature to have is because with gauge invariance, the couplings to all the vertices will be the same. For example, without gauge symmetry, the coupling of the quark-gluon vertex will be different from the three gluon vertex. While it is possible to compute such a theory on the lattice, it is computationally more expensive; therefore LQCD is formulated to be gauge invariant. With this definition of the gauge field, it is now possible to construct the gauge action. In the continuum, the Yang-Mills action is

$$S_{YM} = \int d^4x \frac{1}{2} \sum_{\mu\nu} \mathrm{Tr} F_{\mu\nu}^2(x) \tag{A.2}$$

The simplest discretized gauge action is the plaquette action

$$S_G = \frac{\beta}{N} \sum \Re \mathrm{Tr}\left(1 - U_{pl}\right); \, \beta \equiv \frac{2N}{g^2} \tag{A.3}$$

which is summed over every plaquette with the same orientation on the lattice. U_{pl} is a product of gauge links U_μ that construct a plaquette on the lattice. The plaquette is the smallest Wilson loop that is able to be constructed on the lattice. Eq. (A.4) shows how the plaquette is explicitly constructed by the gauge links and figure A.1 shows how the Wilson loop may be drawn on a lattice.

$$U_{pl} = U_\mu(x) U_\nu(x + a\hat{\mu}) U_\mu^\dagger(x + a\hat{\nu}) U_\nu^\dagger(x) \tag{A.4}$$

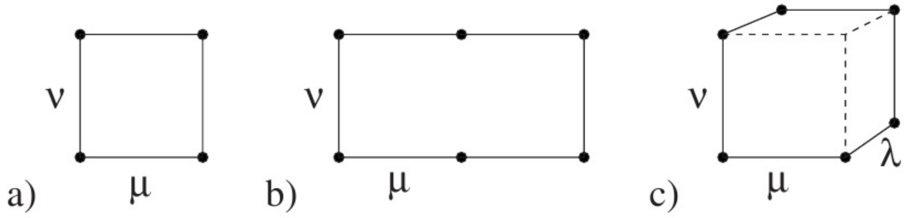

Figure A.1: Schematic diagram for a) plaquette, b) rectangle and c) parallelogram. Picture courtesy of the MILC collaboration.[10]

It can be shown that the plaquette action agrees with the continuum action up to order a^2 in lattice spacing. It is very important however, to be able to improve the action on the lattice as much as possible in order to make high precision calculations. Efforts to improve lattice actions to higher order in lattice spacing are called Symanzik improvements.

A.1 Tadpole Improvement

Before improving the O(a^2) discretization errors of the plaquette action, it is important to first understand the consequence of using $U_\mu(x)$ instead of the gauge fields in constructing actions. It is most straightforward to understand this issue by expanding the gauge link in terms of lattice spacing.

$$\begin{aligned} U_\mu(x) &\approx \exp\left[-iagA_\mu\right] \\ &= 1 - iagA_\mu + \mathcal{O}\left(a^2\right) \end{aligned} \tag{A.5}$$

Eq. (A.5) shows that the leading order of U_μ is the gauge field, however the gauge link also includes all powers of agA_μ. In practice, if the gauge link is used to describe the gluon in the quark-gluon vertex for example, then it is clear that the vertex will contain the usual $\bar{\psi}A_\mu\psi$ term as well as lattice artifacts of the form $\bar{\psi}\left(A_\mu\right)^n\psi$. These lattice artifacts are called tadpole contributions. The tadpoles must be resumed and divided out in order for lattice calculations to be comparable to results in the continuum. Without eliminating the tadpole contributions, lattice QCD calculations using the bare coupling start to deviate from the results of continuum QCD earlier than what the perturbation theory suggested [44]. To account for these tadpole contributions, the gauge link is divided by the mean value of the link u_0.

$$U_\mu(x) \rightarrow \frac{1}{u_0}U_\mu(x) \tag{A.6}$$

$$u_0 = \langle 0\left|P_{\mu\nu}\right|0\rangle^{\frac{1}{4}} \tag{A.7}$$

Eq. (A.7) gives the alternate definition of u_0 which is the fourth root of the plaquette expectation value. This is the definition used in practice since it is the most convenient definition.

A.2 Symanzik Improvement: Gauge Field Improvement

The order a^2 improved gauge action is called the Lüscher-Weisz action, which along with the plaquette (pl) action, gains a Rectangle (rt) and Parallelogram (pg) term. The tadpole improved Lüscher-Weisz action is

$$\begin{aligned} S_{LW} =& \frac{\beta_{LW}}{3}\Big\{\sum \Re\mathrm{Tr}\left(1 - U_{pl}\right) \\ & - \sum \frac{[1 + 0.4805\alpha_s]}{20u_0^2} \Re\mathrm{Tr}\left(1 - U_{rt}\right) \\ & - \sum \frac{0.03325\alpha_s}{u_0^2} \Re\mathrm{Tr}\left(1 - U_{pg}\right)\Big\} \end{aligned} \tag{A.8}$$

where $\beta_{LW} \equiv u_0^{-4}\beta c_{pl}$ and $\alpha_s \equiv -1.303615 \ln u_0$.[10] The coefficients in front of the three Wilson loop terms were determined by Lüscher and Weisz and can be written in terms of c_{pl}, the coefficient of the plaquette.[48] [1] α_s is the non-perturbatively renormalized coupling. Written in the form of Eq. (A.8), it is clear that the Lüscher-Weisz action is improved up to $\mathcal{O}\left(\alpha_s a^2\right)$.

---

[1] Lüscher and Weisz computed the static quark potential as well as some more complicated on-shell quantity to determine the value of the coefficient.

Appendix B

Fermion Actions

When dealing with fermions on the lattice, the naive thing to do is to discretize the Dirac action. The symmetric Dirac Hamiltonian is defined as

$$H_{\text{Dirac}} = \int d^3\mathbf{x}\bar{\psi}(\mathbf{x}) \left\{ m + \frac{i}{2}\gamma_k \left(\frac{\overleftarrow{\partial}}{\partial x_k} - \frac{\overrightarrow{\partial}}{\partial x_k} \right) \right\} \psi(\mathbf{x}) \tag{B.1}$$

where $k = \{1, 2, 3\}$. Replacing the derivative with the finite difference operator and Fourier transforming into momentum space yields the naive lattice Hamiltonian, shown in Eq. (B.2).

$$H_{\text{naive}} = \frac{1}{(aL)^3} \sum_{\mathbf{q}} \bar{\psi}_{\mathbf{q}} \left\{ m + \frac{1}{a}\gamma_k \sin(q_k) \right\} \psi_{\mathbf{q}} \tag{B.2}$$

appro The eigenvalues of the naive Hamiltonian are

$$E_{\mathbf{q}}^2 = m^2 + \frac{1}{a^2} \sum_k \sin(q_k). \tag{B.3}$$

The energy-momentum relation is attained by setting $\mathbf{p} \equiv \mathbf{q}/a$. Expanding Eq. (B.3) in the small $\mathbf{p}$ limit yields $E^2 = m^2 + \mathbf{p}^2 + \mathcal{O}\left(a^2\right)$ which at the limit of $a \to 0$ returns the continuum result. Eq. (B.3) suggests that the discretized Hamiltonian is well behaved at least at small enough lattice spacing. However, a closer look at Eq. (B.3) suggests that the continuum energy momentum relation may be attained not only for small values of $\mathbf{q}$, but are also attained for values of $\mathbf{q} + \boldsymbol{\pi}$. As a result, in 4 dimensions, there are 16 'tastes' which possess the same energy-momentum relation. This phenomena is referred to as fermion doubling.

In general, fermions on the lattice have to obey the Nielson-Ninomiya no-go theorem [] which states that one may not construct a local fermion action that is chirally and translationally invariant without doublers. Therefore, different formulations of the lattice fermion action respect the no-go theorem by either breaking chiral symmetry (Wilson fermions), redefining the notion of locality (chiral fermions), or keeping the doublers (staggered fermions). While every fermion action has its strengths and compromises, this project uses the improved staggered action for the light valence and sea quarks, while the Fermilab interpretation of the improved Wilson action is used to describe the heavy charm quark. And therefore, I will focus my discussion on the these two actions.

B.1 Wilson fermions

Wilson fermions eliminate all of the doublers in the theory at the expense of breaking chiral symmetry. Since the doublers live on non-zero momentum vertices of the Brillouin zone as shown by Eq. (B.3), the Wilson action introduces an additive mass-like term such that every taste fermion gains a mass of order $1/a \gg \Lambda_{\text{QCD}}$. The additive mass term decouples the taste fermions from the theory but explicitly breaks chiral symmetry with the introduction of a $\bar{\psi}\psi$ term. Wilson introduced an additional dimension 5 operator to the naive action, corresponding to the second derivative operator. Eq. B.4 shows the discretized Wilson term as the symmetric second order finite difference operator, and since the operator is also in the form of a Fermion bilinear, it also transforms under chiral rotations similar to a mass term.

$$H_{\text{Wilson}} = H_{\text{Dirac}} - a^3 \sum_{\mathbf{x}} \frac{r}{2a} \sum_{k=1}^{3} \left[\bar{\psi}_{\mathbf{x}+\hat{k}}\psi_{\mathbf{x}} - 2\bar{\psi}_{\mathbf{x}}\psi_{\mathbf{x}} - \bar{\psi}_{\mathbf{x}}\psi_{\mathbf{x}+\hat{k}}\right] \tag{B.4}$$

where $0 < r \leq 1$ is the Wilson parameter; while the naive Hamiltonian is reproduced by setting $r = 0$. The Fourier transform of Eq. B.4 yields Eq. B.5.

$$H_{\text{Wilson}} = H_{\text{Dirac}} + \frac{1}{(aL)^3} \sum_{\mathbf{q}} \frac{r}{a} \bar{\psi}_{\mathbf{q}} \sum_{k=1}^{3} (1 - \cos q_k)\, \psi_{\mathbf{q}} \tag{B.5}$$

Eq. (B.5) shows that the Wilson terms only add diagonal elements to the naive Hamiltonian, therefore the eigenvalues of the Wilson Hamiltonian may be attained by the following substitution $m \to m + \frac{r}{a} \sum_k (1 - \cos q_k)$.

$$E_{\mathbf{q}}^2 = \left[m + \frac{r}{a} \sum_{k=1}^{3} (1 - \cos q_k)\right]^2 + \sum_{k=1}^{3} \frac{1}{a^2} \sin^2 q_k \tag{B.6}$$

The eigenvalues of the Wilson Hamiltonian shows that for $\mathbf{q} = \mathbf{0}$, the solution to the naive Hamiltonian is reproduced. For the other taste fermions where $q_k = \pi$, the mass gains an additive term $m \to m + 2\frac{r}{a}$ resulting in the extra tastes gaining infinite mass in the limit where $a \to 0$. Since the Wilson term introduces a dimension 5 operator to the theory, scaling violations start at $\mathcal{O}(a)$. The improved Wilson action corrects the tree-level $\mathcal{O}(a)$ discretization errors and will be discussed in the following section.

B.1.1 The clover action

As with all lattice actions, the Wilson action may be thought of as QCD with a lattice regularization scheme. Therefore, deviations from continuum QCD may be systematically improved order by order in powers of a^n. Improvements to the action around powers of the lattice spacing are commonly referred to as Symanzik improvements. Under this system, the Wilson action may be written down up to dimension 5 as the following,

$$\begin{aligned} S_{\text{clover}} =& \frac{m_0 a}{a}\bar{\psi}(x)\psi(x) + \bar{\psi}(x)\not{D}\psi(x) && \text{(B.7)} \\ &+ a r_s \bar{\psi}(x)\not{D}^2\psi(x) + iac_{\text{SW}}\bar{\psi}(x)\sigma_{\mu\nu}F^{\mu\nu}\psi(x) && \text{(B.8)} \end{aligned}$$

where m_0, r_s and c_{SW} are couplings and in particular, m_0 fixes the fermion mass, r_s is a redundant coupling used to solve the doubling problem, while c_{SW} is chosen to improve the action through $\mathcal{O}(a)$ at tree-level. The couplings are based on the renormalizatoin group and are dependent on the fermion masses $m_0 a$ and gauge coupling g_0^2. When the clover action is used to simulate heavy quarks, it is common to take the limit in which $m_q \gg \Lambda_{\text{QCD}}$. This non-relativistic treatment assumes the existence of a heavy quark scale which is well separated from the typical strong interaction scale, and expansions in orders of $\mathbf{p}/m_q$ are used to correct for dynamical behavior. On the other hand, for light quarks, it is natural to expand in orders of $m_0 a$. However, for this project, the charm quark is only slightly heavier than the typical strong interaction scale, and therefore a different interpretation of the clover action is used.

B.1.2 Fermilab Interpretation

For a typical heavy-light process, one may naively picture a light quark being bound to a nearly stationary heavy quark. Therefore, the relevant small parameter in this system is the three-momentum. The Fermilab interpretation assumes only that the $\mathbf{p}a \ll 1$ and makes no assumption on the size of the fermion mass. As a result, in the limit of $m_0 a \to 0$ the coefficients in [59] are recovered, while in the limit of $m_q \gg \Lambda_{\text{QCD}}$ the coefficients are bounded, leaving only order $\mathbf{p}a$ and $\Lambda_{\text{QCD}}a$ corrections. The Fermilab interpretation of the clover action is well behaved for all quark masses, and may be used to simulate the charm quark with controlled systematic errors.

Since the Fermilab interpretation no longer treats space and time on equal footing, axis-interchange symmetry is broken. The discretized version of the clover action in the Fermilab interpretation is given as,

$$\begin{aligned}S_0 =& m_0 \int \bar{\psi}(x)\psi(x) \\ &+ \int \left[\bar{\psi}(x)\frac{1}{2}\left(1+\gamma_0\right) D_0^- \psi(x) - \bar{\psi}(x)\frac{1}{2}\left(1-\gamma_0\right) D_0^+ \psi(x)\right] \\ &+ \zeta \int \bar{\psi}(x)\boldsymbol{\gamma}\cdot\mathbf{D}\psi(x) \\ &- \frac{1}{2}ar_s\zeta \int \bar{\psi}(x)\Delta^{(3)}\psi(x), \end{aligned} \tag{B.9}$$

$$S_B = -\frac{i}{2}ac_B\zeta \int \bar{\psi}(x)\boldsymbol{\Sigma}\cdot\mathbf{B}(x)\psi(x), \tag{B.10}$$

$$S_E = -\frac{1}{2}ac_E\zeta \int \bar{\psi}\boldsymbol{\alpha}\cdot\mathbf{E}(x)\psi(x), \tag{B.11}$$

where $\int \to a^4 \sum_x$ and the derivatives are covariant different operators defined as,

$$D_0^+\psi(x) = a^{-1}\left[U_0(x)\psi(x+a\hat{0}) - \psi(x)\right], \tag{B.12}$$

$$D_0^-\psi(x) = a^{-1}\left[\psi(x) - U_0^\dagger(x-a\hat{0})\psi(x-a\hat{0})\right], \tag{B.13}$$

$$D_i\psi(x) = (2a)^{-1}\left[U_i(x)\psi(x+a\hat{i}) - U_i^\dagger(x-a\hat{i})\psi(x-a\hat{i})\right], \tag{B.14}$$

$$\Delta^{(3)}\psi(x) = a^{-2}\sum_{i=1}^{3}\left[U_i(x)\psi(x+a\hat{i}) + U_i^\dagger(x-a\hat{i})\psi(x-a\hat{i}) - 2\psi(x)\right]. \tag{B.15}$$

After breaking axis interchange symmetry, the theory is now parametrized by the following couplings, $\{\zeta, r_s, c_B, c_E\}$, where $m_0 a = \frac{1}{2\kappa_t} - [1 + 3r_s\zeta]$ and $\zeta = \kappa_s/\kappa_t$. The bare coupling is now related to the temporal and spatial κ values, while c_{SW} is split into c_B and c_E.

The dispersion relation of the heavy quark

$$E^2 = M_1^2 + \frac{M_1}{M_2}\mathbf{p}^2 \tag{B.16}$$

$$M_1 = m_q = \ln\left(1+m_0\right) \tag{B.17}$$

$$M_2^{-1} = \frac{2\zeta^2}{m_0(2+m_0)} + \frac{r_s\zeta}{1+m_0} \tag{B.18}$$

becomes $E^2 = m_q^2 + \mathbf{p}^2$ and therefore describes a particle of mass m_q in terms of the bare mass m_0. However, in practice it is only necessary to set the kinetic mass M_2 to the physical mass. This is because the heavy quark at first order is stationary with respect to the light quark while corrections to this description depend only on the kinetic mass. A detailed description of the non-perturbative tuning for κ is given in Ref. [16], while c_B and c_E are chosen to correct for $\mathcal{O}(a)$ scaling violations. Therefore, the charm quark has systematic error originating from the action starting at $\mathcal{O}(\alpha_s a, a^2)$.

B.2 Staggered Fermions

The light quarks are simulated using the staggered formulation of QCD. The staggered formulation obeys the Nielson-Ninomiya theorem by reducing the number of doublers, without completely eliminating the taste-states. However, as a result, the staggered formulation preserves a reduced chiral symmetry which is a necessary condition needed to construct a chiral effective theory needed later in the analysis. From a simulation standpoint, the staggered formulation is also the cheapest type of quark to simulate. This translates to the ability of obtaining relatively high amounts of statistics at a low cost compared to other fermion formulations. Therefore, a staggered-type action is used to describe the sea quarks as well as the light valence quark in this project.

Referring back to Eq. B.3, the doublers live on the edges of the hypercube in momentum space. Therefore, if one were to effectively increase the lattice spacing, it is possible to work in a theory where the doublers are pushed outside of the Brillouin zone. Starting from a naive field with four spin degrees of freedom per lattice site, the staggered formulation redistributes the spin degrees of freedom onto neighboring lattice sites. In a 4-dimensional space-time lattice, four 'tastes' would completely define all 16 degrees of freedom within the unit hypercube, and therefore, effectively doubling the lattice spacing and eliminating the other 15 tastes which now live outside of the Brillouin zone.

Starting from the naive action, the following transformations diagonalizes the action in spin space,

$$\psi(x) = \Omega_x \chi(x) \tag{B.19}$$

$$\bar{\psi}(x) = \bar{\chi}(x) \Omega_x^\dagger, \tag{B.20}$$

$$\tag{B.21}$$

where

$$\Omega_x = \gamma_1^{\frac{x_1}{a}} \gamma_2^{\frac{x_2}{a}} \gamma_3^{\frac{x_3}{a}} \gamma_4^{\frac{x_4}{a}} . \tag{B.22}$$

Defining

$$\eta_\mu(x)\mathbb{1} \equiv \Omega_x^\dagger \gamma_\mu \Omega_{x+a\hat{\mu}} = (-1)^{(x_1+\ldots+x_{\mu-1})/a}\mathbb{1}, \tag{B.23}$$

the naive action is rewritten as the spin-diagonalized Kogut-Susskin action for a single flavor as,

$$S_{\mathrm{KS}} = \sum_x \bar{\chi}(x) \left\{ \sum_\mu \eta_\mu(x)\mathbb{1}\nabla_\mu \chi(x) + m\mathbb{1}\chi(x) \right\} . \tag{B.24}$$

At this point, the action is spin-diagonalized, which may be interpreted as the spin degrees of freedom being distributed to neighboring lattice sites. We may now eliminate the number of tastes down to 4 by working with only one component or 'copy' in Eq. B.24, and the resulting action is called the staggered action.

In the limit $m \to 0$, this action in invariant under $\mathrm{U}(1)_e \otimes \mathrm{U}(1)_o$ transformation,

$$\chi(x) \to e^{i\alpha_e}\chi(x), \qquad \bar{\chi}(x) \to \bar{\chi}(x)e^{-i\alpha_o}, \tag{B.25}$$

for $\sum_i x_i/a = \text{even}$,

$$\chi(x) \to e^{i\alpha_o}\chi(x), \qquad \bar{\chi}(x) \to \bar{\chi}(x)e^{-i\alpha_e}, \tag{B.26}$$

for $\sum_i x_i/a = \text{odd}$.

The action may be rewritten in the more familiar form of a four-component Dirac field over the doubled lattice. In four dimensions, the Dirac field now occupies a hypercube of volume 2^4, and the lattice spacing is now enlarged from $a \to 2a$. The Dirac field $q(y)$ in terms of one-component staggered field is,

$$q(y)_{\alpha i} = \frac{1}{8}\sum_{A}(\Omega_A)_{\alpha i}U_A(y)\chi(2y + a\hat{A}), \tag{B.27}$$

$$\bar{q}(y)_{\alpha i} = \frac{1}{8}\sum_{A}\bar{\chi}(2y + a\hat{A})U_A^\dagger(y)(\Omega_A)^\dagger_{i\alpha}. \tag{B.28}$$

The link variable $U_A(y)$ is the gluon on the lattice and carries the phase information from lattice site y to $y + aA$ while α and i label the Dirac and taste indices. Following the Symanzik improvement program, the staggered action including the dimension 5 Laplacian operator can be expressed by the $q(y)$ fields as

$$S_{\mathrm{KS}} = 16\sum_{y}\bar{q}(y)\left\{m(\mathbb{1}\otimes\mathbb{1}) + \sum_{\mu}[(\gamma_\mu\otimes\mathbb{1})\nabla_\mu + a(\gamma_5\otimes\xi_\mu\xi_5)\Delta_\mu]\right\}q(y). \tag{B.29}$$

The γ_μ describe the spin structure while $\xi_i = \gamma_i^*$ are gamma matrices that describe the taste structure. The derivatives ∇_μ and Δ_μ correspond to the first and second derivative operators operating on the doubled lattice. At this point, it is informative to point out that while Eq. (B.29) suggests that the staggered action has $\mathcal{O}(a)$ discretization errors, this not the case. The staggered action must possess the same discretization errors as the Naive action, which start at $\mathcal{O}(a^2)$, since the two actions differ only by a 'doubling'-symmetry transformation. However, the transformation from the one-component staggered action Eq. (B.24) to the doubled lattice Eq. (B.29) violates translational symmetry, and as a result of losing momentum conservation, the staggered action picks up the $\mathcal{O}(a)$ term to correct for this effect[45]. However, Eq. (B.29) illuminates the chiral symmetry properties of the staggered action. Note that Eq. (B.29) looks very similar to the Wilson action discussed previously. Assuming a four flavor/taste theory, by taking the continuum and massless limit, both the Wilson and staggered action are invariant under $\mathrm{U}(4) \otimes \mathrm{U}(4)$ symmetry. And similar to the Wilson action, chiral symmetry is also broken for the staggered action at non-zero mass. However, at non-zero lattice spacing, the $\mathcal{O}(a)$ term in the

Wilson action transforms like a mass term and therefore, chiral symmetry is completely lost. However, looking at Eq. (B.29), we see that the action is invariant under axial transformations,

$$q(y) \rightarrow e^{i\alpha(\gamma_5 \otimes \xi_5)} q(y), \tag{B.30}$$

$$\bar{q}(y) \rightarrow \bar{q}(y) e^{i\alpha(\gamma_5 \otimes \xi_5)}. \tag{B.31}$$

This nontrivial remnant of chiral symmetry manifests itself as a spontaneously broken symmetry in staggered QCD, generating Goldstone bosons in the massless limit. Therefore, γ_5-symmetry protects the mass terms from additive renormalizations. For non-zero mass, the Goldstone bosons pick up a mass-squared proportional to m as will be seen in the discussion of chiral perturbation theory.

The staggered Dirac operator may be written as,

$$D_{\mathrm{KS}} = \sum_\mu [(\gamma_\mu \otimes \mathbb{1})\nabla_\mu + a(\gamma_5 \otimes \xi_\mu \xi_5)\Delta_\mu] \tag{B.32}$$

$$= D \otimes \mathbb{1} + a\Delta, \tag{B.33}$$

$$M_{\mathrm{KS}} = D_{\mathrm{KS}} + m(\mathbb{1} \otimes \mathbb{1}), \tag{B.34}$$

where D is the naive Dirac operator. After rewriting the fermion action on the doubled lattice, we are however still left with four tastes. However, in the continuum limit, Eq. (B.34) suggests that the taste structure disappears and the Dirac operator is now again completely diagonalized. In light of this fact, the extra tastes in the sea are removed by the 'fourth-root' procedure. In the path integral, the fermion fields are integrated out such that,

$$\frac{1}{Z}\int [d\psi][d\bar{\psi}][dU] e^{-S_{\mathrm{gluons}} - S_{\mathrm{fermions}}} = \frac{1}{Z}\int [dU] \mathrm{Det}(\not{D} + M) e^{-S_{\mathrm{gluons}}}. \tag{B.35}$$

Rooting

Eq. B.29 show that up to dimension 4, the Dirac operator is diagonal in taste space. Therefore, in the continuum limit, replacing $\mathrm{Det} M_{\mathrm{KS}} \rightarrow \mathrm{Det}\,(M_{\mathrm{KS}})^{1/4}$ restricts the Dirac operator to a single taste. However, as suggested in Eq. (B.29), for non-zero lattice spacing, taste breaking effects enter and the validity of the fourth-root procedure becomes nontrivial. There is concern that the rooted staggered theory is not in the same universality class as continuum QCD. This is because the Goldstone Bosons of the rooted staggered theory has non-degenerate masses implying that the theory at non-zero lattice spacing is non-local.[18] However, for non-zero quark masses, in the continuum limit, the non-local contributions disappear, indicating that the rooted staggered theory is in the same universality class as QCD given that the chiral limit is never taken. Currently, all published criticisms[27][26][28] of the fourth root procedure have been refuted[19][20] and there is a significant amount of circumstantial evidence[33][41][58] that supports the validity of this procedure.

B.2.1 Improved staggered action

While the scaling violations of the staggered action start at $\mathcal{O}(a^2)$, the errors introduced at this level are very large compared to $\mathcal{O}(a^2)$ errors of other lattice actions. The $\mathcal{O}(a^2)$ errors originate from the action as well as taste-mixing violations mediated by an ultraviolet gluon.

The Naik term improves the action at tree-level and is added to the action by improving the finite difference operator through $\mathcal{O}(a^2)$,

$$\nabla \cdot \gamma \to \left[\nabla_\mu - \frac{a^2}{6}\left(\nabla_\mu\right)^3\right]\gamma^\mu, \tag{B.36}$$

yielding

$$S_{\text{Naik}} = \sum_x \bar{\chi}(x)\left(-\frac{a^2}{6}\gamma\cdot\nabla^3\right)\chi(x). \tag{B.37}$$

Taste-changing processes occur through exchange of high momentum gluons. Therefore, it is possible to suppress taste-changing effects by adding a 4-quark operator since the gluons are highly virtual. However, a simpler modification is to suppress the high momentum gluons. The suppression is realized by imposing an ultraviolet cutoff on the link fields,

$$V_\mu(x) = \Pi_{\rho\neq\mu}\left(1 + \frac{a^2\nabla_\rho^2}{4}\right)U_\mu(x), \tag{B.38}$$

where the smearing function may be suggestively written as

$$1 + \frac{1}{4}a^2\nabla_\rho^2 \to 1 - \frac{1}{4}a^2p^2 \approx e^{-\frac{a^2p^2}{4}}. \tag{B.39}$$

On the lattice, the smearing makes the links fatter, and therefore, the smearing used in the asqtad action is called a fat7 smearing. The exact form of the fat7 smearing is detailed in Ref. [10]. The smearing however, introduces a new $\mathcal{O}(a^2)$ term which is canceled by the Lepage term[10], and is needed to preserve the $\mathcal{O}(a^2)$ improvement provided by the Naik term.

Combining the improvement on the action (Naik term), and the suppression of taste-mixing violations, the asqtad action is improved through $\mathcal{O}(a^2)$ and have errors starting at $\mathcal{O}(\alpha_s a^2)$ and $\mathcal{O}(a^4)$. As the name suggests, the links are also tadpole improved, as discussed in Appendix A.1.

Appendix C

Chiral perturbation theory

While lattice QCD currently provides a rigorous first principle description of the strong interaction, knowledge and insights from effective theories provide invaluable information in practice. Due to the expense of simulating at physical fermion masses, for this project the lightest pion is simulated at approximately 170MeV, while the physical pion mass lies at 135MeV; therefore matrix elements simulated on nearly-physical ensembles need to be extrapolated to describe pions with physical masses. Such a process is guided by a chiral effective theory. Unlike pre-QCD descriptions, chiral perturbation theory is formulated with the understanding of the symmetries of the QCD Lagrangian; this allows for order-by-order systematic improvements on the effective theory, a characteristic absent in pre-QCD models. Therefore, essential symmetries of the QCD Lagrangian will be covered below.

C.1 Symmetries of the QCD Lagrangian

The QCD Lagrangian is invariant under $\mathrm{U}(n)_\mathrm{F}$ flavor symmetry in the limit of zero quark masses. Flavor symmetry may be rewritten in the chiral form as $\mathrm{U}(n)_\mathrm{L} \times \mathrm{U}(n)_\mathrm{R}$. Furthermore, $\mathrm{U}(n)$ is isomorphic to $\mathrm{SU}(n) \times \mathrm{U}(1)$. It is therefore customary to say that the QCD Lagrangian is invariant under

$$\mathrm{SU}(n)_\mathrm{L} \times \mathrm{SU}(n)_\mathrm{R} \times \mathrm{U}(1)_\mathrm{L} \times \mathrm{U}(1)_\mathrm{R}. \tag{C.1}$$

However, the symmetry of the Lagrangian is believed to be spontaneously broken. A sufficient condition which indicates that spontaneous symmetry breaking occurs in QCD is to show that the scalar quark condensate at the chiral (zero quark mass) limit is non-vanishing. The following argument is outlined in Ref. [56]. In order to show that the scalar quark condensate is non-vanishing, let us first define the scalar and pseudoscalar Noether currents,

$$S_a(y) = \bar{q}(y)\lambda_a q(y) \qquad \text{for } a = \{0, \ldots, 8\} \tag{C.2}$$

$$P_a(y) = i\bar{q}(y)\gamma_5\lambda_a q(y) \qquad \text{for } a = \{0, \ldots, 8\} \tag{C.3}$$

where without loss of generality, $\lambda_a/2$ for $a = \{1, \ldots, 8\}$ are the generators of SU(3) and $\lambda_0/2$ is the identity corresponding to the phase. Together all 9 generators form the generators of U(3). The vector and axial-vector charge is therefore defined as

$$Q_V^a(t) = \int d^3x q^\dagger(\vec{x},t)\frac{\lambda^a}{2}q(\vec{x},t), \tag{C.4}$$

$$Q_A^a(t) = \int d^3x q^\dagger(\vec{x},t)\gamma_5\frac{\lambda^a}{2}q(\vec{x},t). \tag{C.5}$$

From the SU(3) Lie bracket, we can define the following commutation relation for the octet and singlet,

$$\left[\frac{\lambda_a}{2}, \gamma_0\lambda_b\right] = \gamma_0 i f_{abc}\lambda_c \qquad \text{for } a,b = 1,\ldots,8, \tag{C.6}$$

$$\left[\frac{\lambda_a}{2}, \gamma_0\lambda_0\right] = 0 \qquad \text{for } a = 1,\ldots,8, \tag{C.7}$$

where f_{abc} are the structure constants. From the Dirac matrix algebra, we can define the following commutation relation,

$$(i)^2\left[\gamma_5\frac{\lambda_a}{2}, \gamma_0\gamma_5\lambda_a\right] = \lambda_a^2\gamma_0. \tag{C.8}$$

Let us first consider the vector charge Q_V. Applying the commutation relations from Eq. (C.6) on to Eq. (C.4) yields the following relationship,

$$[Q_V^a(t), S_b(y)] = i\sum_{c=1}^{8} f_{abc}S_c(y) \qquad \text{for } a,b = 1,\ldots,8, \tag{C.9}$$

$$[Q_V^a(t), S_0(y)] = 0 \qquad \text{for } a = 1,\ldots,8. \tag{C.10}$$

We have only worked out the case for which the charges transform under the octet representation because it is well know that the commutation relations for the singlet has an anomaly, which will introduce unnecessary complications for this discussion. Let us first take a look at the octet components for the charge density described by Eq. (C.9). Using the following relationship,

$$\sum_{a,b=1}^{8} f_{abc}f_{abd} = 3\delta_{cd}, \tag{C.11}$$

the octet scalar quark density may be derived from Eq. (C.9) giving

$$S_a(y) = -\frac{i}{3}\sum_{b,c=1}^{8} f_{abc}\left[Q_V^b(t), S_c(y)\right]. \tag{C.12}$$

In the chiral limit, the ground state is invariant under SU(3)$_V$, therefore the vector charge of the ground state vanishes $Q_V^a\left|0\right\rangle = 0$. As a result,

$$\langle 0\left|S_a(y)\right|0\rangle = 0. \tag{C.13}$$

We may conclude then, that octet component of the scalar quark condensate vanishes in the chiral limit. We may further derive the following relationships,

$$\langle S_3 \rangle = \left\langle \bar{q} \begin{pmatrix} 1 & 0 & 0 \\ 0 & -1 & 0 \\ 0 & 0 & 0 \end{pmatrix} q \right\rangle = \langle \bar{u}u \rangle - \langle \bar{d}d \rangle \,, \tag{C.14}$$

$$\langle S_8 \rangle = \left\langle \bar{q} \sqrt{\frac{1}{3}} \begin{pmatrix} 1 & 0 & 0 \\ 0 & 1 & 0 \\ 0 & 0 & -2 \end{pmatrix} q \right\rangle = \sqrt{\frac{1}{3}} \left(\langle \bar{u}u \rangle + \langle \bar{d}d \rangle - 2 \langle \bar{s}s \rangle \right) . \tag{C.15}$$

From here we get see that,

$$\langle \bar{u}u \rangle = \langle \bar{d}d \rangle \,, \tag{C.16}$$

$$\therefore \langle \bar{u}u \rangle = \langle \bar{d}d \rangle = \langle \bar{s}s \rangle \,. \tag{C.17}$$

Eq. (C.10) suggests that the singlet component of the scalar quark density commutes with the vector charge. Therefore, unlike the octet component of the scalar quark density, we are unable to show that that the singlet component vanishes. In fact, let us assume that the singlet scalar quark density does not vanish,

$$\langle \bar{q}q \rangle = \langle \bar{u}u \rangle + \langle \bar{d}d \rangle + \langle \bar{s}s \rangle \neq 0. \tag{C.18}$$

Let us next, look at the relationship between the axial-vector charge and the pseudoscalar quark density. By applying Eq. (C.8) to Eq. (C.3, C.5) and using $\langle \bar{u}u \rangle = \langle \bar{d}d \rangle = \langle \bar{s}s \rangle$ we get the following commutation relation,

$$i \left[Q_A^a(t), P_a(y) \right] = \frac{2}{3} \bar{q}q. \tag{C.19}$$

Evaluating this commutation on the ground state relates the axial-vector charge to the scalar chiral quark condensate as follows,

$$\langle 0 \left| i \left[Q_A^a(t), P_a(y) \right] \right| 0 \rangle = \frac{2}{3} \langle \bar{q}q \rangle \qquad \text{for } a = 1, \ldots, 8. \tag{C.20}$$

Rewriting the charge as the axial-vector current, and inserting a complete set of intermediate states $\phi^a(p)$, Eq. (C.20) describes the pion coupling to the axial-vector current. The matrix element is parametrized by the pion decay constant,

$$\left\langle 0 \left| A_\mu^a(0) \right| \phi^b(p) \right\rangle = i p_\mu f_\pi \delta^{ab}. \tag{C.21}$$

Therefore, in order to be certain that QCD exhibits spontaneous symmetry breaking, it is sufficient to show that the singlet chiral quark condensate is non-zero, or equivalently show that the pion decay constant does no vanish. Currently, there are numerous lattice calculations which show that the chiral quark condensate [51][61][37] is non-vanishing. Lattice determinations of the pion and kaon decay constants f_π, f_K [9][31][40] also agree with experiment. Therefore, it is safe to say that chiral perturbation theory accurately describes a theory of pions, and is in fact, an effective theory which respects the symmetry of the QCD ground state. In fact, the symmetry of the QCD ground state may be understood by motivating Goldstone's theorem. As a reminder, the QCD Lagrangian yields left- and right-handed conserved currents under the variation of the corresponding fields. The resulting charges form the following Lie algebra,

$$\left[Q_L^a, Q_L^b\right] = i f_{abc} Q_L^c, \tag{C.22}$$

$$\left[Q_R^a, Q_R^b\right] = i f_{abc} Q_R^c. \tag{C.23}$$

The vector and axial-vector charges are defined as

$$Q_V^a = Q_R^a + Q_L^a, \tag{C.24}$$

$$Q_A^a = Q_R^a - Q_L^a, \tag{C.25}$$

and form the following Lie algebra,

$$\left[Q_V^a, Q_V^b\right] = i f_{abc} Q_V^c, \tag{C.26}$$

$$\left[Q_A^a, Q_A^b\right] = i f_{abc} Q_V^c. \tag{C.27}$$

Here we see that while the vector charges form a closed Lie algebra, the axial-vector charges form a nonlinear Lie algebra. Goldstone's theorem states that generators of non-linearly realized symmetries excite massless bosons out of the asymmetric vacuum. Therefore, given a non-vanishing chiral condensate and the non-linearity of the axial-vector charges, the symmetry of the ground state of QCD is spontaneously broken from $\mathrm{U(3)_F}$ to $\mathrm{SU(3)}_V \times \mathrm{U(1)}_V$ with the $\mathrm{U(1)}_A$ symmetry separately broken by the chiral anomaly.

C.2 Low energy effective field theory

Equipped with the understanding of the symmetries of QCD, the low-energy effective Lagrangian must be symmetric under $\mathrm{SU(3)_L} \times \mathrm{SU(3)_R} \times \mathrm{U(1)}_V$ transformations, while having eight pseudoscalar degrees of freedom generated from $\mathrm{SU(3)}_A$ symmetry breaking. The variables of the effective field theory is commonly packaged as the following,

$$\Sigma(x) = \exp\left(i\frac{\phi(x)}{f_\pi}\right), \tag{C.28}$$

$$\phi(x) = \sum_{a=1}^{8} \lambda_a \phi_a(x) = \begin{pmatrix} \pi^0 + \frac{1}{\sqrt{3}}\eta & \sqrt{2}\pi^+ & \sqrt{2}K^+ \\ \sqrt{2}\pi^- & -\pi^0 + \frac{1}{\sqrt{3}}\eta & \sqrt{2}K^0 \\ \sqrt{2}K^- & \sqrt{2}\bar{K}^0 & -\frac{2}{\sqrt{3}}\eta \end{pmatrix}. \tag{C.29}$$

Under global $\mathrm{SU}(3)_\mathrm{L} \times \mathrm{SU}(3)_\mathrm{R}$ transformations, the field Σ transforms as,

$$\Sigma \to U_\mathrm{R} \Sigma U_\mathrm{L}^\dagger \tag{C.30}$$

where $U_{\mathrm{L/R}} \in \mathrm{SU}(3)_{\mathrm{L/R}}$. To construct the Lagrangian, we motivate Weinberg's power counting scheme and expand in orders of momentum and quark mass. Since this is a low-energy theory, momenta enter in as factors of p/Λ_χ where $\Lambda_\chi \sim 1\mathrm{GeV}$ is the scale at which chiral perturbation theory is believed to break down. On-shell meson masses enter in as factors of $p^2 = M_\pi^2 \propto m_q$, hence enter as momentum squared terms to the Lagrangian. Finally, since the Lorentz index always contracts with either the metric tensor $g^{\mu\nu}$ or the Levi-Civita symbol $\epsilon^{\mu\nu\rho\sigma}$, only even powers of momenta are expected in the effective Lagrangian. Therefore, at lowest order, the chiral Lagrangian is

$$\mathcal{L}_\mathrm{eff} = \frac{f_\pi^2}{8} \mathrm{Tr}\left(\partial_\mu \Sigma \partial_\mu \Sigma^\dagger\right) \tag{C.31}$$

where f_π is the pion decay constant, and is a free parameter in the effective theory.

Away from the chiral limit, explicit symmetry breaking is observed in QCD, and is introduced into the chiral effective theory as the following term,

$$\mathcal{L}_\mathrm{s.b.} = \frac{f_\pi^2 B_0}{4} \mathrm{Tr}\left(M\Sigma^\dagger + \Sigma M^\dagger\right), \tag{C.32}$$

where $M = \mathrm{diag}(m_u, m_d, m_s)$ and $3f_\pi^2 B_0 = -\langle \bar{q}q \rangle$ is a free parameter related to the chiral condensate. Let us expand

$$\Sigma = 1 + i\frac{\lambda_a \phi_a}{f_\pi} - \frac{1}{2}\frac{\left(\lambda_a \phi_a\right)^2}{f_\pi^2} + \ldots. \tag{C.33}$$

Then to lowest order (ignoring the constant term under variations of the Lagrangian), taking into account that $M = M^\dagger$ and $\mathrm{Tr}(\phi) = \mathrm{Tr}(\phi^\dagger)$,

$$\mathcal{L}_\mathrm{s.b.} = -\frac{B_0}{2} \mathrm{Tr}\left(\phi^2 M\right). \tag{C.34}$$

Taking the isospin symmetric limit $m_u = m_d = m_l$, the trace of Eq. (C.34) yields,

$$\mathrm{Tr}\left(\phi^2 M\right) = \frac{1}{2}M_\pi^2\left(3\pi^2\right) + \frac{1}{2}M_K^2\left(4K^2\right) + \frac{1}{2}M_\eta^2 \eta^2, \tag{C.35}$$

where

$$M_\pi^2 = 2B_0 m_l, \tag{C.36}$$

$$M_K^2 = B_0(m_l + m_s), \tag{C.37}$$

$$M_\eta^2 = \frac{2}{3}B_0(m_l + 2m_s), \tag{C.38}$$

demonstrating the earlier claim that the quark masses are proportional to the square of the meson masses. Having at our disposal, a description of the physics of pions as a function of the pion mass allows us to leverage this knowledge, and extrapolate matrix elements extracted at heavier than physical pion masses to the physical point.

The leading order effective Lagrangian for continuum chiral perturbation theory is given by Eq. (C.31, C.32),

$$\mathcal{L}_{\text{cont. LO}} = \frac{f_\pi^2}{8}\mathrm{Tr}\left(\partial_\mu \Sigma \partial_\mu \Sigma^\dagger\right) + \frac{f_\pi^2 B_0}{4}\mathrm{Tr}\left(M\Sigma^\dagger + \Sigma M^\dagger\right). \tag{C.39}$$

C.2.1 Rooted staggered chiral perturbation theory

Under the formulation of staggered fermions, as detailed in Appendix B.2, taste degrees of freedom are reduced but not eliminated. As a result, for $N_f = 3$ the Lagrangian is invariant under SU(12) describing 3 flavors times 4 tastes. The taste interactions are generated by ultraviolet gluons with momentum near π/a. The discrete taste transformations are generated by $\xi_\mu = \gamma_\mu^*$. The leading order Lagrangian for staggered chiral perturbation theory is similar to Eq. (C.39) with the field Σ expanded to include the tastes. The quark fields under staggered chiral perturbation theory are

$$q_i \to \xi_\mu q_i \tag{C.40}$$

yielding the 12×12 field Φ analogous to Eq. (C.29). At $\mathcal{O}(a^2)$, the dimension 6 operators that contribute to the Lagrangian may be described by a set of 4-quark operators since the UV gluons can be integrated out. A systematic derivation of the exhaustive set of 4-quark operators for the one flavor theory is given in detail in Ref. [42] and are derived by understanding the symmetries of fermion bilinears in the continuum and on the lattice. For the three-flavor theory we take the direct sum of the taste structures and define the matrix,

$$\xi_\mu^{(3)} = \begin{pmatrix} \xi_\mu & 0 & 0 \\ 0 & \xi_\mu & 0 \\ 0 & 0 & \xi_\mu \end{pmatrix}. \tag{C.41}$$

Including the $\mathcal{O}(a^2)$ terms, the staggered chiral Lagrangian is,

$$\mathcal{L}_{\text{stag.}} = \mathcal{L}_{\text{cont. LO}} + a^2\mathcal{V} \tag{C.42}$$

$$\begin{aligned}
\mathcal{V} =& C_1 \mathrm{Tr}(\xi_5^{(3)}\Sigma\xi_5^{(3)}\Sigma^\dagger) + C_3\frac{1}{2}\sum_\nu \left[\mathrm{Tr}(\xi_\nu^{(3)}\Sigma\xi_\nu^{(3)}\Sigma) + \text{h.c.}\right] \\
&+ \frac{1}{2}C_4\sum_\nu \left[\mathrm{Tr}(i\xi_{\nu 5}^{(3)}\Sigma i\xi_{\nu 5}^{(3)}\Sigma) + \text{h.c.}\right] + C_6\sum_{\mu<\nu}\mathrm{Tr}(\xi_{\mu\nu}^{(3)}\Sigma\xi_{\mu\nu}^{(3)}\Sigma^\dagger) \\
&+ \frac{1}{4}C_{2V}\sum_\nu \left[\mathrm{Tr}(\xi_\nu^{(3)}\Sigma)\mathrm{Tr}(\xi_\nu^{(3)}\Sigma) + \text{h.c.}\right] \\
&+ \frac{1}{4}C_{2A}\sum_\nu \left[\mathrm{Tr}(\xi_{5\nu}^{(3)}\Sigma)\mathrm{Tr}(\xi_{\nu 5}^{(3)}\Sigma) + \text{h.c.}\right] \\
&+ \frac{1}{2}C_{5V}\sum_\nu \mathrm{Tr}(\xi_\nu^{(3)}\Sigma)\mathrm{tr}(\xi_\nu^{(3)}\Sigma^\dagger) + \frac{1}{2}C_{5A}\sum_\nu \mathrm{Tr}(\xi_{5\nu}^{(3)}\Sigma)\mathrm{Tr}(\xi_{\nu 5}^{(3)}\Sigma^\dagger),
\end{aligned} \tag{C.43}$$

where $\xi_{5\nu} \equiv \xi_5\xi_\nu$ and $\xi_{\mu\nu} = (1/2)[\xi_\mu, \xi_\nu]$.

The pion fields $\Sigma = \exp(i\phi/f_\pi)$ can be expanded in terms of the 16 taste generators,

$$\phi_{ij} = \frac{1}{2}\sum_{F=1}^{16}\Xi_F\phi_{ij}^F, \qquad \text{where } i,j = u,d,s \tag{C.44}$$

$$\Xi_F \in \{\xi_5, i\xi_{5\mu}, i\xi_{\mu\nu}, \xi_\mu, \mathbb{1}\}\,. \tag{C.45}$$

With the extra taste degrees of freedom, the meson masses may be obtained by repeating the calculation detailed in Eq. (C.32) through Eq. (C.38) while taking into account the $\mathcal{O}(a^2)$ taste violations outlines in $\mathcal{L}_{\text{stag.}}$. The pion masses are,

$$m_{Fij}^2 = B_0(m_i + m_j) + a^2\Delta(\Xi_F), \qquad \text{where } i,j = u,d,s \text{ and } i \neq j \tag{C.46}$$

while the taste splittings are

$$\Delta(\xi_5) = 0, \tag{C.47}$$

$$\Delta(i\xi_{5\mu}) = \frac{16}{f_\pi^2}(C_1 + 3C_3 + C_4 + 3C_6), \tag{C.48}$$

$$\Delta(i\xi_{\mu\nu}) = \frac{16}{f_\pi^2}(2C_3 + 2C_4 + 4C_6), \tag{C.49}$$

$$\Delta(\xi_\mu) = \frac{16}{f_\pi^2}(C_1 + C_3 + 3C_4 + 3C_6), \tag{C.50}$$

$$\Delta(\mathbb{1}) = \frac{16}{f_\pi^2}(4C_3 + 4C_4). \tag{C.51}$$

The pseudoscalar taste receives no taste splitting contribution and is protected to all orders in chiral perturbation theory by the remnant axial-symmetry discussed in Appendix B.2. The numerical values for the taste splittings are obtained through global fits on to the MILC asqtad data on the squared-masses of the pions as a function of light quark mass[4]. The taste splittings organize into 5 different groups with the degeneracy protected by SO(4), the symmetry of the contributing 4-quark terms at $\mathcal{O}(a^2)$.

C.2.2 Taste symmetries of staggered chiral effective theory

The symmetries of staggered chiral effective theory is better understood by taking a step back and understanding the terms which explicitly enter into the $\mathcal{O}(a^2)$ contributions in the Lagrangian. This section summarizes the ideas laid out in Ref. [42], I will focus on the contributions of the 4-quark terms at dimension 6 only however. For simplicity, we will work with an SU(4) theory with one flavor and 15 tastes. In the continuum limit, one would expect that the effective chiral Lagrangian retain the full SU(4) symmetry as all the taste contributions disappear. However this symmetry is broken into the subgroup SO(4) at $\mathcal{O}(a^2)$ and further broken down to Γ_4 at $\mathcal{O}(a^4)$. To understand this mechanism, let us consider the 4-quark contributions to the Lagrangian. In general the 4-quark terms have the form

$$S_6^{\text{4-quark}} = \bar{Q}(\Gamma \otimes \Xi_F)q(y)\bar{Q}(y)(\Gamma \otimes \Xi_F)q(y) \tag{C.52}$$

where Γ and Ξ separately act on spin and taste space. The 4-quark terms may be split into two subgroups, S_6^{nomix} and S_6^{mix} where the Lorentz indices are either separately summed between the spin and taste spaces or form correlated bilinears. For example, for the 4-quark term with a tensor spin structure and vector taste structure, the 4-quark contributions are,

$$S_6^{\text{nomix}} =\bar{Q}(\gamma_\mu\gamma_\nu \otimes \xi_\rho)q(y)\bar{Q}(y)(\gamma_\mu\gamma_\nu \otimes \xi_\rho)q(y), \tag{C.53}$$

$$S_6^{\text{mix}} \approx\bar{Q}(\gamma_\mu\gamma_\nu \otimes \xi_\mu)q(y)\bar{Q}(y)(\gamma_\mu\gamma_\nu \otimes \xi_\mu)q(y). \tag{C.54}$$

For dimension 6 contributions of form S_6^{nomix}, the contribution is invariant under the transformations

$$Q \to (\mathbb{1} \otimes \xi_\mu)Q, \qquad \bar{Q} \to \bar{Q}(\mathbb{1} \otimes \xi_\mu), \tag{C.55}$$

where xi_μ are the generators of the Γ_4 Clifford algebra in taste space suggesting that S_6^{nomix} is invariant under Γ_4 transformations. However, since S_6^{nomix} is Lorentz invariant and the quark fields transform as Lorentz vectors, these terms are invariant under the larger SO(4) taste group. In fact, given the Clifford algebra

$$\{\gamma_\mu, \gamma_\nu\} = 2\delta_{\mu\nu}, \tag{C.56}$$

we may construct a representation of SO(4)

$$M_{\mu\nu} = \frac{1}{4i}[\gamma_\mu, \gamma_\nu]. \tag{C.57}$$

It then follows explicitly that S_6^{nomix} is invariant under SO(4) transformations. Taste SO(4) symmetry protects the tastes degeneracies within the five Ξ elements, yielding degenerate multiplicities of 1,4,6,4,1 respectively. The set of operators in S_6^{nomix} match to the terms in Eq. (C.43), completely describing all 4-quark terms that enter at $\mathcal{O}(a^2)$. Therefore, at this order, the Lagrangian breaks SU(4) but preserves SO(4) taste symmetry.

On the other hand, the S_6^{mix} terms are only invariant under the hypercubic subgroup of SO(4) which acts simultaneously on spin and taste as seen by the four repeated Lorentz indices in Eq. (C.54). As a result taste symmetry is broken down to Γ_4 lifting all degeneracies in taste space.

C.2.3 Partially quenched chiral perturbation theory

In order to leverage the limited computing resources that are available, much of the dataset used for this project involve partially-quenched ensembles. In our 2+1 ensembles, this means that the light sea and valence quark masses m_l are different. This allows ensembles with different valence masses (cheap) to be generated on the same gauge configurations (expensive), cheaply yielding higher statistics. For heavy quarks, the Fermilab interpretation of the Wilson action is used to simulate the heavy valence quark on top of the staggered action sea quarks. In this case, mixed action QCD is used, and the corresponding mixed action chiral perturbation theory is needed in order to leverage data generated in this manner. While partial quenching and mixed action QCD is not a well defined quantum theory (violates unitarity), the validity of the mixed action theory hinges on the fact that while working in the region where the chiral expansion is valid (small quark masses), the effective theory gains predictive power once the LECs of the theory are determined. Since the LECs are independent of quark masses, we may use a mixed action description to first determine what the LECs are, and then extrapolate to the physical point by following the full QCD trajectory.

C.2.4 Heavy quark effective theory

Before a discussion on heavy meson chiral perturbation theory, I will first discuss heavy quark effective theory as HMχPT is a marriage between HQET and χPT following Schwartz. Taking a step back, let us first discuss heavy quark physics, as HQET is an effective field theory of QCD useful for describing heavy quark physics of heavy-light systems.

Taking a look at the D- and B-mesons, we can draw similarities between these heavy-light systems and the hydrogen atom. At leading order, we describe the hydrogen atom with a proton supplying a static coulomb source dressed with an electron cloud. Analogously, for heavy-light systems, in the $m_Q \to \infty$ limit, the heavy quark is treated as a static color (gluon) source dressed with a pion cloud. The hydrogen atom forms S-wave and P-wave orbitals corresponding to a singlet and triplet state, which at leading order are degenerate. The heavy-light system similarly forms a singlet D and triplet D^* state as a result of the tensor product two spin 1/2 wavefunctions. At leading order in HQET, the two states are also degenerate, thus recovering heavy-quark spin symmetry. For the hydrogen atom, at $\mathrm{O}(E/m_p)$ where E is the binding energy, and m_p is the proton mass, the degeneracy is lifted with the spin-spin interaction, resulting in the hyperfine splitting. Similarly, in HQET, at $\mathrm{O}(\Lambda_{\mathrm{QCD}}/m_Q)$, the degeneracy is also lifted, thus defining the hyperfine splitting Δ^* as defined in the chiral fit function. However, the similarities end, since the heavy-light system is in a bound state, the pion cloud carries energy of order Λ_{QCD}, and therefore is strongly interaction; unlike the hydrogen atom, we can not model the pions using Schrödinger's equation.

At leading order, we take the $m_Q \to \infty$ limit, therefore HQET at leading order is identical for the B and D systems; and is where we recover heavy-quark flavor symmetry. At large m_Q, we can rewrite the four-momentum as

$$p^\mu = m_Q v^\mu + k^\mu \tag{C.58}$$

where v is the normalized velocity of the heavy quark such that $v^2 = 1$. Since we are working in the soft pion limit, the scales are again $m_Q \gg \Lambda_{\mathrm{QCD}}$, while changes in the momentum $k^\mu \sim \Lambda_{\mathrm{QCD}}$. Therefore, at leading order, v is a constant since there is not enough energy to change the direction of v. Since v is a constant, in HQET, v is a good choice as a conserved quantum number, as will be seen later.

Usually, we work with states which are relativistically normalized such that

$$\langle D(p')|D(p)\rangle = 2p^0(2\pi)^3\delta(p-p'). \tag{C.59}$$

However, in the heavy-quark limit $m_Q \to \infty$, therefore $p^0 \to \infty$. Therefore, in HQET we non-relativistically normalize our states. We define the HQET normalization condition as

$$\langle D(p)|D(p')\rangle_{\mathrm{NR}} = (2\pi)^3\delta(p-p'), \tag{C.60}$$

consistent with how we normalize the matrix elements of this project.

Given a heavy-light wavefunction, we can factorize it in the following way

$$|D\rangle = |c; v s_Q\rangle\, |\mathrm{muck}; v s_q\rangle \tag{C.61}$$

where the heavy quark has quantum numbers of velocity and heavy quark spin, while the pion cloud has quantum numbers of the heavy quark velocity and light quark spin. If we then compute currents using this factorized wavefunction, then in general for a heavy-heavy current, we get

$$\langle D\,|\bar{c}\Gamma c|\,D\rangle = \langle c; v' s_Q\,|\bar{c}\Gamma c|\,c; v s_Q\rangle \left\langle \text{muck}; v' s'_Q|\text{muck}; v s_Q\right\rangle \tag{C.62}$$

$$\equiv \langle c; v' s_Q\,|\bar{c}\Gamma c|\,c; v s_Q\rangle\, \xi(v, v') \tag{C.63}$$

where the dependence on v and v' can only be $\omega = v_\mu v'^\mu$ due to Lorentz invariance. The function $\xi(\omega)$ is the Isgur-Wise function and captures the physics of the pion cloud. At the limit of zero-recoil $\omega = 1$, in the heavy quark limit $m_Q \to \infty$, $\xi(1) = 1$. Deviations from unity at zero-recoil receives contributions perturbatively if the initial and final states are different, resulting in corrections of order $\alpha_s(m_b) - \alpha_s(m_c)$. Non-perturbative corrections to the Isgur-Wise function come in at order Λ_{QCD}/m_Q and are studied through lattice techniques.

To derive the leading order HQET Lagrangian, let us again refer back to the parametrization of the four-momentum $p^\mu = m_Q v^\mu + k^\mu$. Taking the $k^\mu = 0$ limit, the momentum space Dirac equation becomes,

$$\not{p}\psi = m_Q\psi \tag{C.64}$$

$$\to (1 - \not{v})\psi = 0 \tag{C.65}$$

We can split the field into a large component, and a small component as a result,

$$\psi(x) \equiv \psi_v(x) + \tilde{\psi}_v(x) \tag{C.66}$$

where $\psi_v(x) = \frac{1+\not{v}}{2}\psi(x)$ and $\tilde{\psi}_v(x) = \frac{1-\not{v}}{2}\psi(x)$. Here we see explicitly that the velocity v is promoted to a quantum number. Substituting in the Dirac equation, $\psi(x) = \psi_v(x)$ when $k^\mu = 0$ therefore $\psi_v(x)$ is the large component, and $\tilde{\psi}_v(x)$ is the small component which will only appear in the Lagrangian at higher order. Writing the wavefunction in the non-relativistic limit with spinor fields, we get

$$\psi = e^{-im_Q v\cdot x}\frac{1+\not{v}}{2}Q_v(x) \tag{C.67}$$

where the exponential factor is analogous to a non-relativistic plane wave at rest which is e^{-imt}. We can substitute ψ in to the QCD Lagrangian to get

$$\bar{\psi}(i\not{D} - m_Q)\psi = i\bar{Q}_v v\cdot D\frac{1+\not{v}}{2}Q_v. \tag{C.68}$$

We see that at leading order the heavy quark Lagrangian is independent of m_Q as protected by heavy-quark flavor symmetry. The full HQET Lagrangian at leading order includes light quarks and the gluon kinetic term yielding

$$\mathcal{L}_{\mathrm{HQET}} = -\frac{1}{4}(F^a_{\mu\nu})^2 + \bar{q}(i\not{D} - m_q)q \tag{C.69}$$

$$+\sum_v i\bar{Q}_v v\cdot D\frac{1+\not{v}}{2}Q_v + \mathrm{O}\left(\frac{1}{m_Q}\right). \tag{C.70}$$

The sum over v suggests that heavy quarks in momentum space live in separate boxes located at $m_Q v^\mu \gg \Lambda_{\mathrm{QCD}}$ with box sizes of $k^\mu \sim \Lambda_{\mathrm{QCD}}$.

C.2.5 Heavy meson chiral perturbation theory

So far, we have discussed the effective theory of pions, however our goal is to describe interactions of heavy-light mesons (namely the D^0) with pions. To accomplish this task, we will now introduce heavy meson degrees of freedom into the chiral perturbation theory through the formulation of heavy quark effective theory (HQET). A complete discussion of heavy quark physics may be found in Ref. [49], while the following sections discusses key concepts of this theory.

A heavy-light meson composed of a $Q\bar{q}$ pair incorporates physics at length scales $m_q \ll \Lambda_{\mathrm{QCD}}$ and $m_Q \gg \Lambda_{\mathrm{QCD}}$, while the typical interaction energy of nonperturbative QCD dynamics is of order Λ_{QCD}. In the limit of $m_q \to 0$, we recover the chiral limit $\mathrm{SU(3)_L}\otimes\mathrm{SU(3)_R}$. On the other hand, we may take the limit $m_Q \to \infty$. In this limit, nonperturbative interactions do not change the velocity of the heavy quark, and the heavy quark behaves like a static source that transforms as a color triplet. Therefore, the mass of the heavy quark at leading order is irrelevant, leading to heavy quark flavor symmetry. Since the heavy quark only behaves as a color source, interactions must also be independent of spin, leading to heavy quark spin symmetry. In particular, one may rotate the heavy-light meson from the spin singlet to the spin triplet state for free in the $m_Q \to \infty$ limit. Combining the SU(2) spin symmetry with U(N) heavy flavor symmetry, the Lagrangian must be constructed to be symmetric under U($2N$) transformations where N is the number of heavy flavors.

Due to heavy quark spin symmetry, we construct the heavy-light field $H_v^{(Q)}$ to incorporate both the pseudoscalar and vector mesons. Given a pseudoscalar field $P_v^{(Q)}$ and vector field $P_{v\mu}^{*(Q)}$, the heavy-light field is defined as,

$$H_v^{(Q)} = \frac{1+\not{v}}{2}\left[\not{P}_v^{*(Q)} + iP_v^{(Q)}\gamma_5\right], \tag{C.71}$$

and the conjugate field,

$$\bar{H}_v^{(Q)} = \left[\not{P}_v^{*} + i\gamma_5 P_v^{(Q)}\right]\frac{1+\not{v}}{2}, \tag{C.72}$$

where P transforms as a pseudoscalar, P^* transforms as a vector, while the factor $(1+\not{v})/2$ projects out the particle components of the four-component spinor in the heavy-quark rest frame. Specifically, in the heavy-quark rest frame

$(1+\not{v})/2 \to (1+\gamma_0)/2$. In HQET, the particle and anti-particles are treated as separate fields since the effective theory is only viable at scales much smaller than Λ_{QCD}, while interactions which mix particle with anti-particles occur at the Λ_{QCD} scale.

For a single flavor heavy quark, the heavy-light field transforms as a doublet under $S \in \mathrm{SU}(2)$ heavy quark spin symmetry,

$$H \to SH, \tag{C.73}$$

$$\bar{H} \to \bar{H}S^\dagger. \tag{C.74}$$

while under chiral $\mathrm{SU}(n)$ symmetry, where n is the number of light quark flavors, the heavy-light fields transform as

$$H \to HU^\dagger, \tag{C.75}$$

$$\bar{H} \to U\bar{H}, \tag{C.76}$$

where for staggered fermions, the symmetry again expands to $U \in \mathrm{SU}(4n)$ to incorporate the taste fermions.

0

Appendix D

Correlator Fit Functions

The correlator fit functions may be derived by using the path integral formulation. Both the two- and three-point fit functions will be derived to order $\exp(-ET)$; these terms describe the wrap around terms from the periodic boundary conditions.

D.1 Two-point fit function

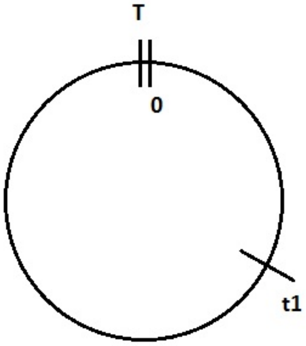

Figure D.1: Two-point source and sink locations for lattice of length T.

For the two-point functions, the source is set to $t_{\text{source}} = 0$ while the sink is placed at $t_{\text{sink}} = t_1$. Fig. D.1 shows where the source, sink and periodic boundary condition source are located. The source and sink operators are connected by the transfer matrix.

$$C^{2pt} = \frac{\mathrm{Tr}\chi^\dagger e^{-\hat{H}t}\chi e^{-\hat{H}(T-t)}}{\mathrm{Tr}e^{-\hat{H}T}} \tag{D.1}$$

$$= \frac{\sum \left\langle i \left|\chi^\dagger\right| j\right\rangle \left\langle j \left|\chi\right| i\right\rangle e^{-(E_0+E_j)t} e^{-(E_0+E_i)(T-t)}}{e^{-E_0 T}} \tag{D.2}$$

$$= \sum Z^\dagger_{ij} Z_{ji} e^{-E_j t} e^{-E_i(T-t)} \tag{D.3}$$

where χ's are the meson interpolation operators and $Z_{ij} \equiv \left\langle i \left|\chi\right| j\right\rangle$.

In Eq. (D.2), we insert complete sets of states and project out the energy eigenvalues. For the denominator, we make the following simplification,

$$\mathrm{Tr} e^{-\hat{H}T} = \sum_n \left\langle n \left| e^{-\hat{H}T} \right| n \right\rangle \tag{D.4}$$

$$\approx \left\langle 0 \left| e^{-\hat{H}T} \right| 0 \right\rangle \tag{D.5}$$

$$= e^{-E_0 T}. \tag{D.6}$$

Note that the denominator cancels out the vacuum energy in the numerator, therefore E_i and E_j is the energy above the ground state, as is the norm.

For this project, lattice configurations describe the QCD vacuum, therefore the interpolation operators act on the vacuum. Using this information, Eq. D.3 becomes,

$$C^{2\mathrm{pt}} = \sum_i \left(Z_{0i}^{\dagger} Z_{i0} e^{-E_i t} + Z_{0i} Z_{i0}^{\dagger} e^{-E_i (T-t)} \right). \tag{D.7}$$

The first term in Eq. (D.7) describes signal of the propagation of a meson while the second term describes the signal of a backwards propagating meson. The second term however, is suppressed by a factor of e^{-ET} indicating that this is a periodic boundary condition artifact. For data at $t < T/2$, contamination from the backward propagating signal is minimized.

D.2 Three-point fit function

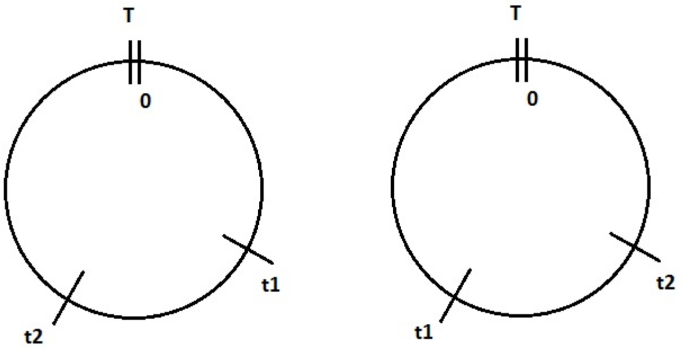

Figure D.2: Three-point source, sink and 4-quark operator locations for lattice of length T.

For the three-point fit functions, the 4-quark operator $\mathcal{O}$ is placed at $t = 0$ while the $\bar{D}$-meson and D-meson are respectively at t_1 and t_2. This allows for two possibilities of ordering the three operators.

$$0 < t_1 < t_2 \tag{D.8}$$

$$0 < t_2 < t_1 \tag{D.9}$$

Taking into account the periodic boundary conditions, the operators may again be placed in a circle as shown in Fig. D.2. Following the path integral formulation, the three-point fit function may be derived as the following,

$$\begin{aligned}
C^{3\text{pt}} =& \frac{1}{\text{Tr}e^{-\hat{H}T}} \Big\{ \Theta(t_1 - t_2)\text{Tr}\mathcal{O}e^{-\hat{H}t_2}\chi e^{-\hat{H}(t_1-t_2)}\chi e^{-\hat{H}(T-t_1)} \\
&+ \Theta(t_2 - t_1)\text{Tr}\mathcal{O}e^{-\hat{H}t_1}\chi e^{-\hat{H}(t_2-t_1)}\chi e^{-\hat{H}(T-t_2)} \Big\} \qquad \text{(D.10)} \\
=& \frac{1}{e^{-E_0 T}} \Bigg\{ \theta(t_1 - t_2) \sum_{i,j,k} \langle i \left| \mathcal{O} \right| j \rangle \langle j \left| \chi \right| k \rangle \langle k \left| \chi \right| i \rangle \\
& \quad \times e^{-(E_0+E_j)t_2} e^{-(E_0+E_k)(t_1-t_2)} e^{-(E_0+E_i)(T-t_1)} \\
&+ \theta(t_2 - t_1) \sum_{i,j,k} \langle i \left| \mathcal{O} \right| j \rangle \langle j \left| \chi \right| k \rangle \langle k \left| \chi \right| i \rangle \\
& \quad \times e^{-(E_0+E_j)t_1} e^{-(E_0+E_k)(t_2-t_1)} e^{-(E_0+E_i)(T-t_2)}. \qquad \text{(D.11)}
\end{aligned}$$

Collecting factors of $e^{-E_0 T}$ from the numerator cancels the vacuum energy in the denominator as expected. The energies are now defined as splittings above the vacuum energy. Next, act the operators on to the QCD vacuum yields the following six possibilities.

$$\begin{aligned}
C^{3\text{pt}} =& \sum_{i,j} \Big\{ \Theta(t_1 - t_2) Z_{0i} \mathcal{O}_{ij} Z_{j0} e^{-E_j^{(1)} t_2} e^{-E_i^{(1)}(T-t_1)} && \text{(D.12)} \\
&+ \Theta(t_2 - t_1) Z_{0i} \mathcal{O}_{ij} Z_{j0} e^{-E_j^{(1)} t_1} e^{-E_i^{(1)}(T-t_2)} && \text{(D.13)} \\
&+ \Theta(t_1 - t_2) \mathcal{O}_{0j} Z_{ji} Z_{i0} e^{-E_j^{(2)} t_2} e^{-E_i^{(1)}(t_1-t_2)} && \text{(D.14)} \\
&+ \Theta(t_1 - t_2) Z_{0j} Z_{ji} \mathcal{O}_{i0} e^{-E_j^{(1)}(t_1-t_2)} e^{-E_i^{(2)}(T-t_1)} && \text{(D.15)} \\
&+ \Theta(t_2 - t_1) \mathcal{O}_{0j} Z_{ji} Z_{i0} e^{-E_j^{(2)} t_1} e^{-E_i^{(1)}(t_2-t_1)} && \text{(D.16)} \\
&+ \Theta(t_2 - t_1) Z_{0j} Z_{ji} \mathcal{O}_{i0} e^{-E_j^{(1)}(t_2-t_1)} e^{-E_i^{(2)}(T-t_2)} \Big\} && \text{(D.17)}
\end{aligned}$$

Eq. (D.12) and (D.13) describes the process of a charmed-meson experiencing a 4-quark interaction and flavor changing into its anti-particle. These two equations describe the D-meson mixing process. Therefore, the energy eigenvalues $E_i^{(1)}$ involve the superscript (1) indicating that the states have one charm quark.

Eq. (D.14) through (D.17) describes the process of either two charmed-mesons combining to form one doubly-charmed state, or one doubly-charmed state decaying into two charmed-meson states. The energy eigenvalues $E_i^{(2)}$ indicate a state with two charm quarks. These are lattice artifacts which arise from the periodic boundary conditions.

So far, the three-point fit function formulation assumes that $0 < t_1, t_2 < T$. However, the source actually creates the D-meson before the meson interacts with the 4-quark operator placed at $t = 0$. This requires a time shift to be performed where $t_1 \to -|t_1| + T$. With this substitution, Eq. (D.12) through (D.17) becomes,

$$
\begin{aligned}
C^{3\mathrm{pt}} =& \sum_{i,j} \Big\{ \Theta(T - |t_1| - t_2) Z_{0i} \mathcal{O}_{ij} Z_{j0} e^{-E_j^{(1)} t_2} e^{-E_i^{(1)} |t_1|} && \text{(D.18)} \\
& + \Theta(t2 - |t_1| - T) Z_{0i} \mathcal{O}_{ij} Z_{j0} e^{-E_j^{(1)} (T - |t_1|)} e^{-E_i^{(1)} (T - t_2)} && \text{(D.19)} \\
& + \Theta(T - |t_1| - t_2) \mathcal{O}_{0j} Z_{ji} Z_{i0} e^{-E_j^{(2)} t_2} e^{-E_i^{(1)} (T - |t_1| - t_2)} && \text{(D.20)} \\
& + \Theta(T - |t_1| - t_2) Z_{0j} Z_{ji} \mathcal{O}_{i0} e^{-E_j^{(1)} (T - |t_1| - t_2)} e^{-E_i^{(2)} |t_1|} && \text{(D.21)} \\
& + \Theta(t_2 + |t_1| - T) \mathcal{O}_{0j} Z_{ji} Z_{i0} e^{-E_j^{(2)} (T - |t_1|)} e^{-E_i^{(1)} (T - |t_1| - t_2)} && \text{(D.22)} \\
& + \Theta(t_2 + |t_1| - T) Z_{0j} Z_{ji} \mathcal{O}_{i0} e^{-E_j^{(1)} (T - |t_1| - t_2)} e^{-E_i^{(2)} (T - t_2)} \Big\} && \text{(D.23)}
\end{aligned}
$$

Eq. (D.18) is the leading order contribution to the three-point correlation function; this term describes D-meson mixing and is the signal of interest. Eq. (D.19)also describes D-meson mixing, however this contribution is suppressed by two factors of e^{-ET} and therefore is sub-dominant and may be safely neglected. Eq. (D.20) through (D.23) describe lattice artifacts with doubly-charmed particles, however Eq. (D.20,D.21) are suppressed by one order of e^{-ET} and Eq. (D.22,D.23) are suppressed by two orders of e^{-ET} and therefore are also sub-dominant.

D.3 Oscillations

The choice of using the staggered action for light-quarks yields oscillations in the temporal direction. These effects may be derived by taking into account the details of the staggered interpolation operator. A meson interpolation operator involving a Wilson-type heavy-quark and a staggered light-quark has the following form[63],

$$\chi^0(t) = \bar{\psi}_{H,t} \gamma_5 \left(q_t^{\emptyset} + (-1)^t M_0^\dagger q_t^0 \right) \tag{D.24}$$

where ψ_H is the heavy quark spinor, $q^{\emptyset}$ is the light-quark momentum space spinor at the center of the Brillouin zone and q^0 is the temporal doubler. $M_0 = i\gamma_5\gamma_0$ is the operator what preserves doubling symmetry. It follows directly that,

$$\chi^{0\dagger}(t) = \left((-1)^t \bar{q}_t^0 M_0 - \bar{q}_t^{\emptyset} \right) \gamma_5 \psi_{H,t}. \tag{D.25}$$

The two-point correlator may be constructed by combining Eq. (D.24) and (D.25).

$$\left\langle \chi^{0\dagger}(t)\chi^{0}(0)\right\rangle = \mathrm{Tr}\left\{\left((-1)^t\bar{q}^0_t M_0 - \bar{q}^{\emptyset}_t\right)\gamma_5\psi_{H,t}\bar{\psi}_{H,0}\gamma_5\left(q^{\emptyset}_0 + (-1)^t M^\dagger_0 q^0_0\right)\right\} \tag{D.26}$$

$$\begin{aligned} &= \mathrm{Tr}\left\{q^{\emptyset}_0\bar{q}^{\emptyset}_t\gamma_5 + (-1)^{t+1}q^0_0\bar{q}^0_t M_0\gamma_5\psi_{H,t}\bar{\psi}_{H,0}\gamma_5 M^\dagger_0\right. \\ &\quad \left. + \text{ cross terms}\right\} \end{aligned} \tag{D.27}$$

$$= \mathrm{Tr}\left\{L_{0t}\gamma_5 H_{t0}\gamma_5 + (-1)^{t+1}L_{0t}M_0\gamma_5 H_{t0}\gamma_5 M^\dagger_0\right\} \tag{D.28}$$

$$= \mathrm{Tr}\left\{L_{0t}H^\dagger_{0t} + (-1)^{t+1}L_{0t}H^\dagger_{0t}\right\} \tag{D.29}$$

L and H correspond to the light and heavy quark propagator respectively. The cross terms in Eq. (D.27) may be dropped because the gauge links are smeared, suppressing the high energy gluons which mediates the process between $q^{\emptyset}$ and q^0. Applying γ_5-hermiticity and doubling symmetry $M_0 H_{0t} M^\dagger_0 = H_{0t}$, the oscillation terms from the staggered light quark is described by Eq. (D.29). Combining this result with Eq. (D.7), the two-point fit function is complete and is given in Eq. (D.30).

$$C^{2\mathrm{pt}}(t) = \sum_{n=0}^{N_s}(-1)^{n(t+1)}\frac{|Z_n|^2}{2E_n}\left(e^{-E_n t} + e^{-E_n(T-t)}\right) \tag{D.30}$$

Following the derivation of the two-point fit function, the oscillations in the three-point fit function at zeroth order in e^{-ET} is given in Eq. (D.31).

$$C^{3\mathrm{pt}}_i(t_1,t_2) = \sum_{m,n=0}^{N_s}(-1)^{n(t_2+1)}(-1)^{m(|t_1|+1)}\frac{\langle n\,|\mathcal{O}_i|\,m\rangle\, Z^\dagger_n Z_m}{4E_n E_m}e^{-E_n t_2}e^{-E_m|t_1|} \tag{D.31}$$

In Eq. (D.30) and (D.31), the states are relativistically normalized, yielding the factors of $1/2E_n$. The operator $\mathcal{O}_i$ here indicates the five 4-quark operators therefore, the three-point fit function is given a subscript i.

Appendix E

Theory of Constraint Curve Fitting

This section is dedicated to explaining the theory and algorithm behind the LSQFit fitter[47]. While the main objective of the project is to resolve the D-meson hadronic matrix elements, a solid understanding in numerical analysis is required. Central to this project, is the statistical theory behind the augmented-χ^2 minimization and the Levenberg-Marquardt algorithm.

E.1 The Augmented-χ^2

The type of constraint curve fitting used in this project is an extension of χ^2 minimization. In general, constraint curve fitting may be extended to other minimization methods (ie. least squared minimization). However, the data that is analyzed is Gaussian distributed amongst independent observations (configurations), naturally leading to the choice of χ^2 minimization.

The χ^2 distribution is defined as

$$\chi^2 = \sum_{t_1,t_2=1}^{T} (f_{t_1} - \bar{y}_{t_1})\, \Sigma^{-2}_{t_1,t_2}\, (f_{t_2} - \bar{y}_{t_2})\,. \tag{E.1}$$

Here $\bar{y}_t = \frac{1}{N}\sum_{i=1}^{N} y_{i;t}$ is the mean of the set $\{y\}$ with N independent and identically distributed (i.i.d.) vector of random variables with length T. The model describing the data is f_t, as is a function of a set of fit parameters $\{\rho\}$. The ρ's are the parameters that are varied by the optimization. Σ is the covariance matrix of the set $\{y\}$. An intuitive way to understand the χ^2 distribution is to calculate the χ^2/T, the χ^2 per degree of freedom. When the $chi^2 = 1$, the model is on average, consistent with the data to one standard deviation.

The way to include constraints into a χ^2 minimization is to incorporate *a priori* information of the fit parameters into the χ^2 statistic. An intuitive way to think about this is to think of giving the parameters their own data sets. The parameters are now called "priors" in the language of Bayesian statistics. The augmented χ^2 will then determined by both data from the i.i.d. random variables and the priors. Given a set of priors $\rho_i = N(\mu_i, \sigma_i^2)$ that are Gaussian i.i.d., the augmented χ^2 is defined as

$$\chi^2_{\text{aug}} = \chi^2 + \sum_{i=1}^{M} \frac{(\rho_i - \mu_i)^2}{\sigma_i^2}, \tag{E.2}$$

where the sum is over M priors. In Eq. (E.2), it is assumed that there are no correlations between the priors, and is the assumption made in this project. In general, the variance in Eq. (E.2) may be substituted by the covariance matrix. While it is not required that the priors be Gaussian distributed, the most unbiased choice for the probability density is given by a Gaussian distribution. This is derived by maximizing the differential entropy with constraints on normalization and constant variance,

$$S = -\int_{-\infty}^{\infty} P(\rho) \log P(\rho) d\rho, \tag{E.3}$$

$$1 = \int_{-\infty}^{\infty} P(\rho) d\rho, \tag{E.4}$$

$$\sigma^2 = \int_{-\infty}^{\infty} (x - \mu)^2 P(\rho) d\rho. \tag{E.5}$$

Using the method of Lagrange multipliers and variational calculus, the maximum entropy subject to constraints Eq. (E.4) and Eq. (E.5) yields

$$P(\rho) = \frac{1}{\sqrt{2\pi\sigma^2}} e^{-\dfrac{(\rho-\mu)^2}{2\sigma^2}}, \tag{E.6}$$

demonstrating that the Gaussian distribution is the most unbiased choice.

Philosophically, the validity of Bayesian inference is often questioned. From a frequentist point of view, probability is objective and merely reflect the frequency in which an observation will be made given that the number of measurements tend to infinity; while parameters are fixed (usually unknown) constants, and therefore do not have a probability distribution. Bayesian inference treats probability as a measure of belief, allowing one to make statements such as "On July 1st 1997 at 3pm, the probability that the Queen of England was drinking tea is 0.85", or allowing one to assign probability statements about parameters. For a frequentist, this would be absurd, since in both cases the statement does not refer to behavior at limiting frequency, but only a degree of belief and in general, such statements provoke heated discussions. Constraint curve fitting using χ^2 minimization falls under Bayesian inference since the parameters are given probability distributions. However, unlike the statement made on the Queen of England, the probability statements on many of the parameters originate from D-meson experimental values; values which have probability statements a frequentist would agree with. Therefore, while the constraint fits are formulated in the language of Bayesian inference, the probability statements made on the priors do not merely quantify belief; the priors quantify experimental observation and allow for a systematic inclusion of experimental data into the QCD simulation.

E.2 Steepest Decent: Levenberg-Marquardt Optimization

The algorithm behind minimizing the augmented χ^2 uses a more sophisticated version of the gradient descent called the Levenberg-Marquardt optimization. In vanilla gradient descent, the idea is to search for the minimum of a function $P(\rho)$ in the direction of steepest descent. The Levenberg-Marquardt optimization smoothly transitions between approximating $P(\rho)$ as a linear function for ρ far away form the minimum, and approximating $P(\rho)$ as a quadratic function for ρ near the minimum. The gradient of $P(\rho)$ is the vector

$$G_i(\rho) = \frac{\partial P(\rho)}{\partial \rho_i}, \tag{E.7}$$

while the Hessian of $P(\rho)$ is the matrix

$$H_{ij}(\rho) = \frac{\partial^2 P(\rho)}{\partial \rho_i \partial \rho_j}. \tag{E.8}$$

It follows that the Taylor expansion of $P(\rho)$ in the direction of $\hat{u}$ is

$$P(\rho + \epsilon\hat{u}) = P(\rho) + \epsilon G(\rho)^T \hat{u} + \frac{1}{2}\epsilon^2 \hat{u}^T H(\rho)\hat{u} + ... \tag{E.9}$$

Therefore,

$$\frac{d}{d\epsilon}P(\rho) = G(\rho)^T \hat{u} + \epsilon \hat{u}^T H(\rho)\hat{u}. \tag{E.10}$$

At this point, it is useful to consider the linearized and quadratic form of $P(\rho)$. If $P(\rho)$ is approximately linear, the direction of steepest descent is given by

$$\frac{d}{d\epsilon}P(\rho)\bigg|_{\epsilon=0} = G(\rho)^T \hat{u} \tag{E.11}$$

Therefore the optimization updates the point ρ in the direction of the negative gradient as follows,

$$\rho \to \rho - G(\rho). \tag{E.12}$$

The quadratic approximation of $P(\rho)$ results in the search direction towards the minimum,

$$\begin{aligned} \frac{d}{d\epsilon}P(\rho) =& G(\rho)^T \hat{u} + \epsilon \hat{u}^T H \hat{u} = 0 & \text{(E.13)} \\ \therefore \epsilon\hat{u} =& -H(\rho)^{-1} G(\rho) & \text{(E.14)} \end{aligned}$$

From Eq. (E.9), the optimization is updated as follows,

$$\therefore \rho \to \rho - H(\rho)^{-1}G(\rho). \tag{E.15}$$

The Levenberg optimization combines Eq. (E.12, E.15) by employing the following update rule,

$$\rho \to \rho - (H(\rho) + \lambda \mathbb{1})^{-1}G(\rho). \tag{E.16}$$

For small values of λ, Eq. (E.16) approaches the quadratic approximation Eq. (E.15) while for large values of λ, the update rule approaches the linear approximation. If the χ^2 increases after the update, this suggests that ρ is still far away from the minimum, and therefore the algorithm increases λ leverage the linear approximation. If the χ^2 decreases after the update, λ is decreased to leverage the quadratic approximation of $P(\rho)$.

Marquardt improved the Levenberg optimization by including estimation of the local curvature and replaced the identity with the diagonal of the Hessian resulting in the Levenberg-Marquardt method.

$$\rho \to \rho - (H(\rho) + \lambda \mathrm{diag}[H])^{-1}G(\rho). \tag{E.17}$$

By including information about the curvature inside the linear approximation, the algorithm searches faster in flat regions allowing for much faster convergence.

The Levenberg-Marquardt method is not optimized for speed or final error tolerance, but is a heuristic method for optimization and work extremely well in practice. One of the only flaws of this method lies in the fact that an inversion of the Hessian is needed. However for problem sizes where the rank of the Hessian is of order $\mathcal{O}(100)$, the Levenberg-Marquardt method is optimal; this corresponds to the size of the Hessian encountered in the D-meson mixing project.

Appendix F

Exhaustive List of Fit Parameters

This section provides an exhaustive list of every parameter used in this analysis. Motivation of the selection is discussed in the pertinent sections of the thesis.

F.1 The r_1 scale

Every number that appears in the simulation are dimensionless quantities since fundamental data structures of a computer involve integers, floats, strings, etc. and not meters, kilograms or electron volts for example. Therefore, in order to relate simulation quantities to physical values, a dimensionful length scale r_1 is defined in the simulation [60, 22]. The r_1 scale is defined by the static potential $F(r_1)$ such that

$$r_1^2 F(r_1) = 1.0. \tag{F.1}$$

For the MILC asqtad ensembles, r_1 has been determined by the MILC collaboration [10] to be

$$r_1 = 0.31174^{+0.0012}_{-0.0037}\text{fm} \tag{F.2}$$

while the lattice spacing dependent quantity r_1/a is calculated and then fitted via a smooth function [2] in order to arrive at the values listed in Table I of Ref. [10]. Possessing the value of r_1/a, we can translate all dimensionless simulation quantities into units of femtometers. For example, in the simulation, masses of quark have the form am_q because in natural units, masses have units of inverse length, therefore, we can convert the dimensionless mass parameter to 'r_1 units',

$$am_q \to \frac{r_1}{a} am_q \tag{F.3}$$

yielding the quark mass in units of femtometers. It is then straightforward to convert mass to units of energy by applying the appropriate factor of $\hbar c$. Similar exercises may be done for all parameters in order to convert from dimensionless lattice units to physical units.

F.2 MILC gauge configurations

The parameters of the MILC gauge configurations are given in Tab. F.1. In Tab. F.2, the valence quark propagators generated from the gauge ensembles are tabulated with their corresponding masses.

Table F.1: Parameters of ensembles. The first three columns list the approximate lattice spacing, volume, and spatial length in terms of the pion mass. The ratio am_l/am_s are listed, where the physical ratio is ~ 0.04. The corresponding pion mass is listed in the column m_π(MeV). N_{confgs} are the number of configurations in each ensemble. The r_1/a values are obtained by fitting the ratio to a smooth function [2], as shown in [10].

$a(fm)$	$\left(\frac{L}{a}\right)^3 \times \frac{T}{a}$	$m_\pi L$	am_l/am_s	m_π(MeV)	N_{confs}	r_1/a
0.12	$24^3 \times 64$	3.84	0.1	274	2099	2.647
0.12	$20^4 \times 64$	3.78	0.14	325	2110	2.635
0.12	$20^4 \times 64$	6.27	0.2	388	2259	2.618
0.12	$20^4 \times 64$	6.22	0.4	557	2052	2.644
0.09	$64^3 \times 64$	4.80	0.05	176	791	3.691
0.09	$40^4 \times 64$	4.21	0.1	249	1015	3.695
0.09	$32^4 \times 64$	4.11	0.14	308	984	3.697
0.09	$28^4 \times 64$	4.14	0.2	354	1931	3.699
0.09	$28^4 \times 64$	5.78	0.4	506	1996	3.712
0.06	$64^3 \times 144$	4.27	0.1	223	827	5.281
0.06	$56^4 \times 144$	4.39	0.14	264	801	5.292
0.06	$48^4 \times 144$	4.49	0.2	317	673	5.296
0.06	$48^4 \times 144$	6.33	0.4	451	593	5.283
0.045	$64^3 \times 192$	4.56	0.2	323	801	7.115

Table F.2: The list of partially-quenched datasets used in the analysis. The valence (sea) light-quark mass in lattice units is related to the pion mass through $m_\pi^2 = 2B_0 m_{q,l}$ [15].

$a(fm)$	am_l/am_s	am_q(lattice units)
0.12	0.1—0.4	$0.0050, 0.0070, 0.0100, 0.0200, 0.0300, 0.03497, 0.0415, 0.0500$
0.09	0.05	$0.00155, 0.0031, 0.0062, 0.0093, 0.0124, 0.0261, 0.0310$
0.09	0.1—0.4	$0.0031, 0.0047, 0.0062, 0.0093, 0.0124, 0.0261, 0.0310$
0.06	0.1—0.4	$0.0018, 0.0025, 0.0036, 0.0054, 0.0072, 0.0160, 0.0188$
0.045	0.2	$0.0018, 0.0028, 0.0040, 0.0056, 0.0084, 0.0130, 0.0160$

F.3 Two-point correlator parameters

Listed in Table F.3 are the estimated effective mass and scaled correlator values. The central values are averaged over all ensembles in the same lattice spacing, with the standard deviation describing the spread in observed values. These values are considered when setting the ground state priors for $\tilde{E}_0$ and $\tilde{Z}_0$.

Ensemble	M_{eff} C.V.	Std. Dev.	$Z_{\text{eff}}^{1/4}$ C.V.	Std. Dev.
Coarse	0.9791	0.0290	1.443	0.0255
Fine	0.7502	0.0175	1.411	0.0274
sFine	0.5546	0.0121	1.365	0.0291
uFine	0.4125	0.0109	1.351	0.0271

Table F.3: Estimated values for effective mass and scaled correlator averaged over ensembles of the same lattice spacing.

Listed in Table F.4 are the energy splittings for $D^0 - D^{0*}$ and radial excitation splittings. The $D^0 - D^{0*}$ splitting is obtained from the Particle Data Group [14] while the radial excitations are estimated from quark models [34]. The energy splittings in lattice units are listed as the natural log of the splittings as per defined in the priors. Eq. F.4 specifies the conversion from GeV to lattice units.

$$\tilde{E}_n \equiv \ln\left(\Delta E[\text{lattice units}]\right) = \ln\left(a[\text{m}] \times \Delta E[\text{eV}] \times \frac{1}{\hbar c[\text{eV*m}]}\right) \tag{F.4}$$

Splitting	ΔE[MeV]	$\tilde{E}_n$(Coarse)	$\tilde{E}_n$(Fine)	$\tilde{E}_n$(sFine)	$\tilde{E}_n$(uFine)
$D^0 - D^{0*}$	~ 454	-1.287	-1.574	-1.980	-2.268
$D_n - D_{n-1}$	~ 650	-0.928	-1.216	-1.621	-1.909

Table F.4: Energy splittings in MeV and the natural log of the energy splittings in lattice units.

The excited state $\tilde{Z}_n$s are expected to be smaller than the ground state value due to operator smearing. This information is used to set priors for $\tilde{Z}_n$.

F.4 Three-point correlator parameters

Listed in Table F.5 and F.6 are the values for the SM and BSM scaled three-point correlator. These values guide the prior selection for the ground state $\tilde{O}_{i;00}$, where $i = \{1, 2, 3, 4, 5\}$ denotes the five 4-quark operators.

Ensemble	$O_{1,\text{eff}}$	Std. Dev.	$O_{2,\text{eff}}$	Std. Dev.	$O_{3,\text{eff}}$	Std. Dev.
Coarse	2.48E-2	3.54E-3	-5.36E-2	6.93E-3	1.22E-2	1.63E-3
Fine	8.78E-3	1.15E-3	-1.89E-2	2.71E-3	4.68E-3	6.13E-4
sFine	2.85E-3	4.91E-4	-7.12E-3	9.58E-4	1.72E-3	2.13E-4
uFine	1.22E-3	1.77E-4	-3.28E-3	4.00E-4	8.01E-4	8.43E-5

Table F.5: Estimated scaled three-point values for Standard Model 4-quark operators in lattice units.

Ensemble	$O_{4,\text{eff}}$	Std. Dev.	$O_{5,\text{eff}}$	Std. Dev.
Coarse	9.63E-2	1.00E-2	4.04E-2	4.60E-3
Fine	3.86E-2	4.30E-3	1.58E-2	1.91E-3
sFine	1.45E-2	1.56E-3	5.90E-3	6.41E-4
uFine	6.89E-3	7.06E-4	2.71E-3	2.83E-4

Table F.6: Estimated scaled three-point values for Beyond Standard Model 4-quark operators in lattice units.

The excited state $\tilde{O}_i$'s are expected to have values around the same order of magnitude as the ground state matrix elements since the 4-quark operator is not smeared. This information is adequate for setting the $\tilde{O}_{i;nm}$ priors.

F.5 Correlator priors and time ranges

Chapter 4 and Section F.3, F.4 motivates the selection of the correlator priors. The priors used for the final correlator fits are provided in Table F.7. $\tilde{Z}_n$ and $\tilde{E}_n$ denote excited state decay priors where $n \geq 2$. The excited state matrix elements priors $\tilde{O}_{nm}$ are the same for all five operators for n or $m \geq 1$.

Ensemble	$\tilde{Z}_0$	$\tilde{Z}_1$	$\tilde{Z}_n$
Coarse	1.45(0.08)	0.7(0.5)	0.7(1.0)
Fine	1.42(0.08)	0.7(0.5)	0.7(1.0)
sFine	1.37(0.1)	0.7(0.5)	0.7(1.0)
uFine	1.36(0.1)	0.7(0.5)	0.7(1.0)
	$\tilde{E}_0$	$\tilde{E}_1$	$\tilde{E}_n$
Coarse	1.0(0.1)	-1.2(0.5)	-1.0(1.5)
Fine	0.75(0.05)	-1.6(0.5)	-1.2(2.0)
sFine	0.56(0.04)	-2.0(1.0)	-1.6(2.0)
uFine	0.42(0.04)	-2.3(1.0)	-1.9(2.0)
	$\tilde{O}_1$	$\tilde{O}_2$	$\tilde{O}_3$
Coarse	0.025(0.01)	-0.055(0.02)	0.012(0.006)
Fine	0.009(0.003)	-0.02(0.006)	0.005(0.002)
sFine	0.003(0.0015)	-0.007(0.003)	0.0017(0.0005)
uFine	0.0013(0.0008)	-0.0035(0.0015)	0.0008(0.0003)
	$\tilde{O}_4$	$\tilde{O}_5$	$\tilde{O}_{nm}$
Coarse	0.1(0.03)	0.04(0.015)	0(0.1)
Fine	0.04(0.01)	0.016(0.005)	0(0.05)
sFine	0.015(0.005)	0.006(0.002)	0(0.02)
uFine	0.007(0.002)	0.0027(0.0008)	0(0.01)

Table F.7: Finalized priors used in correlator fits.

The final fit ranges used in the two- and three-point correlator fits are listed in Table F.8. The physical length of $t_{\text{min}} = 0.72\text{fm}$ for all four lattice spacings. The physical length of t_{max} varies linearly as a function of lattice spacing from 2.25fm to 3fm.

Lattice Spacing (fm)	t_{min}(lattice units)	t_{max}(lattice units)
Coarse0.12	6	25
Fine0.09	8	30
Superfine0.06	12	42
Ultrafine0.045	16	50

Table F.8: Finalized time ranges used in 2+2 state two- and three-point correlator fits.

F.6 Renormalization and matching parameters

	$\mathcal{O}_1$		$\mathcal{O}_2$		$\mathcal{O}_3$	
	ζ_{11}	ζ_{12}	ζ_{22}	ζ_{21}	ζ_{33}	ζ_{31}
$a0.12$						
BBGLN	0.051	−0.066	0.327	0.448	0.527	0.010
BJU			0.008	0.434	0.633	−0.004
$a0.09$						
BBGLN	0.120	-0.049	−0.015	0.479	0.658	−0.065
BJU			−0.333	0.466	0.764	−0.078
$a0.06$						
BBGLN	0.197	-0.032	−0.388	0.519	0.796	−0.142
BJU			−0.706	0.506	0.902	−0.156
$a0.045$						
BBGLN	0.269	-0.023	−0.695	0.552	0.918	−0.225
BJU			−1.014	0.538	1.024	−0.238

Table F.9: Renormalization coefficients for $\{\mathcal{O}_1, \mathcal{O}_2, \mathcal{O}_3\}$. The BBGLN and BJU values for $\mathcal{O}_1$ are the same.

$\mathcal{O}_4$		$\mathcal{O}_5$	
ζ_{44}	ζ_{45}	ζ_{55}	ζ_{54}
$a0.12$			
0.091	-0.255	0.138	-0.291
$a0.09$			
-0.382	-0.250	0.175	-0.469
$a0.06$			
-0.901	-0.234	0.234	-0.645
$a0.045$			
-1.337	-0.238	0.269	-0.790

Table F.10: Renormalization coefficients for $\{\mathcal{O}_4, \mathcal{O}_5\}$. The BBGLN and BJU values for $\mathcal{O}_4$ and $\mathcal{O}_5$ are the same.

	$\mathcal{O}_1$		$\mathcal{O}_2$		$\mathcal{O}_3$	
	ζ_{11}	ζ_{12}	ζ_{22}	ζ_{21}	ζ_{33}	ζ_{31}
$k0.1254$						
BBGLN	0.051	-0.066	0.327	0.448	0.527	0.010
BJU			0.008	0.434	0.633	-0.004
$k0.1280$						
BBGLN	0.029	-0.055	0.278	0.478	0.523	0.016
BJU			-0.040	0.464	0.629	0.002

Table F.11: Renormalization coefficients for $\{\mathcal{O}_1, \mathcal{O}_2, \mathcal{O}_3\}$ kappa tuning points.

$\mathcal{O}_4$		$\mathcal{O}_5$	
ζ_{44}	ζ_{45}	ζ_{55}	ζ_{54}
$k0.1254$			
0.091	-0.255	0.138	-0.291
$k0.1280$			
0.045	-0.249	0.129	-0.303

Table F.12: Renormalization coefficients for $\{\mathcal{O}_4, \mathcal{O}_5\}$ kappa tuning points.

F.7 Kappa tuning parameters

A table of values for the critical, tuned and simulation κs, tadpole-improvement factor u_0 and r_1/a are given in Table F.13. The tuned and simulation κ values are transcribed from Ref. [6]; the u_0 values are transcribed from Ref. [10].

a(fm)	m_l/m_s	κ_{crit}	κ_{tune}	$\kappa_{\text{sim.}}$	u_0	r_1/a
0.12	0.4	0.14073	0.12452(15)(16)	0.1259	0.8688	2.821123
0.12	0.2	0.14091	0.12423(15)(16)	0.1254	0.8677	2.738591
0.12	0.14	0.14095	0.12423(15)(16)	0.1254	0.8678	2.738591
0.12	0.1	0.14096	0.12423(15)(16)	0.1254	0.8678	2.738591
0.09	0.4	0.139052	0.12737(9)(14)	0.1277	0.8788	3.857729
0.09	0.2	0.139119	0.12722(9)(14)	0.1276	0.8782	3.788732
0.09	0.14	0.139134	0.12718(9)(14)	0.1275	0.8781	3.771633
0.09	0.1	0.139173	0.12714(9)(14)	0.1275	0.8779	3.754593
0.09	0.05	0.13919	0.12710(9)(14)	0.1275	0.877805	3.737613
0.06	0.4	0.137582	0.12964(4)(11)	0.1295	0.8881	5.399129
0.06	0.2	0.137632	0.12960(4)(11)	0.1296	0.88788	5.353063
0.06	0.14	0.137667	0.12957(4)(11)	0.1296	0.88776	5.330159
0.06	0.1	0.137678	0.12955(4)(11)	0.1296	0.88764	5.307340
0.045	0.2	0.13664	0.130921(16)(70)	0.1310	0.89511	7.208234

Table F.13: Parameters used for the kappa tuning corrections. The slopes outlined by Eq. (6.5) are calculated on the $a = 0.12$, $m_l/m_s = 0.2$ ensemble with an additional simulated $\kappa = 0.1280$.

The values of ΔM_2 as described by Eq. 6.6) are given in Table F.14.

a(fm)	m_l/m_s	ΔM_2
0.12	0.4	$-0.0751(0.0110)$
0.12	0.2	$-0.0612(0.0107)$
0.12	0.14	$-0.0610(0.0107)$
0.12	0.1	$-0.0610(0.0107)$
0.09	0.4	$-0.0230(0.0113)$
0.09	0.2	$-0.0261(0.0111)$
0.09	0.14	$-0.0218(0.0110)$
0.09	0.1	$-0.0244(0.0109)$
0.09	0.05	$-0.0271(0.0109)$
0.06	0.4	$+0.0140(0.0119)$
0.06	0.2	$+0.0000(0.0117)$
0.06	0.14	$-0.0030(0.0116)$
0.06	0.1	$-0.0050(0.0116)$
0.045	0.2	$-0.0115(0.0103)$

Table F.14: Values of $1/r_1 M_2$ for all ensembles used in the analysis.

The values of the kappa tuning slope extracted from the two-parameter linear fits are given in Table F.15.

operator	slope
$\mathcal{O}_1$	$-0.3112(0.1078)$
$\mathcal{O}_2$	$+0.0868(0.0580)$
$\mathcal{O}_3$	$-0.0038(0.0248)$
$\mathcal{O}_4$	$-0.1597(0.2593)$
$\mathcal{O}_5$	$-0.1618(0.1049)$

Table F.15: The slopes outlined by Eq. (6.5) are calculated on the $a = 0.12$, $m_l/m_s = 0.2$ ensemble with an additional simulated $\kappa = 0.1280$.

F.8 Chiral and continuum extrapolation parameters

Parameters use in the chiral-continuum extrapolation are listed here.

Λ_χ	$\beta_{1,3,4,5}$	β_2	$\beta'_{2,3,4,5}$
775MeV	1 ± 1	-1 ± 1	0 ± 1

c_i	d_i	δ'_V	δ'_A
0 ± 1	0 ± 1	0 ± 0.07	-0.28 ± 0.06

f_π	$g_{D^*D\pm}$	Λ_1	Δ^*
130 ± 0.2MeV	0.53 ± 0.08	$0.219 \pm 0.003\text{GeV}^{-1}$	142.1 ± 2.6MeV

Table F.16: Parameters and priors of the chiral-continuum fit.

References

[1] Georges Aad et al. Observation of a new particle in the search for the Standard Model Higgs boson with the ATLAS detector at the LHC. *Phys.Lett.*, B716:1–29, 2012.

[2] C.R. Allton. Lattice Monte Carlo data versus perturbation theory. 1996.

[3] Y. Amhis et al. Averages of b-hadron, c-hadron, and τ-lepton properties as of summer 2014. 2014.

[4] C. Aubin et al. Light pseudoscalar decay constants, quark masses, and low energy constants from three-flavor lattice QCD. *Phys.Rev.*, D70:114501, 2004.

[5] Z. Bai, N.H. Christ, T. Izubuchi, C.T. Sachrajda, A. Soni, et al. The $K_L - K_S$ mass difference from lattice QCD. 2014.

[6] Jon A. Bailey, A. Bazavov, C. Bernard, M. Bouchard, C. C. DeTar, Daping Du, X. El-Khadra, A. J. Foley, D. Freeland, E. E. Gámiz, Steven Gottlieb, M. Heller, U. S. Kronfeld, A. J. Laiho, L. Levkova, B. Mackenzie, P. T. Neil, E. Si-Wei Qiu, J. Simone, R. Sugar, D. Toussaint, S. Van de Water, R. and Ran Zhou. Update of $|V_{cb}|$ from the $\overline{B} \to D^* \ell \overline{\nu}$ form factor at zero recoil with three-flavor lattice qcd. *Phys. Rev. D*, 89:114504, Jun 2014.

[7] Jon A. Bailey et al. Update of $|V_{cb}|$ from the $\bar{B} \to D^* \ell \bar{\nu}$ form factor at zero recoil with three-flavor lattice QCD. *Phys.Rev.*, D89(11):114504, 2014.

[8] A. Bazavov et al. B- and D-meson decay constants from three-flavor lattice QCD. *Phys.Rev.*, D85:114506, 2012.

[9] A. Bazavov et al. Charmed and light pseudoscalar meson decay constants from four-flavor lattice QCD with physical light quarks. 2014.

[10] A. Bazavov, D. Toussaint, C. Bernard, J. Laiho, C. DeTar, L. Levkova, M. B. Oktay, Steven Gottlieb, U. M. Heller, J. E. Hetrick, P. B. Mackenzie, R. Sugar, and R. S. Van de Water. Nonperturbative qcd simulations with $2+1$ flavors of improved staggered quarks. *Rev. Mod. Phys.*, 82:1349–1417, May 2010.

[11] Damir Becirevic and Francesco Sanfilippo. Theoretical estimate of the $D^* \to D\pi$ decay rate. *Phys.Lett.*, B721:94–100, 2013.

[12] M. Beneke, G. Buchalla, C. Greub, A. Lenz, and U. Nierste. Next-to-leading order qcd corrections to the lifetime difference of b(s) mesons. *Phys.Lett.*, B459:631–640, 1999.

[13] J. Beringer et al. Review of Particle Physics (RPP). *Phys.Rev.*, D86:010001, 2012.

[14] J. Beringer and et al. (Particle Data Group). The review of particle physics. *Phys. Rev.*, D86, 010001 2012.

[15] C. Bernard. Neutral B Mixing in Staggered Chiral Perturbation Theory. *Phys.Rev.*, D87(11):114503, 2013.

[16] C. Bernard, C. DeTar, M. Di Pierro, A. X. El-Khadra, R. T. Evans, E. D. Freeland, E. Gámiz, Steven Gottlieb, U. M. Heller, J. E. Hetrick, A. S. Kronfeld, J. Laiho, L. Levkova, P. B. Mackenzie, J. N. Simone, R. Sugar, D. Toussaint, and R. S. Van de Water. Tuning fermilab heavy quarks in $2 + 1$ flavor lattice qcd with application to hyperfine splittings. *Phys. Rev. D*, 83:034503, Feb 2011.

[17] C. Bernard et al. Tuning Fermilab Heavy Quarks in 2+1 Flavor Lattice QCD with Application to Hyperfine Splittings. *Phys.Rev.*, D83:034503, 2011.

[18] Claude Bernard et al. Observations on staggered fermions at non-zero lattice spacing. *Phys.Rev.*, D73:114511, 2006.

[19] Claude Bernard et al. Comment on 'Chiral anomalies and rooted staggered fermions'. *Phys.Lett.*, B649:235–240, 2007.

[20] Claude Bernard et al. 't Hooft vertices, partial quenching, and rooted staggered QCD. *Phys.Rev.*, D77:114504, 2008.

[21] Claude W. Bernard. Weak Matrix Elements on and off the Lattice. 1989.

[22] Claude W. Bernard, Tom Burch, Kostas Orginos, Doug Toussaint, Thomas A. DeGrand, et al. The Static quark potential in three flavor QCD. *Phys.Rev.*, D62:034503, 2000.

[23] K.U. Can, G. Erkol, M. Oka, A. Ozpineci, and T.T. Takahashi. Vector and axial-vector couplings of D and D^* mesons in 2+1 flavor Lattice QCD. *Phys.Lett.*, B719:103–109, 2013.

[24] N. Carrasco, M. Ciuchini, P. Dimopoulos, R. Frezzotti, V. Gimenez, V. Lubicz, C. Rossi, G. F. Sanfilippo, L. Silvestrini, S. Simula, and C. Tarantino. $D^0 - \overline{d}^0$ mixing in the standard model and beyond from $N_f = 2$ twisted mass qcd. *Phys. Rev. D*, 90:014502, Jul 2014.

[25] Serguei Chatrchyan et al. Observation of a new boson at a mass of 125 GeV with the CMS experiment at the LHC. *Phys.Lett.*, B716:30–61, 2012.

[26] M Creutz. The evil that is rooting. Technical report, Jan 2007. hep-lat/0701018.

[27] Michael Creutz. Chiral anomalies and rooted staggered fermions. *Phys.Lett.*, B649:230–234, 2007.

[28] Michael Creutz. Why rooting fails. *PoS*, LAT2007:007, 2007.

[29] Amitava Datta and Dharmadas Kumbhakar. d^0-$\bar{D}^0$ mixing: A possible test of physics beyond the standard model. *Zeitschrift fr Physik C Particles and Fields*, 27(4):515–522, 1985.

[30] C.T.H. Davies, E. Follana, I.D. Kendall, G. Peter Lepage, and C. McNeile. Precise determination of the lattice spacing in full lattice QCD. *Phys.Rev.*, D81:034506, 2010.

[31] P. Dimopoulos, R. Frezzotti, P. Lami, V. Lubicz, E. Picca, et al. Pseudoscalar decay constants f_K/f_π, f_D and f_{D_s} with $N_f = 2+1+1$ ETMC configurations. 2013.

[32] S. Durr, Z. Fodor, J. Frison, C. Hoelbling, R. Hoffmann, et al. Ab-Initio Determination of Light Hadron Masses. *Science*, 322:1224–1227, 2008.

[33] Stephan Durr. Theoretical issues with staggered fermion simulations. *PoS*, LAT2005:021, 2006.

[34] D. Ebert, R.N. Faustov, and V.O. Galkin. Heavy-light meson spectroscopy and Regge trajectories in the relativistic quark model. *Eur.Phys.J.*, C66:197–206, 2010.

[35] Aida X. El-Khadra, Andreas S. Kronfeld, and Paul B. Mackenzie. Massive Fermions in Lattice Gauge Theory. *Phys. Rev.*, D55:3933–3957, 1997.

[36] Adam F. Falk, Yuval Grossman, Zoltan Ligeti, and Alexey A. Petrov. SU(3) breaking and D0 - anti-D0 mixing. *Phys.Rev.*, D65:054034, 2002.

[37] H. Fukaya et al. Determination of the chiral condensate from 2+1-flavor lattice QCD. *Phys.Rev.Lett.*, 104:122002, 2010.

[38] Eugene Golowich, JoAnne Hewett, Sandip Pakvasa, and Alexey A. Petrov. Relating D0-anti-D0 Mixing and D0 $\to$ l+ l- with New Physics. *Phys.Rev.*, D79:114030, 2009.

[39] Eugene Golowich and Alexey A. Petrov. Short distance analysis of D0 - anti-D0 mixing. *Phys.Lett.*, B625:53–62, 2005.

[40] R. Horsley, Y. Nakamura, A. Nobile, P.E.L. Rakow, G. Schierholz, et al. Nucleon axial charge and pion decay constant from two-flavor lattice QCD. *Phys.Lett.*, B732:41–48, 2014.

[41] Andreas S. Kronfeld. Lattice gauge theory with staggered fermions: how, where, and why (not). 2007. arxiv/0711.0699.

[42] Weon-Jong Lee and Stephen R. Sharpe. Partial flavor symmetry restoration for chiral staggered fermions. *Phys.Rev.*, D60:114503, 1999.

[43] Laurent Lellouch and Martin Luscher. Weak transition matrix elements from finite volume correlation functions. *Commun.Math.Phys.*, 219:31–44, 2001.

[44] G. P. Lepage. Lattice QCD for Novices. 1998.

[45] G. Peter Lepage. On the Absence of O(a) Errors in Staggered-Quark Discretizations. 2011.

[46] G. Peter Lepage and Paul B. Mackenzie. On the viability of lattice perturbation theory. *Phys.Rev.*, D48:2250–2264, 1993.

[47] G.P. Lepage. lsqfit documentation. 2014.

[48] M. Lüscher and P. Weisz. Computation of the action for on-shell improved lattice gauge theories at weak coupling. *Physics Letters B*, 158:250–254, August 1985.

[49] Aneesh Vasant Manohar and Mark B Wise. *Heavy quark physics*. Cambridge monographs on particle physics, nuclear physics, and cosmology. Cambridge Univ. Press, Cambridge, 2000. Updates can be found at http://einstein.ucsd.edu/hqbook.

[50] Q. Mason, H. D. Trottier, C. T. H. Davies, K. Foley, A. Gray, G. P. Lepage, M. Nobes, and J. Shigemitsu. Accurate determinations of α_s from realistic lattice qcd. *Phys. Rev. Lett.*, 95:052002, Jul 2005.

[51] C. McNeile, A. Bazavov, C.T.H. Davies, R.J. Dowdall, K. Hornbostel, et al. Direct determination of the strange and light quark condensates from full lattice QCD. *Phys.Rev.*, D87(3):034503, 2013.

[52] Damian Paul Menscher. *Charmonium and charmed mesons with improved lattice QCD*. PhD thesis, University of Illinois at Urbana-Champaign, Urbana, May 2005.

[53] C.C. Nishi. Simple derivation of general Fierz-like identities. *Am.J.Phys.*, 73:1160–1163, 2005.

[54] John L. Richardson. The heavy quark potential and the , j/ systems. *Physics Letters B*, 82(2):272 – 274, 1979.

[55] Jonathan L. Rosner and Sheldon Stone. Leptonic Decays of Charged Pseudoscalar Mesons. 2010.

[56] Stefan Scherer. Introduction to chiral perturbation theory. *Adv.Nucl.Phys.*, 27:277, 2003.

[57] M.D. Schwartz. *Quantum Field Theory and the Standard Model*. Quantum Field Theory and the Standard Model. Cambridge University Press, 2013.

[58] Stephen R. Sharpe. Rooted staggered fermions: Good, bad or ugly? *PoS*, LAT2006:022, 2006.

[59] B. Sheikholeslami and R. Wohlert. Improved continuum limit lattice action for {QCD} with wilson fermions. *Nuclear Physics B*, 259(4):572 – 596, 1985.

[60] R. Sommer. A New way to set the energy scale in lattice gauge theories and its applications to the static force and alpha-s in SU(2) Yang-Mills theory. *Nucl.Phys.*, B411:839–854, 1994.

[61] D. Toussaint and W. Freeman. The Strange quark condensate in the nucleon in 2+1 flavor QCD. *Phys.Rev.Lett.*, 103:122002, 2009.

[62] T. van Ritbergen, J.A.M. Vermaseren, and S.A. Larin. The four loop beta function in quantum chromodynamics. *Phys.Lett.*, B400:379–384, 1997.

[63] Matthew Wingate, Junko Shigemitsu, Christine T.H. Davies, G. Peter Lepage, and Howard D. Trottier. Heavy light mesons with staggered light quarks. *Phys.Rev.*, D67:054505, 2003.